Order Number 9426994

Heart rate variability study using phase response curve

Zhang, Peizhuan, Ph.D.

New Jersey Institute of Technology, 1994

U·M·I
300 N. Zeeb Rd.
Ann Arbor, MI 48106

ABSTRACT

Heart Rate Variability Study
Using Phase Response Curve

by
Peizhuan Zhang

A noninvasive phase resetting experiment on human subjects was investigated. The phase response curve was estimated and was used to demonstrate cardiac phase resetting due to a vagal input. The estimated running phase response curve showed that the cardiac cycle resetting depended on the time and the amplitude of the vagal stimulation. The phase response curve was then studied using time circle analysis, topological analysis and nonlinear dynamics analysis. Also phase entrainment and stimulus frequency dependence of the phase response were evaluated. Further, the Van Der Pol model, Generalized Additive model and Knight and Peskin's model were used to simulate the phase resetting process so that the characteristics of the phase resetting can be better understood.

HEART RATE VARIABILITY STUDY USING PHASE RESPONSE CURVE

by
Peizhuan Zhang

A Dissertation
Submitted to the Faculty of
New Jersey Institute of Technology
in Partial Fulfillment of the Requirements for the Degree of
Doctor of Philosophy

Department of Electrical and Computer Engineering

May 1994

APPROVAL PAGE

HEART RATE VARIABILITY STUDY USING PHASE RESPONSE CURVE

Peizhuan Zhang

Dr. Stanley S. Reisman, Dissertation Advisor — Date
Professor of Electrical and Computer Engineering, NJIT

Dr. Walter N. Tapp, Committee Member — Date
Professor of Neuroscience,
University of Medicine and Dentistry

Dr. Peter Engler, Committee Member — Date
Associate Professor of Electrical and Computer Engineering, NJIT

Dr. Timothy Chang, Committee Member — Date
Assistant Professor of Electrical and Computer Engineering, NJIT

Dr. Michael Lacker, Committee Member — Date
Professor of Mathematics, NJIT

BIOGRAPHICAL SKETCH

Author: Peizhuan Zhang

Degree: Doctor of Philosophy
Electrical and Computer Engineering

Date: May 1994

Undergraduate and Graduate Education:

- Doctor of Philosophy in Electrical and Computer Engineering,
  New Jersey Institute of Technology,
  Newark, New Jersey, 1994

- Master of Science in Electrical and Computer Engineering,
  New Jersey Institute of Technology,
  Newark, New Jersey, 1990

- Bachelor of Science in Electrical Engineering,
  Tianjin University, Tianjin, China

Major: Electrical Engineering

Presentations and Publications:

P. Zhang, S. Reisman and W. Tapp, "Heart rate variability study using phase response curve," *IEEE Biomed. Eng. Conf.*, Paris, pp571-572, 1992.

P. Zhang, S. Reisman, W. Tapp and D. Cordero, "Information entropy and dimension calculation on heart rate variability," *19th IEEE Annual Northeast Bioeng. Conf.*, pp9-10, 1993.

This dissertation is dedicated to
Yumei, my wife, Edwin, my son,
my parents and my parents-in-law

ACKNOWLEDGMENT

I wish to express my sincere gratitude to my dissertation advisor, Professor Stanley S. Reisman in the Department of Electrical and Computer Engineering at the New Jersey Institute of Technology, for his guidance, friendship, and a great deal of support throughout this research.

I would also like to express my gratitude to my supervisor, Professor Walter N. Tapp at the CFS center, University of Medicine and Dentistry, for his guidance, excellent ideas and friendship.

Special thanks to Professor Peter Engler, Professor Timothy Chang and Professor Michael Lacker for their valuable suggestions and discussions during the whole period of the research and for serving as members of the committee.

Many thanks to Dr. Benjamin H. Natelson for his personal and sincere care during the research at the VA Medical Center.

I am truly thankful to all the professors and staff of the Department of Electrical and Computer Engineering who have been helpful and supportive throughout my study in the doctoral program.

TABLE OF CONTENTS

Chapter **Page**

1 INTRODUCTION....1

1.1 Introduction to Heart Rate Variability....1

1.2 Past and Current Trends of the Research....3

1.3 The Scope of Our Research....7

2 BACKGROUND....12

2.1 The Heart and the Electrocardiogram....12

2.2 Measurement of the EKG....14

2.3 Neural Effects on the Heart....18

2.4 Neural Coupling between Cardiac Oscillatory System and Pulmonary System....24

3 HEART RATE VARIABILITY STUDY USING COMPLEX DEMODULATION....28

3.1 Introduction....28

3.2 Complex Demodulation....28

3.3 Applications of Complex Demodulation....32

4 SPECTRUM ANALYSIS OF HEART RATE VARIABILITY....39

4.1 Introduction....39

4.2 Experiment and Method....41

4.3 Vagal Activity Study Using the Power Spectrum....43

Chapter **Page**

5 RECENT DEVELOPMENT OF PHASE DEPENDENCE STUDY IN HEART RATE VARIABILITY....48

5.1 Introduction....48

5.2 A Review of Current Research on Phase Dependence....50

6 PHASE DEPENDENCE STUDY....56

6.1 Experiment....56

6.2 Some Concepts of Phase Dependence....57

6.3 Phase Response Curve....58

6.4 Reexamination of the PRC....68

6.5 Comparison between Controls and CFS Subjects....75

6.6 Discussion....83

7 TOPOLOGICAL STUDY....85

7.1 Introduction....85

7.2 Phase Plane....86

7.3 Poincare Map....92

7.4 3-D Study....99

8 NONLINEAR DYNAMICS STUDY....105

8.1 Introduction....105

8.2 Probability Density Curve (PDC)....106

8.3 Information Entropy and Dimension....109

8.4 Comparison between Controls and CFS Subjects....112

Chapter **Page**

8.5 Discussion....114

9 MODELING AND SIMULATION....116

9.1 Introduction....116

9.2 Second-order Systems....117

9.3 Van Der Pol Model....123

9.3.1 A Van Der Pol Model....124

9.3.2 Phase Response to an Impulse....126

9.3.3 Two Coupled Van Der Pol Oscillators....130

9.4 Generalized Additive Model....133

9.5 Knight and Peskin's Models....144

A. Knight's Simple Integrate-and-fire Model....144

B. Knight's Forgetful Integrate-and-fire Model....150

C. Peskin's Model....154

10 CONCLUSIONS....159

10.1 Summary of the Research....159

10.2 Conclusion....164

10.3 Future Development of the Research....166

APPENDIX I Splus Functions....168

APPENDIX II Car Test Data Frame....180

APPENDIX III The General Linear Perturbation Theory....183

APPENDIX IV Figures for the Simulation....186

Chapter **Page**

APPENDIX V Programs 190

REFERENCES.....197

LIST OF TABLES

Table **Page**

1 The MHRV at different pacing rates during sitting and standing.....70

2 Comparison between the normal and the CFS groups in MHRV.....80

3 Comparison between the normal and the CFS groups in information dimension.....113

4 The GAM models at different transforms.....140

5 The improved models.....141

LIST OF FIGURES

Figure **Page**

1 Heart rates of a young adult during rest. Total 300 beats are measured. x-axis is heart beat numbers, y-axis is heart rates with the unit of beats per minute....1

2 (a) ECG signal. (b) R-wave pulse train. (c) IBI value. (d) Interpolated IBI values. The dot in (d) represents interpolated data points....2

3 A spectrum of heart rate variability signal. The corresponding heart rates are shown in Figure 1.1.1....3

4 An amplitude of output of complex demodulation from the IBI signal for a conditioned dog after the shock. x-axis represents time....4

5 Diagrammatic section of the heart. The arrows indicate the direction of blood flow....12

6 Conducting system of the heart. The interatrial conducting bundle are not shown in the Figure....13

7 Typical electrocardiogram. P, atrial depolarization; QRS, ventricular depolarization; T, ventricular repolarization....14

8 Idealized connections for making an ECG recording. The function of amplifier (Amp) is to amplify the voltage between left Arm (LA) and left leg (LL) electrodes by a factor of about 500. The right-leg electrode (RL) is a voltage reference....15

9 Equivalent circuit for the skin-electrode contact. As an approximation, the skin electrode interface may be modelled electrically with a battery (B), resistance (R), and capacitance (C)....16

10 Effects of sympathetic and parasympathetic nerve stimulation on the slope of the pacemaker potential of an SA-node cell. Note that parasympathetic stimulation not only reduces the slope of the pacemaker potential but also lowers the "take off" point....19

11 Balance of sympathetic and parasympathetic forces....20

Figure **Page**

12 Upper thoracic sympathetic chain and the cardiac autonomic nerves on the right side in the dog.....20

13 Heart rate (H.R.) response of an anesthetized dog to steady stimulation of the cardiac sympathetic nerves at a frequency of 20 Hz for 30 seconds.....22

14 The change in heart rate evoked by trains of right vagal stimulation at frequencies of 7 and 10 Hz in a dog.....23

15 Time course of the change in P-P interval evoked by a brief burst of vagal stimuli in a dog.....23

16 The effects of vagal stimuli, delivered once each cardiac cycle, on the cardiac cycle length (P-P Interval) in the dog. The effect varied, depending on the P-St interval, which is the time after the onset of atrial depolarization (P wave).....24

17 Schematic depiction of the interaction between central and peripheral determinants of RSA. Solid lines depict excitatory effects; Dashed lines represent inhibitory effects. Waveforms illustrate the time varying patterns of activity at the respective sites. Lines from the cardiac and pulmonary depictions illustrate the trajectories of chemoreceptor and baroreceptor afferent and pulmonary stretch receptor afferent, respectively. Graphic inserts depict the frequency transfer functions of the cardiaceffector synapses, and the associated waveforms illustrate the transformations on the input functions. Exp.= expiratory phase; Insp.= inspiratory phase; n. IX & X = cranial nerves IX and X.....26

18 A standard sinusoidal wave with a 60 Hz frequency.....31

19 The demodulated signal from the signal shown in Figure 3.2.1a using 60-Hz as the demodulation frequency.....31

20 A 60 Hz sinusoidal signal wave distorted by the noise..... ...32

21 The demodulated components from the signal shown in Figure 3.2.1c using 60 Hz as the demodulation frequency.....32

Figure **Page**

22 The 50-point (5s) average of the respiration frequency response magnitude from the cs+ trials with a reference dotted line at the average of the 30s data before the pre-cs+ interval. The arrow points to the time where the shock was delivered.....33

23 A blood flow signal on the hand under a condition of the high-low temperature stimulation on the contralateral hand in a normal human subject.....35

24 Temperature signal represents the temperature alternations in a 30 s period, which is used as the stimuli on the hand.....35

25 Spectra of the blood flow and the temperature signals. The dotted line represents the spectrum of the temperature signal with a 30s period and the solid line is the spectrum of the blood signal.....35

26 Spectra of the blood flow and the temperature signals. The dotted line represents the spectrum of the temperature with a 40 s period and the solid line is the spectrum of the blood flow.....36

27 A change of the temperature stimulation on the hand represented by the temperature signal. The vertical axis has no unit since the signal from the thermistor was amplified and filtered.....37

28 The blood flow signal on the contralateral hand in response to the temperature change on the one hand as shown in Figure 3.3.3a.....38

29 Respiration-associated vagal changes in response to the temperature stimulation. The vagal changes are obtained from the heart rate variability signal using the complex demodulation.....38

30 (a) Power spectrum of heart rate fluctuations in the adult conscious dog. (b) Power spectrum of heart rate fluctuations under parasympathetic blockade and combined parasympathetic and sympathetic β-adrenergic blockade 40

31 An IBI signal from a normal subject walking at 2MPH.....44

32 A respiration signal from a normal subject walking at 2MPH.....44

33 Spectra of the IBI and respiration signals corresponding to the signals shown in Figure 4.3.1a and Figure 4.3.1b.....45

Figure **Page**

34 Vagal powers vs working loads (the unit of the working load is miles/hour). The negative number represents the number of the rest during the exercise....46

35 Suppression of pacemaker activity of an SA node by a brief, hyperpolarizing current pulse. (A) control cycle with a 640 msec period. (B) A hyperpolarizing pulse applied at an early phase accelerated the next charge. (C) A pulse applied at late phase slightly delayed next charge. (D) A pulse delivered at 67% of the spontaneous cycle terminated the next charge 49

36 A phase response curve (PRC) obtained from a purkinje fiber-sucrose gap preparation by scanning the pacemaker cycle with a brief subthreshold depolarization current pulses. B. Microelectrode recordings from the same preparation using current pulses of the same duration and amplitude but following a change of the steady state maximum diastolic potential to -60mV by the application of bias current. C. PRC from a complete scan in the run illustrated in B. The vertical line indicates the phase at which annihilation occurred....52

37 Data points from phase resetting runs carried out at 6 different stimulus amplitudes in one aggregate. Normalized perturbed cycle length (T_1/T_0) is plotted vs the normalized coupling interval ($\phi = t_c/T_0$). t_c is the stimulus time after the previous cycle. Crosses are placed midway through stimulus artifact which obscures action potential upstroke. solid lines are extrapolations based on results obtained in other aggregates and correspond to membrane reaching threshold during stimulus. Data points are found along dashed lines in A-C when phase-resetting run repeated....54

38 An idealized phase resetting paradigm. T_0 is the cycle without any perturbation. A stimulus delivered in the 3rd cycle delayed the next cycle ($T_a > T_0$) while a stimulus delivered in the 6th cycle advanced the following cycle ($T_b<T_0$)....58

39 Coupling intervals marked by coupling interval points. One respiration cycle is shown in the graph....62

40 An example to estimate phase of the heartbeat. A. Heart beat is represented by vertical bars. B. The IBI signal corresponding to the heart beats shown in A. C. A portion of the respiration cycle, in which a and b represent the coupling interval points....64

Figure **Page**

41 The running PRC and respiration stimuli. (a) sitting. (b) standing.....67

42 A sinusoidal wave with a period of 12 hours.....69

43 Time circle with a 12-hour period.....69

44 The compressed sinusoidal wave with a period of 12 hours, which provides the same information as Figure 6.4.1.....70

45 Time cycle with a period of 10 marked by coupling interval points.....70

46 PRCs projected into one respiration cycle. (a) sitting; (b) standing.....71

47 The mean PRC at different pacing rates. (a) sitting; (b) standing.....73

48 The running PRC with respiration stimuli at 8 BPM. (a) normal; (b) CFS..76

49 PRCs projected into one respiration cycle. (a) normal; (b) CFS.....78

50 The mean PRC. (a) normal; (b) CFS.....79

51 Relative standard deviation in normal and CFS group.....82

52 Phase planes during 8 BPM sitting. Dotted circles are the inner and outer layers. (a) normal; (b) CFS.....87

53 Phase planes during 12 BPM. The dotted circles represents the inner and outer layers.....89

54 Phase planes during 18 BPM sitting. (a) normal; (b) CFS.....91

55 A constant signal.....93

56 The Poincare map of a constant signal.....93

57 A sinusoidal wave.....95

58 The Poincare map of a sinusoidal wave.....95

59 A distorted sinusoidal wave.....96

Figure **Page**

60 The Poincare map of a distorted sinusoidal wave....96

61 Poincare maps of the PRC. (a) normal; (b) CFS....98

62 A 3-D view of phase plane. (a) normal; (b) CFS....101

63 Phase spaces of the PRCs. (a) normal; (b) CFS....102

64 A 3-D view of the relationship between phase shift, stimulus and coupling.... 104

65 Phase response curve divided by boxes....107

66 Probability density curve....108

67 The relation between entropy and boxsize....110

68 Calculation of the information dimension....112

69 Information dimensions for the normal and the CFS groups....112

70 The state-plane portraits in the normal coordinates. (a) for $\lambda_1<0$, $\lambda_2<0$; (b) for $\lambda_1<0$, $\lambda_2>0$; (c) λ_1 and λ_2 are complex with negative real parts; (d) λ_1 and λ_2 are purely imaginary....121

71 (a) A stable limit cycle; (b) An unstable limit cycle; (c) A semi-stable limit cycle....122

72 (a) Output of the Van Der Pol model. (b) Phase plane for the Van der Pol model, k=3.82, μ=0.2, ω=1.92....126

73 A Van Der Pol model in response to different impulse stimulus....128

74 The perturbation process. The solid line represents the stimulus. The dotted lines represent the phase marker....186

75 Phase response curves at different stimulus amplitudes....129

76 Phase planes during different nonlinearities....187

77 Phase planes related to the coupling ways....188

Figure **Page**

78 Phase planes for different coupling coefficients.....189

79 Phase planes for different coupling frequency ratios.....134

80 Car mileage for different cars.....137

81 An additive model relates mileage to weight and HP.....139

82 An additive model used to show the contributions of coupling interval, r-espiration stimulus and slope of respiration to the PRC.....142

83 The function B, amplitude and phase.....150

84 The function $A(r,f_0)$.....154

CHAPTER 1

INTRODUCTION

1.1 Introduction to Heart Rate Variability

Heart beats normally originate from the cardiac pacemaker. A complete heart beat is electrically displayed by an electrocardiogram (ECG). The heart rate is normally derived from the QRS complex of the ECG by measuring the R-R interval. The human heart rate is typically not constant with time as shown in Figure 1.1.1, since the cardiac pacemaker receives a rich supply of parasympathetic and sympathetic neural fibers [9]. The fluctuations in heart rate, known as heart rate variability, disclose activities of both the parasympathetic and sympathetic nervous systems. Generally, sympathetic input increases heart rate while parasympathetic input decreases it.

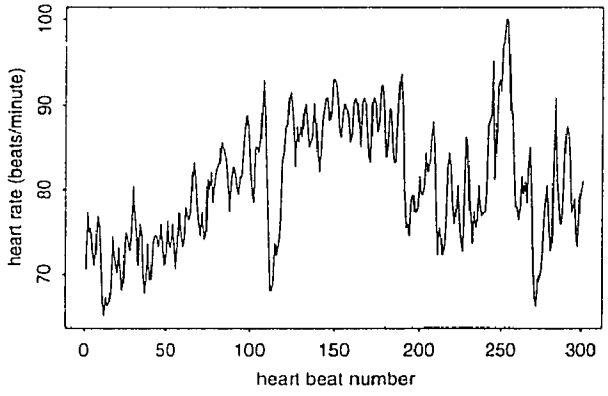

Figure 1.1.1 Heart rates of a young adult during rest. Total 300 beats are measured. x-axis is heart beat numbers, y-axis is heart rates (beats per minute).

The heart rate variability signal is formed by the transformation of the R-R

intervals into a time series. A typical procedure of this transformation is graphically shown in Figure 1.1.2 [1]. The basic steps are as follows: First, the R waves in the

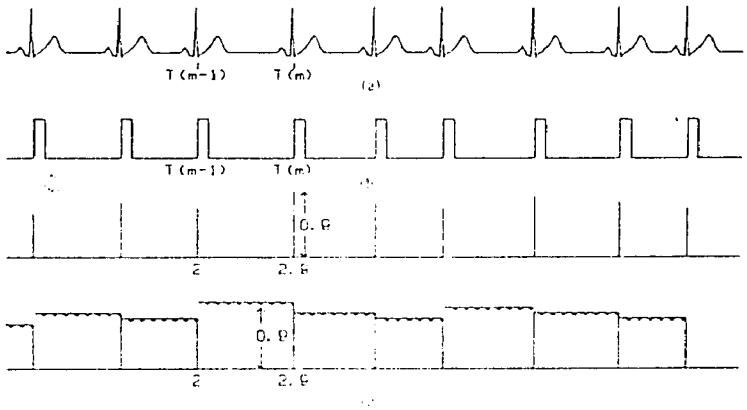

Figure 1.1.2 (a) ECG signal. (b) R-wave pulse train. (c) IBI values. (d) Interpolated IBI values. The dots in (d) represent interpolated data points.

ECG signal are detected as shown in Figure 1.2(b). A discrete interbeat interval (IBI) sequence is determined from the time between R waves and has samples only at the time when a heartbeat occurs as shown in Figure 1.2(c). Then the IBI sequence is interpolated into equidistant IBI samples (IBI signal) as though it were sampled from a series of step functions as shown Figure 1.2(d). Since there is always a very low trend in the IBI signal, which may affect the analytic result in time series analysis, it is normally removed in the signal processing and analysis. The heart rate variability signal shows oscillatory behavior reflecting different control mechanisms. A region of low frequency activity at around 0.04 Hz reflects thermoregulatory activity. Middle-frequency activity around 0.1 Hz is associated

with spontaneous vasomotor activity within the blood pressure control system. A region of activity which occurs at around 0.25 Hz is attributable to respiratory arrhythmia. The effects of respiration on heart rate are mediated through the vagal nerve of the parasympathetic system, also called the vagal system [1,2,3,9,17]. It is known that inspiration increases heart rate and expiration decreases heart rate. The respiration-associated heart rate variability (RA-HRV) has recently become a topic of considerable interest for investigations of normal physiology and disease [1,12,16,20,21,22,23,24] because the potential utility of RA-HRV as an index of vagal effects on the heart assumes special importance in understanding of the complexities of autonomic control.

1.2 Past and Current Trends of the Research

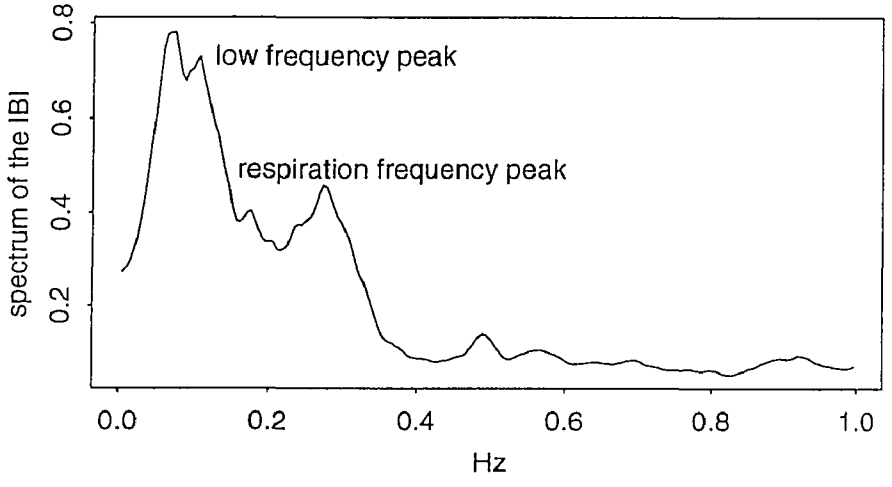

Figure 1.2.1 A spectrum of the heart rate variability signal. The corresponding heart rates shown in Figure 1.1.1

The RA-HRV has been quantified by conventional time-series techniques such as

power spectrum analysis and complex demodulation. Power spectrum analysis separates the power on the basis of the frequency components in the IBI signal. Using this method, we can separate the average power associated with respiration (which we call vagal power) from the rest of the signal [29]. Figure 1.2.1 shows a spectrum of the IBI signal from a subject at rest, in which there is a peak at the respiration frequency and the area under that peak represents the vagal power. Vagal influences on the heart can be measured by finding vagal power under different conditions [25]. Complex demodulation enables us to display the amplitude and phase of respiration frequency components of the IBI signal as functions of time. The demodulated amplitude indicates the intensity of the vagal actions on the heart across time [1]. Figure 1.2.2 displays an output of the complex demondulation from the IBI signal for a conditioned dog after a small shock. These techniques have been used in an effort to understand the role of vagal control of the heart in normal healthy subjects and in disease [1,15,17,18,19,25], and will be discussed in greater detail in the following chapters.

Figure 1.2.2 Anamplitude output of complex demodulation from the IBI signal for a conditioned dog after the shock. x-axis represents time.

Conventional time-series analysis of HRV has the following advantages:

(1) The intensity of RA-HRV is expressed by a power in the frequency domain

using spectrum analysis. The relation between the vagal power and the respiration frequency can be viewed.

(2) The activity of RA-HRV (vagal activity) is approximately displayed across time using complex demodulation. A rapid or significant change of the vagal activity can be studied.

However, a number of disadvantages need to be overcome:

(1) Conventional time-series analysis of HRV fails to take advantage of well-known characteristics of vagal-cardiac interaction. In fact, heart rate variations are due to perturbations to the cardiac oscillator. Cardiac cycles perturbed by respiration through the vagus nerve (vagal stimulation) generate RA-HRV. The change in length of the cardiac cycle depends on the intensity and timing of the perturbation or stimulus, which is called phase-dependency. Spectrum analysis and complex demodulation are not able to show this phenomenon.

(2) The lack of stationarity of the data constrains the data analysis using spectrum analysis and complex demodulation to a short period.

In this thesis, our major work is to examine the possibility that we can develop an analysis of HRV that incorporates the fact that the effects of vagal stimulation on the heart are phase-dependent. Also, other problems which were discussed above can be resolved. To better understand what we mean by phase dependence, consider that the sinoatrial node [SA node] of the heart acts as a self-sustaining oscillator. In the absence of stimuli the SA node progresses through its cycle,

exhibiting its own constant intrinsic rate. When a volley of vagal stimuli arrive at the SA node, their effect is to reset the cardiac cycle, which means that the initiation time of a cardiac cycle is changed. The initiation time of a cardiac cycle is called the phase of the cardiac cycle and a change of the initiation time of a cardiac cycle is a phase shift. The cardiac cycle can be either advanced or delayed depending upon the phase at which the vagal stimulation arrives. The phase of the stimulus is referred to the time of the stimulation in a cardiac cycle. Advancing the cardiac cycle increases heart rate, while delaying the cardiac cycle slows heart rate. Therefore, the phase of the cardiac cycle at the time of the vagal stimulation and the intensity of the vagal stimulation both play an important role in determining the heart rate. Although typically the vagus acts to slow heart rate, this is not always true. In 1934 Brown and Eccles [5] showed that vagal stimulation at the appropriate phase could accelerate the heart rate. Cardioacceleration due to vagal stimulation is a dramatic example of the phase-dependent nature of vagal effects on heart rate. To describe the phase-dependent effects of vagal action on cardiac resetting, Jalife and Glass [8,10] have examined the cardiac response to vagal stimulation across different phases of the cardiac cycle and constructed a phase response curve. The phase response curve (PRC) displays phase shifts at different phases of the stimulation, which is a function of stimulus phase, and stimulus amplitude. The phase response curve is a powerful tool to illustrate the phasic nature of the cardiac oscillator in response to brief vagal perturbations. Knowing the PRC gives us a great deal of information about the dynamics of the vagus-heart

system. Since phase dependence is an important characteristic of the effects of the vagus nerve on the heart, it would be valuable to examine the physiology and pathology of phase-dependent phenomena. This has become an area of considerable interest in physiology [2,4,11,12,13,26]. Recent studies, including the works of Winfree, Jalife & Antzelevitch, Guevara & Shrier & Glass, and etc.[4,6,7,12], have analyzed the phase dependence of cardiac tissue by either chemical or electrical assessment. The results indicate that the magnitude of the phase resetting depends on the amplitude, duration and timing of the stimulus.

Present studies of cardiac phase resetting are, however, all constrained to surgical preparations in animals or in vitro work [4,6,7,12]. Here we report a noninvasive human cardiac phase resetting study during paced-breathing. We pay particular attention to estimating the PRC of respiration related vagal effects on the heart in intact awake humans. As a result, it is possible to characterize the phase dependence of heart rate variability (HRV) under continuous vagal influence of respiration on the heart. Further we have developed several methods to analyze the PRC, which has been not done in previous studies.

1.3 The Scope of Our Research

Heart rate variability has, in recent studies, become a noninvasive assessment of the autonomic nervous system. Study of the respiration-associated heart rate variability (RV-HRV) provides important clues in understanding of the vagal control mechanisms of the heart. In this study, we will first cite two powerful

analytic techniques, spectrum analysis and complex demodulation, to access the vagal system using the heart rate variability signal. Then we will investigate a new approach, the phase response curve, which includes the advantages of spectrum analysis and complex demodulation but overcomes their disadvantages, to reveal the vagal control mechanisms on the heart. Therefore, a complete study of the vagal effects on the heart can be accomplished.

In this study, it is important to understand the physiological structure of the heart and autonomic branches including the sympathetic and vagal systems. In chapter 2, we will review the structure of the heart, neural effects on the heart and neural coupling between heart and lung. This background is helpful to understanding the later study of RA-HRV using conventional time-series techniques and the approach we have developed.

Study of the RA-HRV is a valuable approach to access the vagal control mechanism. Two powerful time-series techniques, complex demondulation and spectrum analysis, have been used to noninvasively quantify the vagal intensity using the heart rate variability signal. Each technique provides important information about vagal effects on the heart in a different manner. In chapter 3, we will introduce the complex demodulation technique. Complex demodulation can demodulate the RA-HRV from the heart rate variability signal in the time domain and is normally used to characterize changes of the vagal input over time. For effective usage of complex demodulation, a conditioning experiment that causes distinct vagal variation is introduced in this chapter and application of complex

demodulation is illustrated. Following complex demodulation, we will present spectrum analysis in chapter 4. Spectrum analysis is a Fourier transform based technique that can decompose the heart rate variability signal into frequency-related components in the frequency domain. The average power related to the respiration frequency or vagal power can be obtained in the spectrum. An experimental protocol, consisting of physical exercise with different walking speeds, is introduced and vagal powers at different exercise stages is discussed.

Vagal activity can be evaluated in the time domain using complex demodulation and in the frequency domain using spectrum analysis. Both spectrum analysis and complex demodulation have their short-comings. The major common drawback is that these two conventional techniques fail to show the phase dependent characteristics of the vagal-cardiac interaction. Chapter 5 gives a general review of recent development of phase dependent studies. In the review, we will try to abstract basics of the cardiac phase dependent nature in response to stimulation in animal experiments and to establish a theoretical foundation for our further study on human subjects. Chapter 5 also provides us with solid evidence of the cardiac phase dependence.

To noninvasively investigate the phase resetting behavior in the intact human, we have developed a paced-breathing protocol. This protocol is important to generate easily analyzable data, and will be described in detail in Chapter 6. Briefly, subjects were asked to breathe at a fixed rate. During the experiment, ECG and respiration signals were collected. The ECG signal was used to derive phasic

changes or phase shifts of the heart-beat, and the respiration signal was used to measure the strength of the respiration-related vagal stimulation. We then introduced the concept of phase-dependence and defined the concepts of phase, stimulus and coupling intervals. Based on the definitions and some assumptions, we began to estimate the running phase response curve (phase response curve corresponding to various respiration cycles). The estimated phase response curve (PRC) was used to display the general characteristics of phase-dependence of the heart rate on respiration. Many studies which are discussed in chapter 5 were limited to searching for a phase resetting pattern without further analysis. We have proposed several methods to explore the PRC analysis. Among them, a time circle method projects the PRC corresponding to every respiration cycle into one respiration cycle so that the common phase resetting behavior can be illustrated. The time circle method not only condensed repetitive or redundant information in the running PRC, but also demonstrated variations away from "common behavior". We have derived the common pattern of the PRC and analyzed the variations. Since the running PRC exhibited its oscillatory feature and dynamics of any oscillatory process could be easily demonstrated by its topological properties, we have presented topological methods in chapter 7 to unveil the topological properties of the running PRC. We have introduced phase plane and Poincare map techniques, and also discussed the 3-dimensional features of the cardiac phase resetting behavior.

Topological analysis also revealed nonlinear dynamic characteristics of the

running PRC. In Chapter 8, we developed a technique to analyze the nonlinear dynamics of the running PRC. The technique includes information entropy and information dimension calculations. Information entropy and dimension have proved to be a good measure of dynamical and chaotic activity underlying the phasic changes of the heart rate. Information dimension also provided us with information about system complexity.

To better understand the mechanism of phase resetting of the heart-beat due to respiration, we have investigated modeling and proposed several possible models such as the Van der Pol model, a nonparametric model called the generalized additive model, and Knight's and Peskin's models, which will be discussed in chapter 9. The modeling and simulation played a very important role in the explanation of the cardiac oscillatory system perturbed by a respiration stimulus.

To test their applicability, we have used all the methods we have developed to characterize and compare the normal group with subjects with chronic fatigue syndrome (CFS). CFS is a baffling and controversial illness that has been making headlines since the mid 1980's. It is a disabling chronic illness characterized by fatigue which is not the result of any medical conditions known to cause fatigue. Although it is believed that CFS has been in existence for over a century, the illness still remains cloaked in mystery. It is estimated that at least 100,000 Americans have the illness. Current investigations include various approaches in neurology, psychology and pathology. In this study, we also attempt to make a contribution to this area.

CHAPTER 2

BACKGROUND

2.1 The Heart and the Electrocardiogram

The human heart is divided longitudinally into right and left halves, each consisting of two chambers, an atrium and a ventricle. The architecture of the heart is shown in Figure 2.1.1.

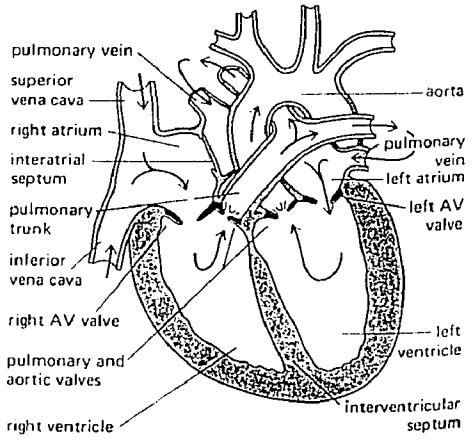

Figure 2.1.1 Diagrammatic section of the heart. The arrows indicate the direction of blood flow [9].

The origin of the normal heartbeat is generated from the conducting system of the heart, as shown in Figure 2.1.2. In this system, about 1% of cardiac muscle cells are autorhythmic, i.e. they are capable of autonomous rhythmical self-excitation. The important feature of such cells is gradual depolarization, which causes the membrane of the cells to reach a threshold potential and generate an action potential. The small mass of specialized cardiac muscle cells in the right

atrium is called the SA node, which is the normal pacemaker of the entire heart. From this cardiac pacemaker, the action potential spreads throughout both atria, reaching the AV node. The bundle of His, a conducting link between atria and ventricles, then carries the potential to the ventricles, causing the ventricles to contract. The spread of electrical activity throughout the cardiac tissue is recorded as an electrocardiogram (EKG) on the surface of the body.

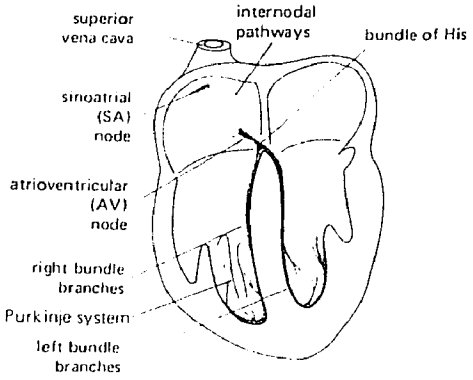

Figure 2.1.2 Conducting system of the heart. The interatrial conducting bundles are not shown in the figure [9].

An example of the normal EKG is shown in Figure 2.1.3. By convention, deflections within the overall periodic wave form of the EKG are referred to by the consecutive waves, P, QRS, and T in Figure 2.1.3. The P wave of the EKG originates from the electrical excitation of the atrium and reflects the spread of the impulse through the atria. From the SA node, the PQ interval indicates the slower rate of conduction through the AV node, whereas the small Q wave shows the spread of the ventricular impulse through the septum. The QRS complex originates from electrical excitation of the ventricles. The large QR wave represents a stage

of fast and full depolarization of the ventricle. The RS wave represents the return from the charged stage to a stage with no current flow, called isoelectric state. The ST segment represents the duration of the isoelectric state. Finally, the myocardium repolarizes and the T wave reflects the repolarization of the ventricle.

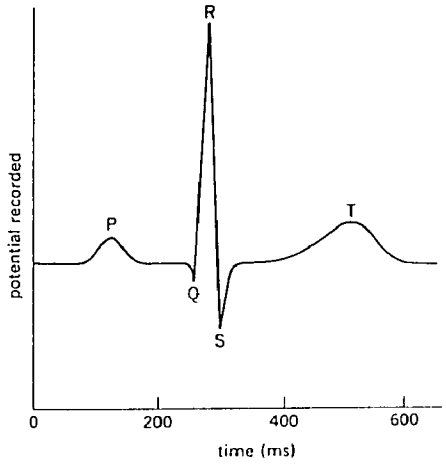

Figure 2.1.3 Typical electrocardiogram. P, atrial depolarization; QRS, ventricular depolarization; T, ventricular repolarization [9].

2.2 Measurement of the ECG

Measurement of the EKG is very important in understanding the origin of the cardiac events described above and to various clinical research. The EKG is usually measured by placing electrodes on the body surface. The quality of the measurement depends on electrode characteristics, number of leads, external noise, electrical equipment and technical skill.

A simple body surface EKG measurement in diagrammatic form is shown in Figure 2.2.1. Three electrode sites, on the left arm (LA), left leg (LL), and right leg (RL) are portrayed. The function of the amplifier (Amp) is to amplify the voltage difference between electrode leads LL and LA by a factor of about 500 so

that a "large" signal on the order of one volt can be displayed on a screen (S) or a recorder. The magnitude of the P wave is about 100 μV and the magnitudes of the QRS and T waves are approximately one millivolt. Most real amplifiers achieve this result by measuring the voltage difference between leads LL and RL and the difference between LA and RL, and then subtracting the latter difference from the former, which is used to diminish the effects of external noise.

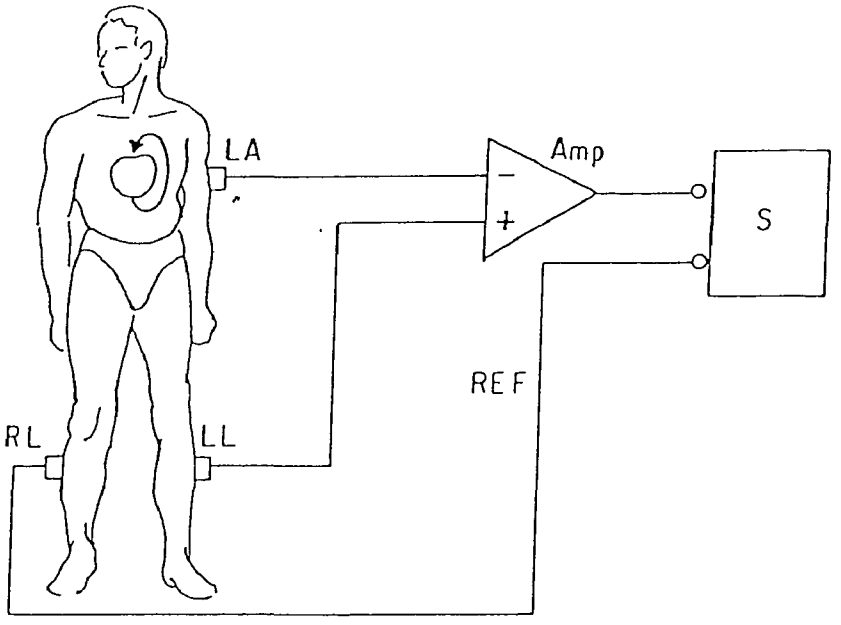

Figure 2.2.1 Idealized connections for making an ECG recording. The function of amplifier (Amp) is to amplify the voltage between the left arm (LA) and left leg (LL) electrodes by a factor of about 500. The right-leg electrode (RL) is a voltage reference [42].

Configuration of the lead system plays an important role for a quantitative EKG measurement. Early electrocardiographic investigators developed a common measurement protocol and standardized lead systems, known as Einthoven lead system: Lead I is the voltage measured between the left arm with respect to the right arm. Lead II is the voltage on the left leg with respect to the right arm. Lead

III is the voltage on the left leg with respect to the left arm. The precordial lead system is a set of six leads measured at standard anatomical locations across the anterior chess wall. The voltage at each of these sites is measured with respect to Wilson's central terminal. The Wilson's central terminal is formed by connecting electrodes on the right arm, left arm, and left leg to a common terminal though large resistors. The precordial lead system is also called the unipolar lead system. In addition, three augmented unipolar limb leads sometimes are used. The augmented leads use the right arm, left arm, and left leg, respectively, as the positive electrode and measure with respect to the average of the other two. Together the three limb leads, six precordial leads, and three augmented unipolar limb leads are referred to as the standard twelve-lead system. In practice, the selection of the lead system is determined by what information is required to be recorded.

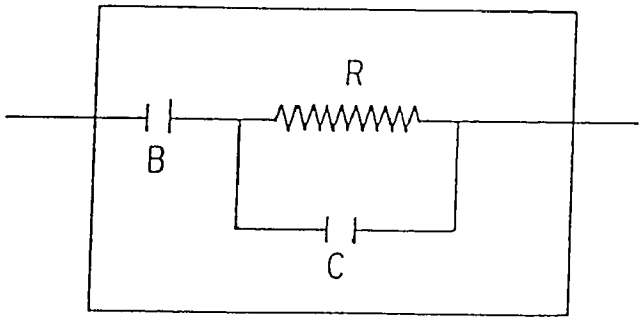

Figure 2.2.2 Equivalent circuit for the skin-electrode contact. As an approximation, the skin electrode interface may be modelled electrically with a battery (B), resistance (R), and capacitance (C) [42].

The interface between the electrodes and the skin tissue can be approximately modeled as shown in Figure 2.2.2. A battery B in the model

represents a voltage generated by the electrochemical interface between the skin tissue and the electrodes. The relative resistive and frequency-dependent properties of the skin can be modelled with a resistor R in parallel with a capacitor. Because of the dc voltage B, an EKG amplifier is normally designed to be ac coupled to the subject so that the effect of the dc voltage B can be eliminated. The resistor R is in the range from a few thousand to a few hundred thousand ohms. To accommodate that resistant, the EKG amplifier is required to have a high input impedance.

The EKG amplifier often incorporates a high-pass filter to eliminate the skin-electrode dc voltage and a low-pass filter to remove high-frequency noise, such as radio. The EKG amplifier is highly sensitive to 60-Hz noise. Such noise may be coupled capacitively from whatever power lines are in the vicinity to the subject or to the electrodes. The result is that the EKG often shows 60-Hz noise. Filtering 60-Hz noise is complicated and is done occasionally because the EKG wave form covers 60-Hz frequency band and a filter at 60-Hz may affect the original shape of the EKG. Filters may be analog or digital.

Signals from the EKG amplifier are often acquired by a computer. Evaluation of the frequency content of the EKG wave form is useful as a guide to the signal recording specification. More importantly, changes in the frequency content might be used as an indicator of changes in the underlying cardiac state. It is found that the frequency content of measured electrocardiograms shows most of the signal power under 100 Hz. There is a gradual decrease of power as

frequency increases. The power does not become zero at any frequency [42]. It is difficult to specify a maximum frequency beyond which there are no signals of cardiac origin to be found. This difficulty is due to small features of the electrocardiographic wave form close to the noise level. The uncertainty of the frequency content of the EKG is reflected in the data acquisition. The sampling rate in the data acquisition determines the accuracy of the data collection. Commonly used sampling rates range from 200 to 1000 samples per second.

The EKG is often used to study the rhythmic activity in the heart. The rate of heart beating rhythms is normally measured by the time difference between two consecutive R waves. Fluctuations of heart rate reflect different effects of the neural control on the heart. Heart rate variability can be measured in various ways, depending on the application. An important application is the study of the vagal activity using heart rate variability signal, which we will discuss in the rest of this thesis.

2.3 Neural Effects on the Heart

The rhythmic beating of the heart will have a constant rate in the complete absence of any nervous or hormonal influences. This is the inherent autonomous discharge rate of the cardiac pacemaker. However, the heart receives a rich supply of sympathetic and parasympathetic nerve fibers. The vagus nerve, subserving parasympathetic function to the heart, has a general inhibitory influence on the rate of cardiac impulse formation and on the velocity of conduction. The effects of

vagal stimulation are known as cholinergic responses, which tend to depress automaticity and conductivity within the heart. The sympathetic nervous system is just the reverse. Figure 2.3.1 illustrates the nature of the sympathetic and parasympathetic influence on the pacemaker, which directly causes changes of the heart rate. We note that parasympathetic stimulation not only reduces the slope of the pacemaker potential but also lowers the "take off" point.

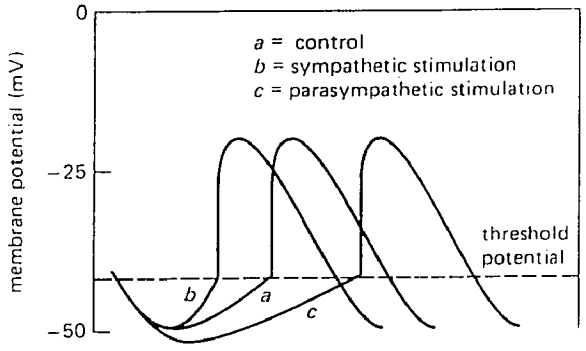

Figure 2.3.1 Effects of sympathetic and parasympathetic nerve stimulation on the slope of the pacemaker potential of an SA-node cell. Note that parasympathetic stimulation not only reduces the slope of the pacemaker potential but also lowers the "take off" point [9].

Because the cardiac pacemaker is normally under the constant influence of these nerves [9], the heart rate may be much lower or higher than that with no nervous influence. Figure 2.3.2. shows the influence of the vagus nerves and sympathetic nerves on the heart rate, in which vagus nerves slow the heart rate and sympathetic nerves speed up the heart rate. The central nervous system controls the relative levels of sympathetic and vagal activity in a reciprocal fashion [1]. When both divisions of the autonomic system are active simultaneously, the sympathetic

and vagal effects do not summate algebraically. Instead, nonlinear sympathetic-parasympathetic interactions are prominent [43].

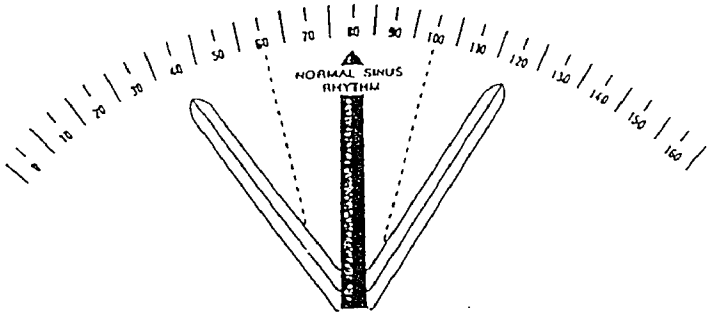

Figure 2.3.2 Balance of sympathetic and parasympathetic forces.

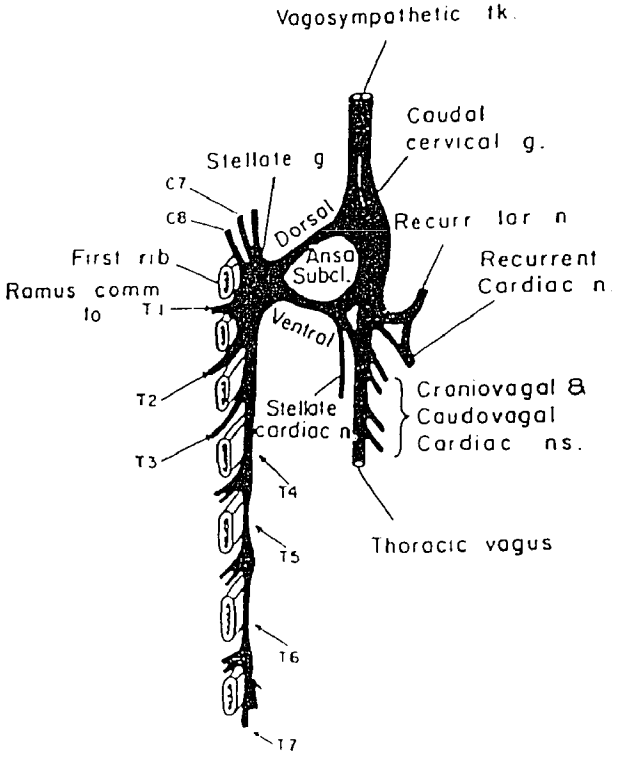

Figure 2.3.3 Upper thoracic sympathetic chain and the cardiac autonomic nerves on the right side in the dog [43].

The anatomy of the cardiac innervation is illustrated in Figure 2.3.3. The preganglionic cell bodies of the sympathetic fibers to the heart lie in the

intermediolateral columns of the first five or six thoracic segments of the spinal cord. The postganglionic sympathetic fibers travel to the heart as a complex plexus of small nerve bundles. The cell bodies of the preganglionic vagal neurons are located in the nucleus ambiguus. The preganglionic fibers exit from the skull, travel down the neck in the carotid sheaths, and enter the thorax. As they pass near the caudal cervical ganglia, the preganglionic vagal fibers become part of the cardiac plexus by forming a number of mixed nerve trunks along with postganglionic sympathetic fibers. The synapses between preganglionic and postganglionic vagal fibers occur in ganglia very close to, or actually within, the walls of the heart itself. Such ganglia are most abundant near the SA and AV nodes.

Sympathetic control of heart rate is facilitatory. The norepinephrine (NE) release from the sympathetic nerve endings in the SA node increase the firing rate of the cells in the node. This is accomplished by increasing the rate of slow diastolic depolarization. When the cardiac sympathetic nerves are stimulated by a long train of pulses, the heart rate begins to increase after a latent period of 1 to 3 seconds as shown for a dog in Figure 2.3.4. The steady-state level of the heart rate is not reached until about 30 to 60 seconds after the beginning of sympathetic stimulation. After removal of sympathetic stimulation, the chronotropic response gradually returns back to the control level. The magnitude of the positive chronotropic response to sympathetic stimulation varies with the stimulation frequency. The maximum response occurs with stimulation frequencies of 20-30 Hz.

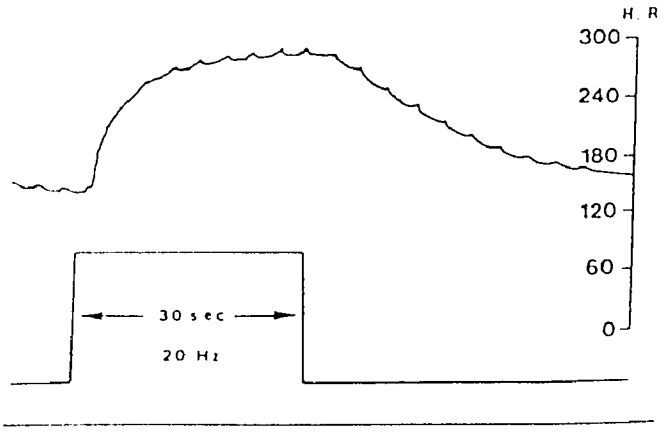

Figure 2.3.4 Heart rate (H.R.) response of an anesthetized dog to steady stimulation of the cardiac sympathetic nerves at a frequency of 20 Hz for 30 seconds [43].

In contrast to the rather slow chronotropic response to sympathetic stimulation, the latent period of the response to a train of vagal stimuli is only about 200 ms, and the steady-state heart rate is achieved within a few beats. Figure 2.3.5 shows variations of the heart rate in a dog in response to a train of vagal stimulation at frequencies of 7 and 10 Hz. When stimulation is removed, the response returns to control level rapidly. This is due to abundance of acetylcholinesterase (Ach) receptors in the nodal regions of the heart.

When a brief burst of stimuli is delivered to the vagus nerves, a triphasic chronotropic response of the heart rate in next 10-15 seconds occurs as shown in Figure 2.3.6. A brief but pronounced deceleratory phase (ABC) is followed by a short phase of relative or absolute cardiac acceleration (CDE), and then by a final small and more prolonged secondary phase of deceleration (EFG). Electrophysiologically, the phase of deceleration (ABC) is associated with a prologation of the sinoatrial conduction time and a hyperpolarization of the

automatic cells. The secondary phase (EFG) of cardiac deceleration is related to a reduction in slope of the pacemaker potential. In the acceleratory phase (CDE), the maximum diastolic potential of the pacemaker cells becomes slightly less negative. This transient acceleration might be ascribable to an evanescent increase in sodium conductance.

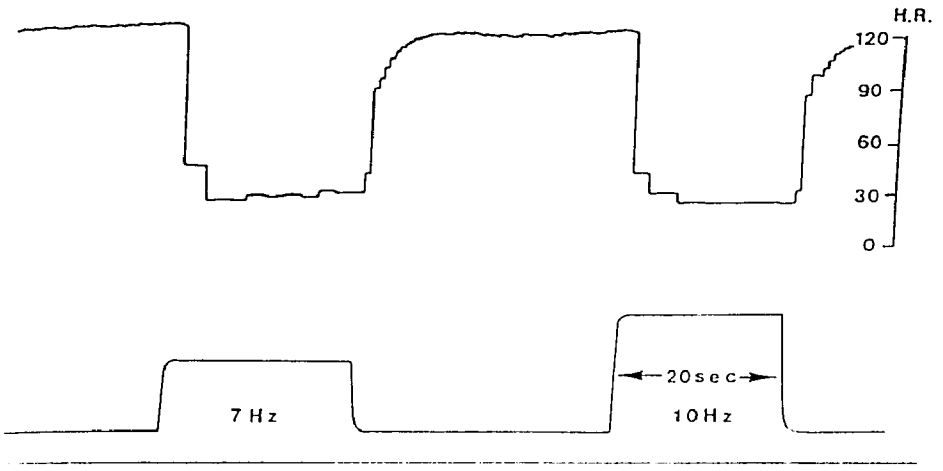

Figure 2.3.5 The change in heart rate evoked by trains of right vagal stimulation at frequencies of 7 and 10 Hz in a dog [43].

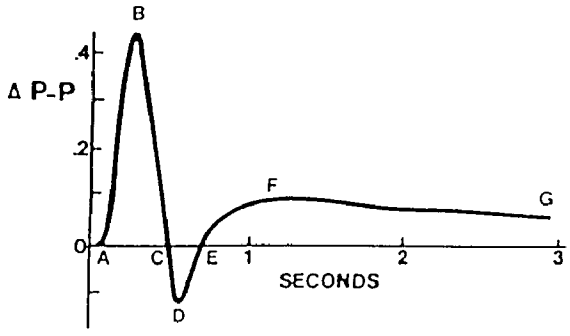

Figure 2.3.6 Time course of the change in P-P interval evoked by a brief burst of vagal stimuli in a dog [43].

Effects of repetitive vagal stimuli on the heart rate is illustrated in Figure 2.3.7, in which one stimulus was delivered to the cervical vagi of an anesthetized

dog during each cardiac cycle and the different P-P intervals are measured when each stimulus (St) is delivered at a different time after a P wave (P-St interval) in each cardiac cycle. Such a curve of P-P intervals, plotted as a function of the P-St interval, constitutes a phase response curve for the SA node pacemaker cells.

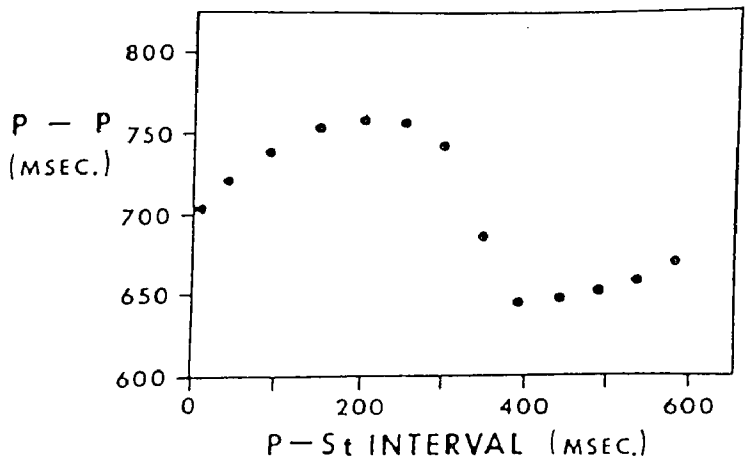

Figure 2.3.7 The effects of vagal stimuli, delivered once each cardiac cycle, on the cardiac cycle length (P-P interval) in the dog. The effect varied, depending on the P-St interval, which is the time after the onset of atrial depolarization (P wave) [43].

2.4 Neural Coupling between Cardiac Oscillatory System and Pulmonary System

There are many different vagal control schemes to change the heart rate, such as electrical, chemical and mechanical control. Generally fluctuations in the heart rate can be attributed to the modulation of blood pressure, thermoregulation, and respiration. Among them, the effect of respiration on the heart, respiratory sinus arrhythmia (RSA), has been known for a long time and holds considerable promise as a noninvasive index of vagal control that is derivable from the EKG signal.

Respiratory sinus arrhythmia arises from a complex interaction of central and

peripheral factors. Cardiorespiratory rhythm generators, tonic and phasic baroreceptor and chemoreceptor reflexes, cardiac and pulmonary stretch reflexes, and local mechanical and metabolic factors may all contribute to RSA. However, neural mechanisms play a far more dominant role in the determination of the RSA than nonneural mechanisms because RSA can be eliminated by autonomic denervation [33]. It is believed that a central respiratory generator can maintain heart period rhythmicity in the absence of peripheral inputs since many studies indicate that fluctuations in heart rate persist at the approximate respiratory frequency even in the absence of respiration or after pulmonary reflexes are eliminated [2]. An example is that heart-period rhythms within the typical respiratory frequency band persist even during complete breath hold.

The two central generators that are mostly associated with the respiratory and the cardiac rhythms are depicted in Figure 2.4.1, which shows the neural control paths of respiratory generator and sympathetic generator to the heart. In spite of the notable respiratory rhythms apparent in both sympathetic and vagal cardiac nerves, RSA is considered to arise largely or exclusively from fluctuations in vagal control. The reasons are (a) RSA is not generally attenuated by sympathectomy, (b) sympathetic contributions are seen only under conditions of depressed vagal control, (c) when present, sympathetic contributions are minimal, (d) sympathetic activity is usually limited at a frequency below 0.1 Hz and is not appreciably manifested in the respiratory frequency band (0.12-0.4 Hz). Vagal cardiomotor neurons are inhibited during the inspiratory phase and are activated

during expiration. In addition to central rhythm generators, peripheral baroreceptors and chemoreceptors also determine the heart rate and heart rate variability as shown in Figure 2.4.1. These peripheral inputs exert powerful excitatory effects on vagal cardiomotor neurons via central relays in the nucleus tractus solitarius. Therefore, both the central respiratory generator and pulmonary afferent modulate the vagal cardiomotor outflow and determine the RSA associated heart rate variability.

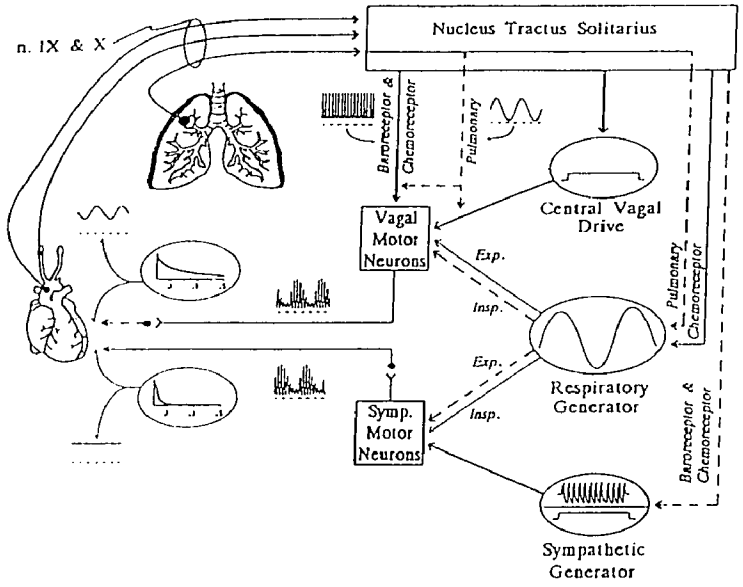

Figure 2.4.1 Schematic depiction of the interaction between central and peripheral determinants of RSA. Solid lines depict excitatory effects; dashed lines represent inhibitory effects. Waveforms illustrate the time varying patterns of activity at the respective sites. Lines from the cardiac and pulmonary depictions illustrate the trajectories of chemoreceptor and baroreceptor afferents and pulmonary stretch receptor afferents, respectively. Graphic inserts depict the frequency transfer functions of the cardioeffector synapses, and the associated waveforms illustrate the transformations on the input functions. EXP.= expiratory phase; Insp. = inspiratory phase; n. IX & X = cranial nerves IX and X.

Most often, inspiration, partially turning off vagal control, is associated with

an increment in heart rate, whereas expiration, partially turning on vagal control, is associated with a decrement in heart rate. The control mechanism is probably that oscillatory changes in the EKG induced by the respiration cycle may be associated with periodic discharge of afferent fibers in the lungs, producing vagal perturbations on the cardiac pacemaker [10]. Therefore interaction between heart and lung is a neural coupling through the vagus. The effects of respiration on the heart rate can be evaluated noninvasively by studying RSA in the heart rate variability signal.

Examination of the RSA data is important. Individual differences in RSA have been interpreted as reflecting differences in basal cardiac vagal tone, and changes of the RSA have been suggested to reflect corresponding alterations in the cardiac vagal tone. This interpretation is based on the fact that changes in tonic vagal activity yields the corresponding changes in the RSA. In the past decade, an increasing number of studies of the RSA have appeared in the physiological, psychological and clinical literatures. These studies have utilized RSA as an index of vagal control of the heart. In the following, we will introduce two conventional time-series techniques we have used to study the RSA. These two techniques are complex demodulation and spectrum analysis.

CHAPTER 3

HEART RATE VARIABILITY STUDY USING COMPLEX DEMODULATION

3.1 Introduction

Complex demodulation is a time series technique which estimates the instantaneous amplitude and phase of a given frequency in a time series [30,44]. The demodulated amplitude and phase of the given frequency in the signal can be expressed in the time domain. In the demodulated series, the variation of the amplitude represents intensity changes of the given frequency over time while change of the phase indicates the frequency variation around the given frequency. Since complex demodulation can provide us with information about instantaneous change of a given-frequency-related activity in a signal, we can use this method to derive information about the respiration-frequency-associated vagal activity in the IBI signal.

3.2 Complex Demodulation

The theory of complex demodulation can be found in detail in Bloomfield's book [30]. When a multi-frequency signal is multiplied by a given single frequency signal, in which the given frequency is one of the frequencies in the multi-frequency signal, the resulting d.c. component will be the demodulated component of the given-frequency in the multi-frequency signal. Mathematically, a multi-frequency signal can be represented by

$$s(t)=\sum_{k=1}^{n} A_k \cos(f_k t+a_k) \qquad (3.2.1)$$

where f_k is the frequency, a_k is the phase and A_k is the amplitude of a signal with a frequency of f_k. The representation in (3.2.1) can be expressed in the following complex form using the Euler expansion:

$$s(t)=\sum_{k=1}^{n} \frac{A_k}{2}\left[e^{i(f_k t+a_k)}+e^{-i(f_k t+a_k)}\right] \qquad (3.2.2)$$

The component with a frequency of f_m in the signal $s(t)$ can be complex demodulated by multiplying $s(t)$ by the following complex expression:

$$x(t)=2e^{-if_m t} \qquad (3.2.3)$$

Then

$$\begin{aligned} y(t) &= s(t)x(t) \\ &= \sum_{k=1}^{n} A_k\left[e^{i(f_k t-f_m t+a_k)}+e^{-i(f_k t+f_m t+a_k)}\right] \\ &= A_m e^{ia_m}+A_m e^{-i(2f_m t+a_m)} \\ &\quad +\sum_{k\neq m} A_k\left[e^{i(f_k t+f_m t+a_k)}+e^{-i(f_k t-f_m t+a_k)}\right] \end{aligned} \qquad (3.2.4)$$

When the resulting $y(t)$ passes through a low pass filter, the following component, called $z(t)$ remains:

$$z(t) = A_m e^{ia_m} \qquad (3.2.5)$$

Therefore, the amplitude and phase of the component with frequency f_m in the signal *s(t)* are extracted. The amplitude is

$$A_m = |z(t)| \qquad (3.2.6)$$

and the phase is

$$a_m = \tan^{-1}\left[\frac{\Im z(t)}{\Re z(t)}\right] \qquad (3.2.7)$$

In practice, the amplitude A_m and the phase a_m are varying with time. Thus, the demodulated result contains not only the d.c. component, but also the slow components around the given frequency. The actual result depends on the bandwidth of the lowpass filter. In order to illustrate the application of the complex demodulation technique, we first present some examples, which are shown in Figures 3.2.1a-d.

Figure 3.2.1a is a one second interval sinusoidal wave with a fixed frequency of 60 Hz. We used a 60 Hz signal to demodulate the 60 Hz component in the sinusoid, and the result was a constant amplitude as shown in Figure 3.2.1b because the sinusoid contained only the 60 Hz component whose amplitude didn't vary with time.

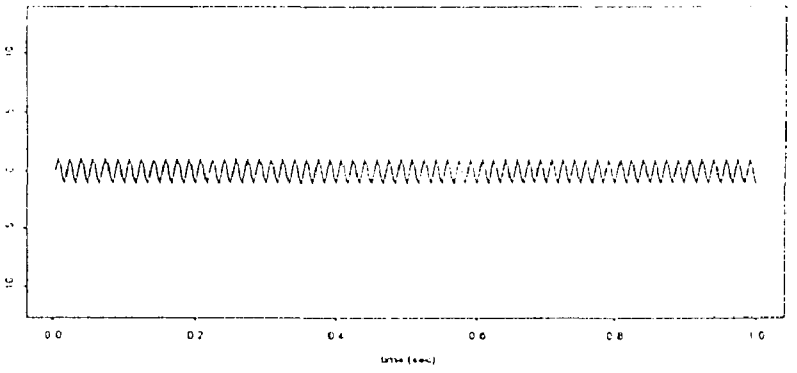

Figure 3.2.1a A standard sinusoidal wave with a 60 Hz frequency.

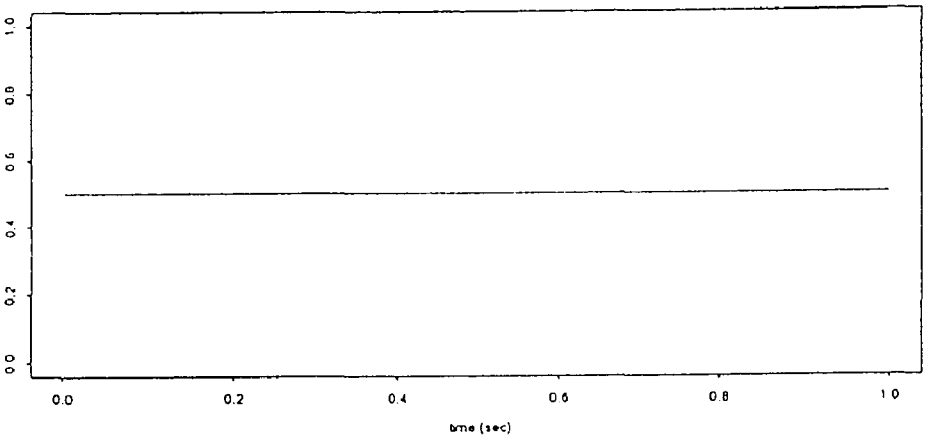

Figure 3.2.1b The demodulated signal from the signal shown in Figure 3.2.1a using 60 Hz as the demodulation frequency.

Figure 3.2.1c shows a signal of one second duration with a 60 Hz oscillation distorted by white noise in the middle of the one second interval. When we used the same 60 Hz signal to demodulate the 60 Hz component from the distorted wave, we found that the demodulated component had a trough at the time corresponding to the distorted portion of the oscillation as shown in Figure 3.2.1d. We could then conclude that the amplitude of the 60 Hz component in that portion of distorted oscillation was very small. Therefore the demodulated component at a given frequency can demonstrate the instantaneous amplitude as well as changes of the amplitude of a certain-frequency-associated component.

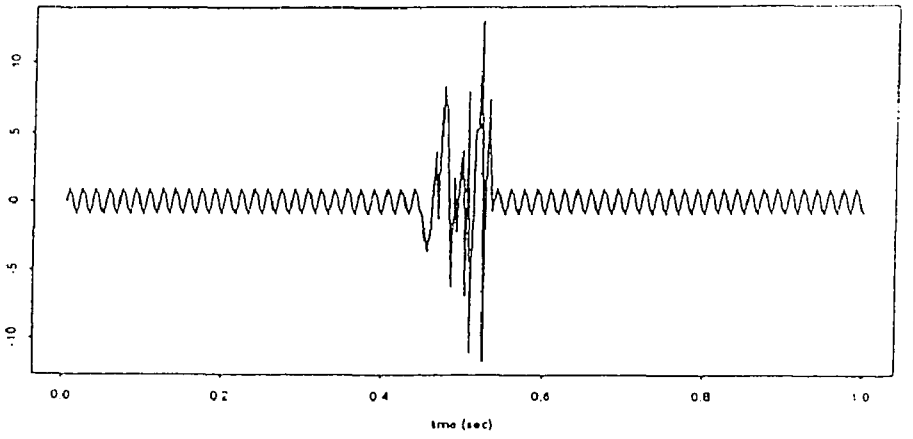

Figure 3.2.1c A 60 Hz sinusoidal signal wave distorted by the noise.

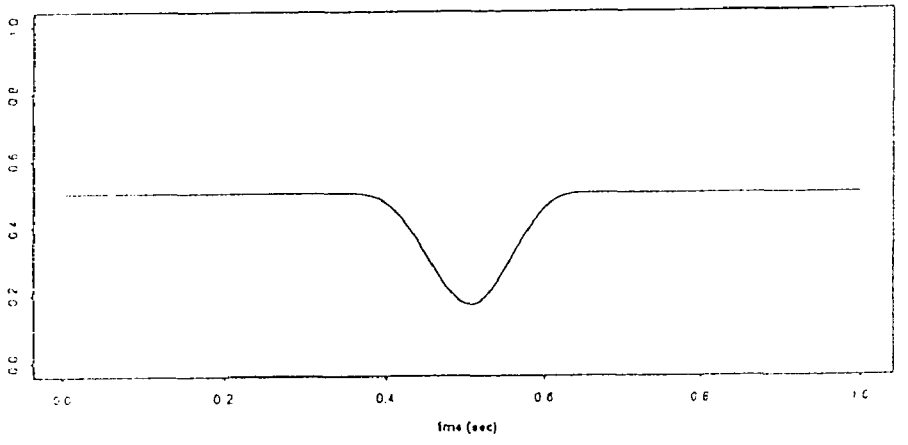

Figure 3.2.1d The demodulated components from the signal shown in Figure 3.2.1c using 60 Hz as the demodulation frequency.

3.3 Applications of Complex Demodulation

Because of the properties described above, complex demodulation has been used to characterize the changes of autonomic input to the regulation of heart rate over time. An example can be found in the study of heart rate response to classical conditioning [1]. In the experiment, a group of dogs received training on a differential classical conditioning task in which a tone, identified by cs^{+}, was generated simutaneously with an electrical shock administered to the flank of the

animal. When the animal is conditioned, it learned that the cs^+ tone reliably predicted a shock and produced vagal response.

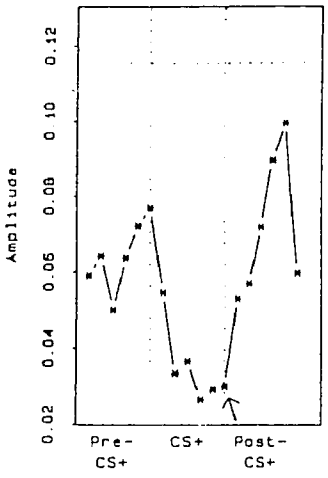

Figure 3.3.1 The 50-point (5 s) average of the respiration frequency response magnitude from the cs+ trials with a reference dotted line at the average of the 30 s data before the pre-cs+ interval. The arrow points to the time where the shock was delivered.

Figure 3.3.1 shows vagal responses in three different periods, a 30-second pre-cs^+ without a tone, a 30-second cs^+ with a tone, and a 30-second post-cs^+ with a shock at end of the cs^+ period. The curve shown in Figure 3.3.1 is the amplitude of the respiration frequency response and is derived from the complex-demodulated component in the IBI signal by averaging its amplitude in every 5 seconds. It is noticed that vagal response drops significantly during the cs^+ period and increases during the post-cs^+ period. In this conditioning experiment, complex demodulation successfully illustrated the highly dynamic vagal changes of heart rate associated with respiration. It is of considerable physiological interest to study situations using complex demodulation, where heart rate changes dramatically over time and the control of these changes.

We have used the complex demodulation technique in a conditioning study called thermal entrainment analysis. Entrainment is a phenomenon where an oscillating system exhibits a strong oscillation when a stimulus is applied to the system at a frequency approaching the system's natural resonant frequency. The study has shown that by applying a certain range of periodic thermal stimuli to one hand the spontaneous variations in blood flow in the contralateral hand could be suppressed and replaced by strong oscillations occurring at the same frequency as the stimulus [31]. This phenomenon is called thermal entrainment. We have measured peripheral blood flow and found that the spontaneous blood flow oscillation occurs in the range from 0.02 Hz to 0.04 Hz. We then carried out experiment to study characteristics of vagal activity during the thermal entrainment.

A thermistor was attached to the forefinger of the right hand and a photoelectric plethysmograph to the distal phalanx of the forefinger of the left hand. The right hand was then immersed alternatively in a cold water bath for 15 seconds and back to air for another 15 seconds, that is, the thermal stimulus had a period of 30 seconds or a frequency of 0.033 Hz. The experiment was repeated with a thermal stimulus at a period of 40 seconds or 0.025 Hz.

Figure 3.3.2a shows the blood flow signal when a thermal stimulus was applied with a period of 30 seconds. Figure 3.3.2b displays the temperature signal with a period of 30 seconds, which was used as the stimulus to entrain the blood flow. The entrainment phenomenon can be illustrated by comparing the spectra shown in Figure 3.3.2c and Figure 3.3.2d. Figure 3.3.2c shows spectra of both the

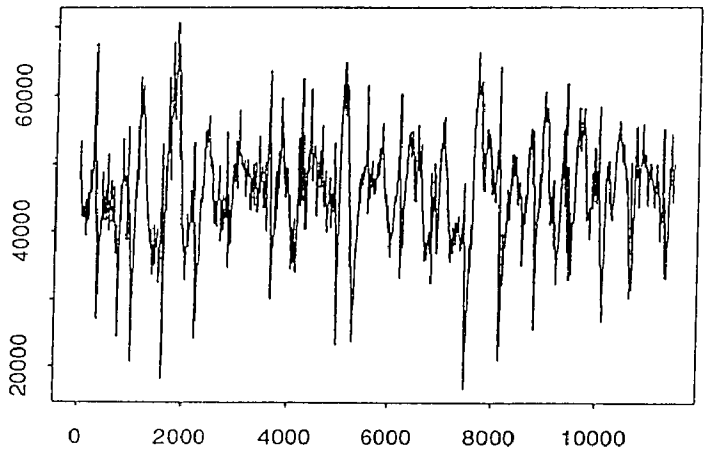

Figure 3.3.2a A blood flow signal on the hand under a condition of the high-low temperature stimulation on the contralateral hand in a normal human subject (sampling rate is 50Hz).

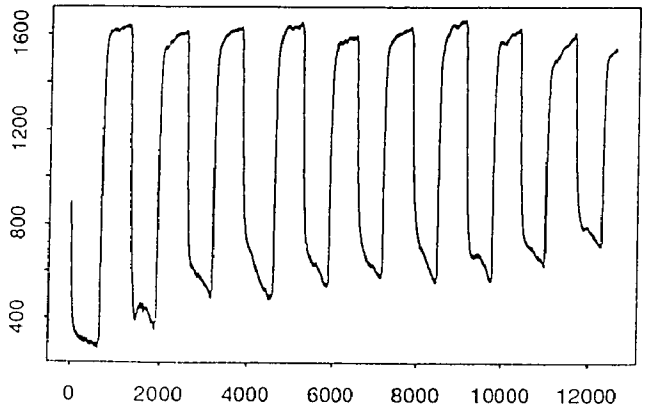

Figure 3.3.2b Temperature signal represents the temperature alternations in a 30s period, which is used as the stimuli on the hand (sampling rate is 50 Hz).

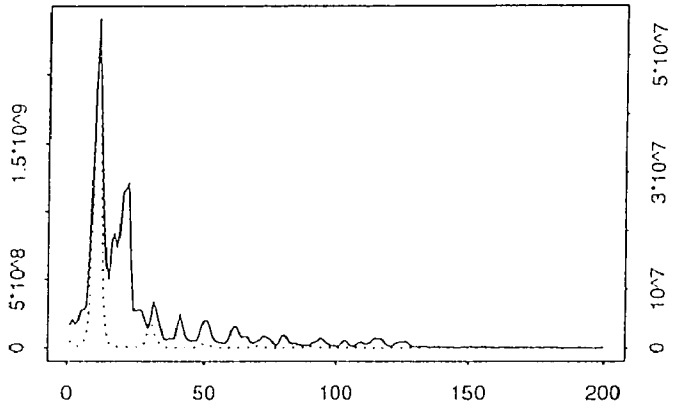

Figure 3.3.2c Spectra of the blood flow and the temperature signals. The dotted line represents the spectrum of the temperature signal with a 30 s period and the solid line is the spectrum of the blood signal.

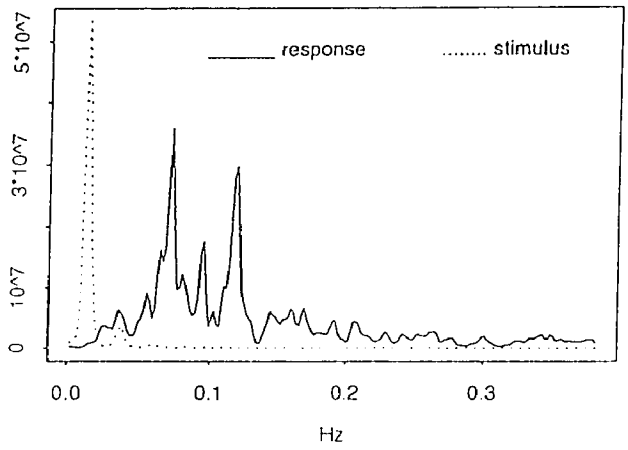

Figure 3.3.2d Spectra of the blood flow and the temperature signals. The dotted line represents the spectrum of the temperature with a 40s period and the solid line is the spectrum of the blood flow.

temperature and the blood flow during the entrainment, in which the temperature signal has a period of 30 seconds. It is observed that there is a large peak in the spectrum of the blood flow corresponding to the peak of the spectrum of the temperature signal, which implies that the blood flow is entrained at the frequency of the temperature signal. Figure 3,3.2d shows spectra of both the temperature and the blood flow without entrainment, in which the temperature signal has a period of 40 seconds. We have found that at the peak of the spectrum of the temperature there is no obvious peak in the spectrum of the blood flow, which is a good indication of nonentrainment.

The above experiment suggested that cold temperature could be used as a stimulus to regulate thermal activities in the human body, which could then affect the vagal activity. Subjects were therefore asked to sit quietly for 4 minutes, followed by immersing their right hand in a cold water with 4 ^{0}C bath for another

4 minutes. Their hands were then returned to air for a 24-minute recovery period. During each stage we measured both EKG and respiration signals. EKG was used to derive the interbeat interval (IBI) signal, following the basic steps described in Chapter 1. We complex demodulated the IBI signal at 0.28 Hz with a low-pass filter that has a cut-off frequency of 0.16 Hz so that the range of the respiration frequency peak (0.12-0.44 Hz) was covered. Figures 3.3.3a and 3.3.3b display the temperature signal as the thermal stimulus on one hand and the subsequent blood flow on the contralateral hand of a normal subject. Figure 3.3.3c shows the complex demodulated vagal activity in the form of the amplitude of the respiration frequency response to the thermal stimulation. It is found that vagal activity decreases significantly when the cold water stimulation is given. After removal of the stimulation, the vagal activity starts to increase and recover to the previous level before the stimulation.

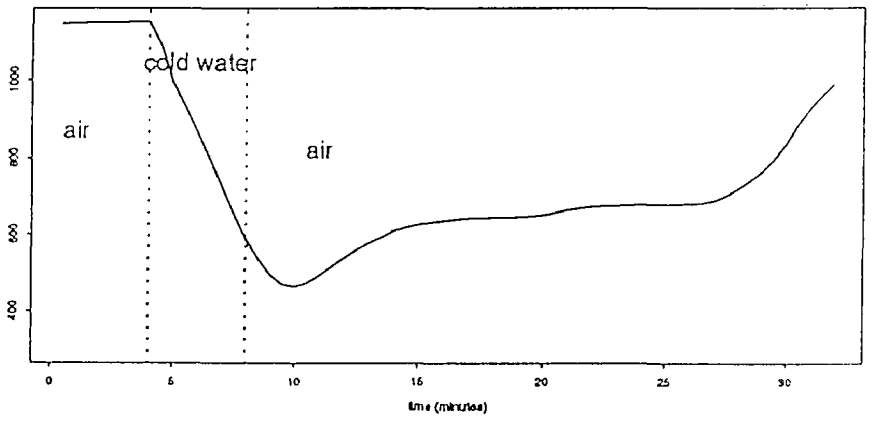

Figure 3.3.3a A change of the temperature stimulation on one hand represented by the temperature signal. The vertical axis has no unit since the signal from the thermistor was amplified and filtered.

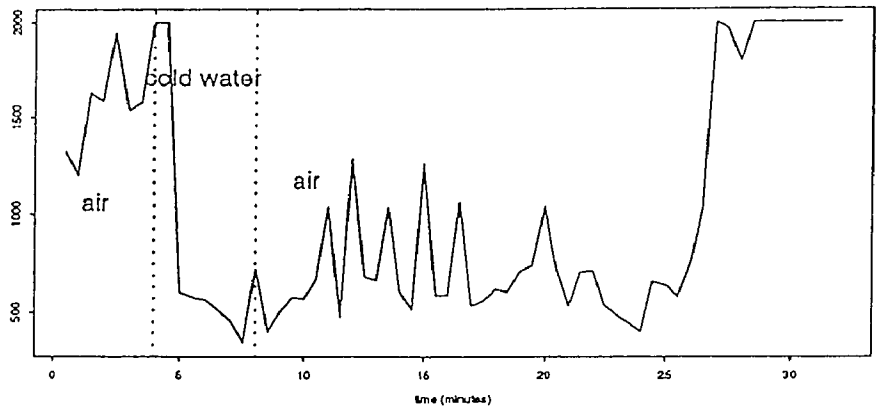

Figure 3.3.3b The blood flow signal on the contralateral hand in response to the temperature change on the one hand as shown in Figure 3.3.3a.

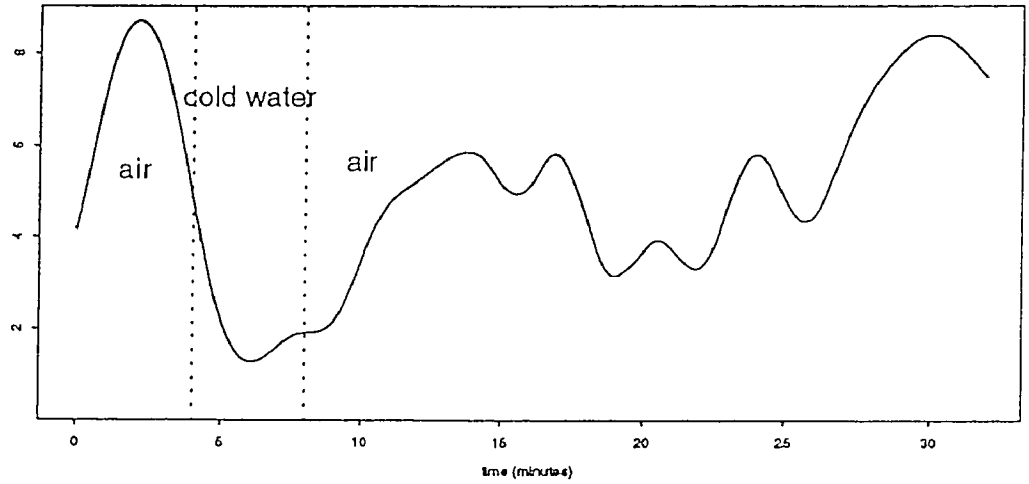

Figure 3.3.3c Respiration-associated vagal changes in response to the temperature stimulation. The vagal changes are obtained from the heart rate variability signal using the complex demodulation.

Therefore, changes of vagal activity with changes of stimulus condition can be clearly observed in the time domain using complex demodulation. Therefore complex demodulation is a valuable tool to examine the change of vagal activity under various conditioning situations in the time domain.

CHAPTER 4

SPECTRUM ANALYSIS OF HEART RATE VARIABILITY

4.1 Introduction

Spectrum analysis is an analytical method based on the Fourier transform. The Fourier transform is a function that decomposes a signal into a set of sinusoidal components corresponding to different frequencies. The amplitude of each decomposed sinusoidal component describes the intensity of the sinusoidal wave at its frequency, while the phase of each decomposed sinusoidal component specifies the starting point in the sinusoid's cycle. Spectrum analysis allows us to find the power densities of decomposed components in the frequency region of interest. Because a signal can be decomposed into many components based on their frequencies and expressed in the spectrum, the power in a certain frequency region can be derived from the spectrum by computing the area in that region. Thus, the Fourier transform can be used to identify the regular contributions to a fluctuating signal, thereby helping to make sense of observations in diverse fields of science [32]. One of the applications of spectrum analysis is the study of heart rate variability.

It has been recognized that heart rate variability is usually due to the neural effects of blood pressure, thermoregulation and respiration on the heart. Study of heart rate variability can help to assess the parasympathetic and sympathetic systems. The power spectrum of the heart rate variability signal contains

identifiable peaks at different frequencies associated with cyclic fluctuations in peripheral vasomotor tone (thermoregulation), the frequency response of the baroreceptor reflex (blood pressure) and respiration frequency, which is shown in Figure 4.1.1.

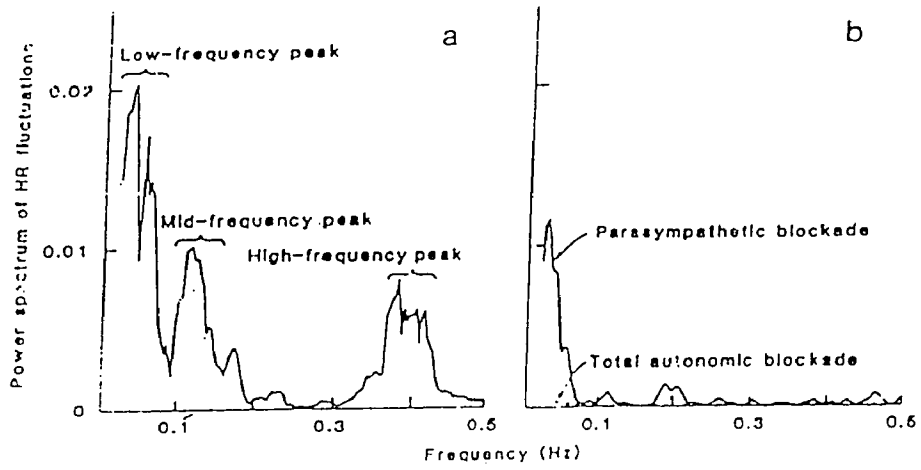

Figure 4.1.1 (a) Power spectrum of heart rate fluctuations in the adult conscious dog. (b) Power spectrum of heart rate fluctuations under parasympathetic blockade and combined parasympathetic and sympathetic β-adrenergic blockade [25].

Figure 4.1.1a displays a power spectrum of the heart rate variability signal in the adult conscious dog. The low-frequency peak is related to variations in peripheral vasomotor tone associated with thermoregulation, the mid-frequency peak is related to the frequency response of the baroreceptor reflex, and the high-frequency peak is centered at the respiration frequency. Further the respiration-related peak of the power spectrum of the IBI variations vanishes under

parasympathetic blockade as shown in Figure 4.1.1b [33]. This fact suggests that heart rate variability in response to respiration is a pure parasympathetic control process. An experiment will be described concerning quantitative measurement of the respiration-related contribution to the power spectrum of the heart rate variability signal in humans.

4.2 Experiment and Method

12 controls and 12 multiple sclerosis (MS) patients were selected. Subjects were asked to dress in shorts and sports shoes and walked on a treadmill. All exercise tests were carried out at room temperature. 2 protocols were used, depending on the subject's physical condition.

Protocol 1:	Rest	1MPH	2MPH	Rest	1.5MPH	2.5MPH	3MPH	Rest
	5 min	4 min	4 min	4 min	4 min	4 min	4 min	10 min

Protocol 2:	Rest	1MPH	2MPH	2.5MPH	3MPH	Rest	3.5MPH	4MPH	Rest
	5 min	4 min	4 min	4 min	4 min	4 min	4 min	4min	10 min

Protocol 1 was 5-minute rest, followed by 4-minute exercise interval at 1 mile per hour (MPH), 2MPH, rest, 1.5 MPH, 2.5 MPH, 3MPH. If possible, elevation was added cumulatively every minute after 3MPH in order to push the subject to a maximum fatigue. Protocol 2 was 5-minute rest, followed by 4-minute exercise interval at 1MPH, 2MPH, 2.5MPH, 3MPH, rest, 3.5MPH and 4MPH, each

for a 4-minute period. If possible, elevation was added cumulatively every minute after 4MPH in order to push the subject to a maximum fatigue. Both protocols ended with a 10-minute rest, which we call the recovery period. During the test, ECG, EMG, respiration, skin temperature, oxygen consumption, subjective perceived exertion, blood pressure and cadence were measured. The respiration signal was measured by placing two electrodes on the chest and variation in the chest impedance was transformed into voltage changes via the Resp1 Monitor (UFI, Inc., Morrow Bay, CA). The standard 12-lead system and Picker/Cambridge Test System were used to measure the EKG. The EKG and respiration signals were then digitized by a 12-bit A/D converter (DASH16, MetraBytes, Inc.) and input into an IBM personal computer. An 8-channel Sony instrumentation tape recorder was utilized to record the EKG and respiration signals as a back-up system. The digitized EKG and respiration data in the PC were transferred by the file transfer protocol (FTP) to a Sun Sparc station 1 where the data processing and analysis were performed.

The interbeat interval signal was derived from the EKG. The basic steps have been introduced in Chapter 1. The IBI signal usually contains some very low frequency components between dc and 0.00158 Hz. These very low frequency components sometimes occupy much power in the spectrum of the IBI signal and make it difficult to visualize the respiration frequency peak. We have designed a detrending procedure using a locally weighted robust regression (LWRR) method to filter out these very low frequency components. The LWRR gives a robust and

local smoothing of scatter plot data. In the LWRR, we chose 0.1 as the fraction of data used for smoothing at each data point, two as the number of iterations used in computing robust estimates, and 5% of the range of the data as the interval size used in the computing estimates. The detrended IBI signal was the IBI signal after the subtraction of the output of the LWRR and was ready for windowing. Windowing is a preprocessing of the time series before the Fourier transform. The direct Fourier transform of finite time series without windowing usually has large frequency leakage. The frequency leakage can be reduced by windowing. The procedure of windowing is to multiply the finite time series by a finite width window in the time domain. Selection of the proper window can result in the reduction of frequency leakage of the Fourier transform. In our study, we selected the Hanning window since it is widely used, easily implemented and gave us satisfactory results. The Fourier transform is performed numerically using the Fast Fourier Transform (FFT) algorithm. The FFT minimizes the number of multiplications in the transform and significantly increases the computing speed. The detailed FFT procedure may be found in many books [45]. The power spectrum contains the amplitudes of the decomposed components of the FFT and displayed the power density in the frequency domain.

4.3 Vagal Activity Study Using the Power Spectrum

The data used in the studies of spectrum analysis of heart rate variability and vagal activity were the IBI and respiration signals. Typical data during physical excise

is illustrated in Figure 4.3.1, which is obtained from a normal subject walking at 2 MPH.

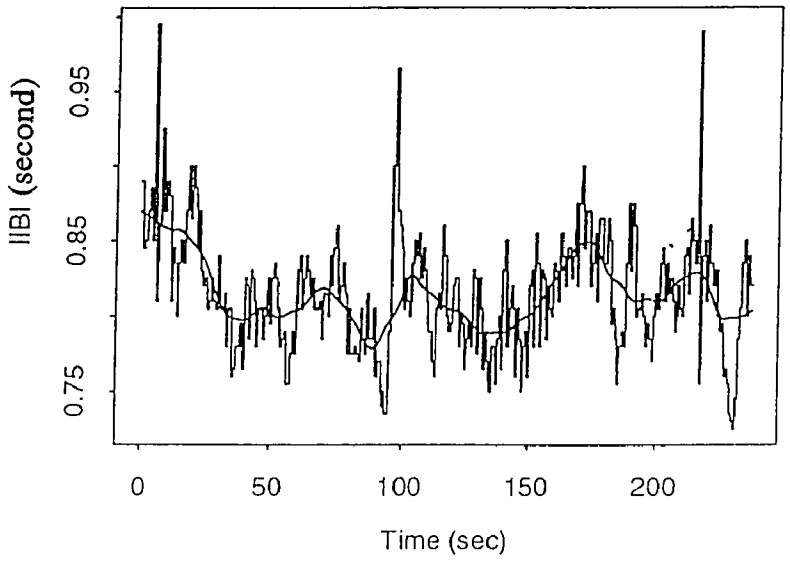

Figure 4.3.1a An IBI signal from a normal subject walking at 2 MPH.

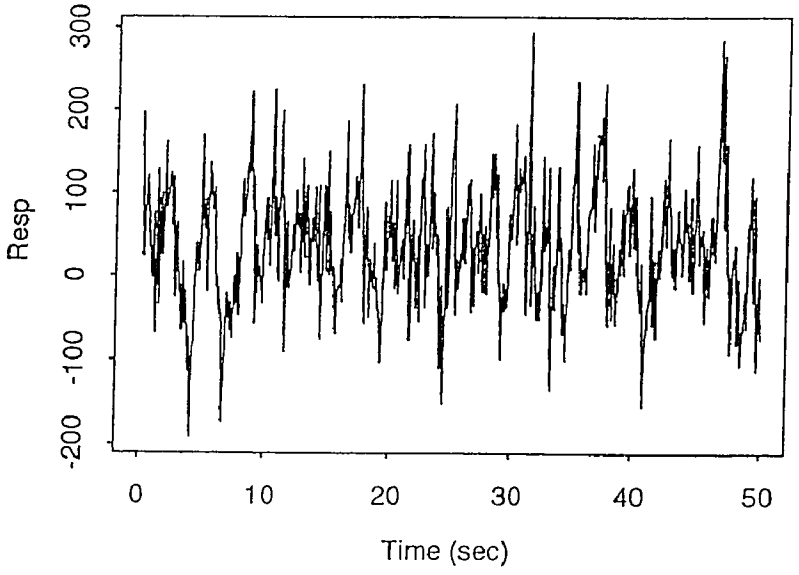

Figure 4.3.1b A respiration signal from a normal subject walking at 2 MPH.

Figure 4.3.1a is the IBI signal constructed by the procedures outlined in Chapter 1. The line which crosses the IBI signal is the detrending line, which represents the very low frequency trends in the IBI signal and needs to be removed

before the Fourier transform action is applied. Figure 4.3.1b is the respiration signal. The noise on the respiration signal might be due to body movement, but will not affect the identification of the respiration frequency in the spectrum of the respiration signal as shown in Figure 4.3.1c. Figure 4.3.1c shows power spectra of

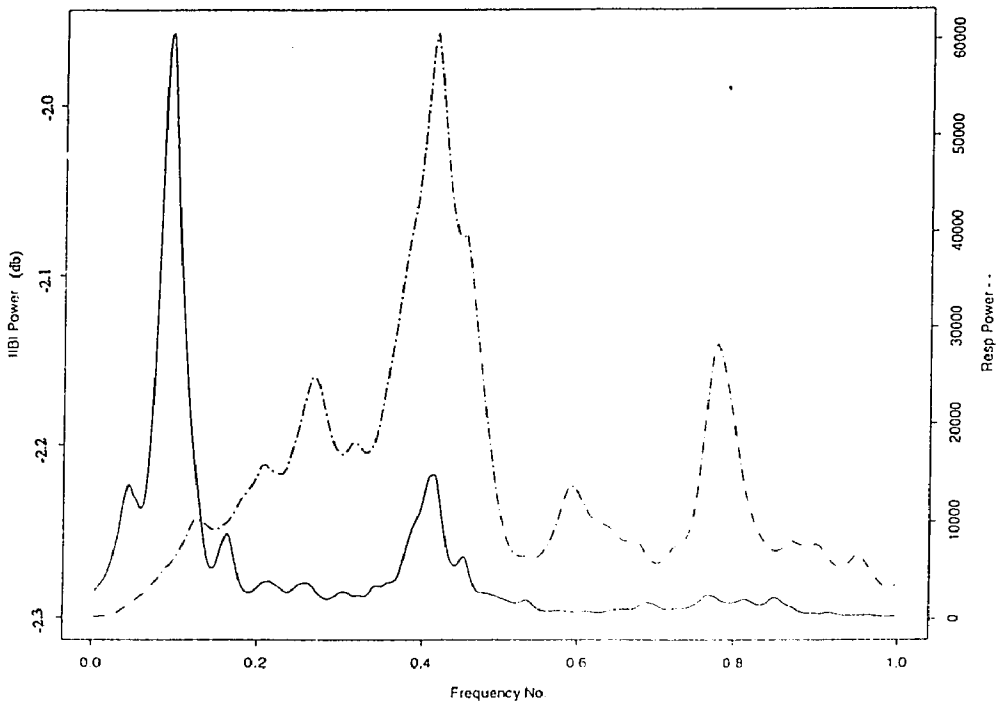

Figure 4.3.1c Spectra of the IBI and respiration signals corresponding to the signals shown in Figure 4.3.1a and Figure 4.3.1b.

the IBI and respiration signals. The solid line represents the power spectrum of the IBI signal while the dotted line represents the power spectrum of respiration. The spectrum of the respiration signal is the reference used to identify the respiration frequency peak in the spectrum of the IBI signal. It is clear that an identifiable peak in the spectrum of the IBI signal corresponds to the peak of the spectrum of the respiration signal at the same frequency. Since this peak is located at the respiration frequency and is a contribution of respiration control, the area under the

peak reflects the intensity of the parasympathetic activity in the control of respiration and is called vagal power in our study.

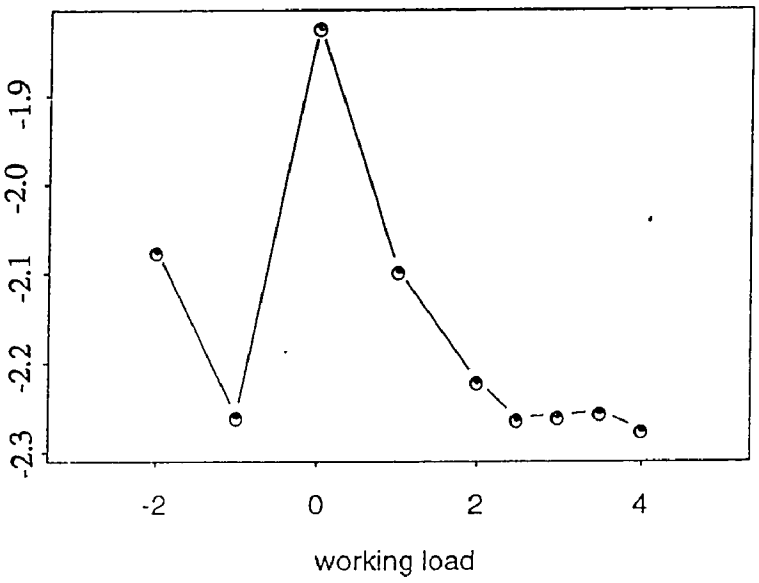

Figure 4.3.2 Vagal powers vs working loads (the unit of the working load is miles/hour). The negative number represents the number of the rest during the exercise.

We have measured the vagal power in different stages (that is, 1MPH, 2MPH, etc). Figure 4.3.2 shows vagal powers at different work loads (or walking speeds) from a normal subject using protocol 2. The x-axis represents the walking speed while the y-axis represents the vagal power. The negative numbers on the x-axis represents the number of rests during the experiment. We have found that vagal power decreases with an increase of the walking speed. The result also implies that vagal control of the heart diminishes if exercise load (walking speed) increases. Further investigation indicated that the trend of vagal power decrease was an exponential-like curve. For an exponential curve, the time constant is an

important factor that determines the characteristics of the curve. Thus it is valuable to study the "time constant" of the vagal-load distribution since it can tell us how rapidly the vagal power decreases to the 36% of the vagal power during rest. The "time constant" can be obtained using the curve-fitting method. It was found that the "time constant" for the normal group was 20% less than in subjects with disease.

Spectrum analysis has been demonstrated in the above applications. The advantage of spectrum analysis is that the intensity or the power of frequency-associated activities can be easily visualized and studied.

CHAPTER 5

RECENT DEVELOPMENT OF PHASE DEPENDENCE STUDY IN HEART RATE VARIABILITY

5.1 Introduction

Heart rate variability studies using conventional time series analysis techniques, such as complex demodulation and spectrum analysis, have demonstrated the applicability and advantages of these techniques. From the amplitude variation of the complex demodulated output, we are able to trace the intensity of the vagal control of the heart as a function of time, especially changes of vagal control due to the change of conditioning. From the amplitude of the Fourier transform using power spectrum analysis, we are able to find the frequency content of heart rate variation and identify the contributions of respiration-associated vagal control of the heart, or vagal power. Since an amplitude at a given frequency in the power spectrum of a signal is an averaged contribution of the given frequency component over the time duration of the signal, the vagal power is an averaged power contributed by the respiration to the heart rate variations. These two time series techniques have provided valuable tools to analyze the heart rate variability in both the time domain and the frequency domain, and their popularity is increasing.

However, a major drawback is that these two techniques fail to show phase-dependence of vagal control on the heart rate. In fact, the timing and intensity of vagal stimulation both play an important role in determining the heart rate. The effect of vagal stimulation on the heart either delays or advances the time

of the heart-beat initiation, depending on the timing of the stimulation.

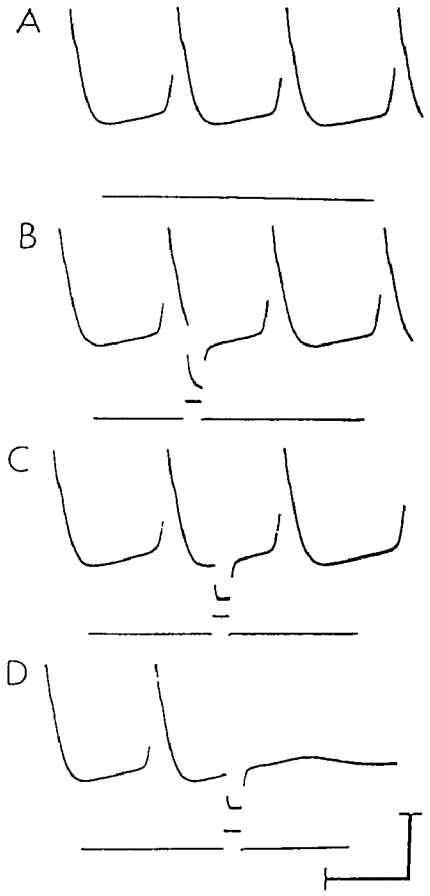

Figure 5.1.1 Suppression of pacemaker activity of an SA node by a brief, hyperpolarizing current pulse. (A) Control cycle with a 640 msec period. (B) A hyperpolarizing pulse applied at an early phase accelerated the next charge. (C) A pulse applied at late phase slightly delayed next charge. (D) A pulse delivered at 67% of the spontaneous cycle terminated the next charge [4].

To illustrate the timing relation between heart rate and stimulation, we present an example as shown in Figure 5.1.1 [4]. Figure 5.1.1 shows the pacemaker activities of a kitten's SA node in response to the stimulation with a brief,

hyperpolarizing current pulse. The peak of the action potential represents the phase marker of the beat. Beneath the action potential curve is the stimulus pulse (no pulse in Figure 5.1.1A). The time of the stimulus pulse following the phase marker of the beat is the phase of the stimulus. Figure 5.1.1B shows that a stimulus applied at an early phase accelerates the discharge of the next action potential (phase advanced). A stimulus applied at a later phase slightly delays the next discharge (phase delayed) as shown in Figure 5.1.1C. Figure 5.1.1D shows that a stimulus applied at a specific phase stopped the spontaneous activity. Therefore change of the heart rate is a phase-resetting process in response to stimulation. A time advance of the heartbeat initiation means an increase of heart rate while a time delay of the heartbeat initiation means an decrease of the heart rate. Study of the timing and intensity relationship between changes of heart rate and vagal stimulation is of great interest to physiologists.

5.2 A Review of Current Research on Phase Dependence

In 1934, Brown and Eccles conducted an experiment to discover an explanation of the vagal action on the heart [5]. In the experiment, single vagal volleys were initiated by applying single induction shocks to the peripheral ends of the transected vagi in a cat. The heart rate was recorded electrically from the pacemaker. It was found that the response of the heart to the single vagal stimulation was a general inhibition or a slowing of the heart rate, but a cardiac acceleration occurred if the vagal volley was set up late in a cardiac cycle. This

discovery suggested the heart rate is dependent upon the phase of the cardiac cycle at which it is stimulated.

To investigate the phase dependence of the heart rate, scientists have approached the response of the heart rate to vagal stimulation with different perspectives and examined the change of cardiac cycle length to vagal stimulation across different phases of cardiac cycles. A phase response curve has been constructed to describe the change of the cardiac cycle length with respect to the phase of stimulation. Jalife and Antzelevitch studied the spontaneous rhythmic activity in isolated cardiac pacemaker cells [4]. Their studies, in which strips of sinoatrial nodes from kittens were used and a current pulse of variable duration was adopted as stimulation, have demonstrated that phase shifts (changes of the cardiac cycle length) occur in response to brief, subthreshold, depolarizing current pulses. The timing relation between cardiac cycle resetting and stimulation was illustrated in Figure 5.1.1 in the section 5.1. The phase response curve was constructed by the phase shift via the phase of the stimulus in order to show different phase resetting behaviors and cessation of spontaneous activity of SA node pacemakers due to the application of perturbing stimuli at different points in the pacemaker cycle. They also provided evidence that there exists a critical time point in a cardiac cycle at which a specific amplitude of stimulus can terminate the spontaneous cardiac rhythm [4]. That is why it is important to apply a defibrillation pulse at the right time to restore the heart to normal sinus rhythm. This evidence is supplementary to proving that timing of stimulation plays an important role on heart rate

variability. Jalife, Slenter, Salata and Michaels also did research on dynamic vagal control of pacemaker activity and suggested that the magnitude of phase shift is a function of the timing, amplitude and duration of the stimulus [10]. This investigation illustrated how many factors usually determine the length of a cardiac cycle or the heart rate. Reiner and Antzelevitch successfully developed a mathematical model to study phase resetting behavior and the annihilation of cardiac rhythmic activity induced by critically timed stimuli [13]. This mathematical modeling helped enhance the understanding of the complex phase resetting mechanism.

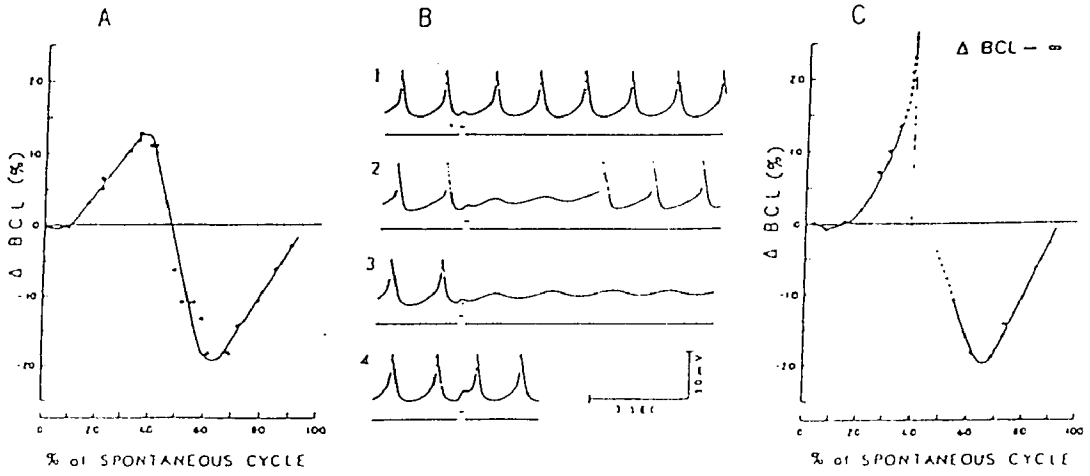

Figure 5.2.1 A. Phase response curve (PRC) obtained from a Purkinje fiber-sucrose gap preparation by scanning the pacemaker cycle with brief subthreshold depolarization current pulses. B. Microelectrode recordings from the same preparation using current pulses of the same duration and amplitude but following a change of the steady state maximum diastolic potential to -60 mV by the application of bias current. C. PRC from a complete scan in the run illustrated in B. The vertical line indicates the phase at which annihilation occurred [13].

Figure 5.2.1 displays a typical result of the above studies in order to depict

phase resetting behaviors during different timing and amplitudes of stimulus. The phase resetting behavior is illustrated by the phase response curve, which was constructed by the change of the basic cycle length (BCL) via phase of the stimulus normalized by the cycle length, represented in percentage of a cycle. Figure 5.2.1A is a phase response curve obtained from a Purkinje fiber pacemaker perturbed by brief subthreshold depolarizing current pulses. Figure 5.2.1C shows a different phase response curve in response to the same duration and magnitude as in Figure 5.2.1A but following a change of the steady state maximum diastolic potential to -60 mv by application of a bias current. The discontinuous portion of the curve in Figure 5.2.1C represents occurrence of the annihilation and the corresponding stimulus phase which could stop the spontaneous pacemaker activity. Figure 5.2.1B shows several cases of the stimulation.

Guevara, Shrier and Glass did some research on the spontaneous rhythm of embryonic chick ventricular heart cell aggregates. They paid particular attention to the phase resetting behavior where transition from delay to advance is a sensitive function of stimulation parameters [7]. Figure 5.2.2 shows a part of their results. They demonstrated that a pulse of stimulus could either delay or advance the time of occurrence of the next action potential, depending on whether the stimulus was delivered early or late in a cardiac cycle. It was found that the phase transition from delay to advance depended on the amplitude of the stimulus. With an increase of stimulus amplitude, the range of phase transition from delay to advance became narrower and narrower, and the smooth phase response curve became discontinuous

in the transition range when stimulus was high. This investigation provided detailed information about phase resetting behavior. Glass, Guevara, Sherier and Perez developed biological models for a cardiac-dysrhythmia-related phase resetting study, and analyzed experimentally observed "chaotic" dynamics at different stimulation parameters [8].

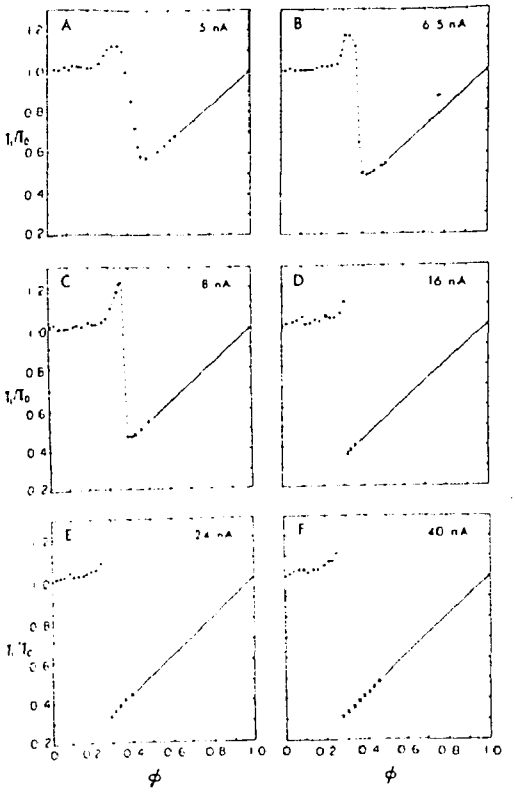

Figure 5.2.2 Data points from phase resetting runs carried out at 6 different stimulus amplitudes in one aggregate. Normalized perturbed cycle length (T_1/T_0) is plotted vs the normalized coupling interval ($\Phi = t_c/T_0$). t_c is the stimulus time after the previous cycle. Crosses are placed midway through stimulus artifact which obscures action potential upstroke. Solid lines are extrapolations based on results obtained in other aggregates and correspond to membrane reaching threshold during stimulus. Data points are found along dashed lines in A-C when phase-resetting run repeated [7].

In summary, phase resetting behaviors are normally illustrated by the phase response curve. The phase response curve is constructed by finding the change of the cardiac cycle length for a given stimulus around the cycle. The stimulus affects

the immediate cardiac cycle during the stimulation and the change of this cycle is usually evaluated in the construction of the phase response curve. The timing of the stimulus determines the phase advance or phase delay. The timing and amplitude of the stimulus determine the amount of the phase shift and possible cessation of the pacemaker activity.

The above work on phase resetting of the cardiac cycle or heart rate is extensive and has provided the basis for further investigation in the area of phase dependence of the heart rate. However, these studies are limited to surgical heart preparations. Phase resetting studies, based on a noninvasive heart preparation, have not as yet been approached.

CHAPTER 6

PHASE DEPENDENCE STUDY

6.1 Experiment

Thirteen presumably healthy volunteers and sixteen persons with chronic fatigue syndrome (CFS) [27] were selected as subjects. At first the subjects were asked to sit and breathe naturally for 2 minutes in order to be stable. Then subjects were asked to pace their breathing at three different rates. The subjects were instructed to inhale-exhale in synchrony with a sequence of lights moving up and down at the desired pacing rate. A light moving up directs subjects to breathe in while a light moving down directs subjects to breathe out. In this way inspiration and expiration each takes approximately half of the respiration cycle so that they have same influence on the heart through the vagus. The three different breathing rates, 8, 12 and 18 breaths/min, were chosen as slow, comfortable and fast pacing rates. The choice of these three pacing rates was intended to examine phase-resetting dependence on the respiration frequency. Each pacing rate was studied in a 2-minute interval since previous work showed that this time length was sufficient to obtain reliable results [27]. The same test sequence --- normal breathing and paced breathing at 8, 12 and 18 breaths/min, was also performed in the standing condition so that effects of posture could be evaluated.

Two standard ECG leads were placed on the subject's chest for monitoring ECG and respiration via impedance pneumography. A 50KHz constant current

signal was applied and the corresponding 50KHz voltage was measured. Changes of the voltage represented variations in chest impedance due to respiration. ECG and respiration signals were collected by a Resp1 Monitor (UFI, Inc. Morrow Bay, CA.) and digitized at 200 Hz using a Metrabyte DASH-16 A/D data acquisition board. The digitized signals were transferred to a Sun workstation for data processing and data analysis. The ECG was used to derive the interbeat interval (IBI) signal. The basic steps have been described in Chapter 1.

6.2 Some Concepts of Phase Dependence

Figure 6.2.1 is an idealized paradigm to illustrate the concept of phase dependence in a self-sustained oscillator that responds to an input. The vertical bars represent some distinguishable phase marker of the oscillator (for example, the positive peaks). In our case, the distinguishable phase marker is the peak of the R wave. When there is no input to the self-sustained oscillator, the same period T_0 will occur repeatedly. When a brief stimulus acts on the oscillator, the phase of the oscillator is reset producing a new period (T_a or T_b). The first half of Figure 6.2.1 shows that the new period becomes greater than T_0 producing a phase delay. Following the phase shift the oscillator continues with period T_0. In the second half of Figure 6.2.1, the stimulus is applied at a different point in the cycle producing a phase advance where the new period is less than T_0. In our application, the input stimulus is the vagus under control of respiration and change in the period corresponds to variation in the interbeat interval.

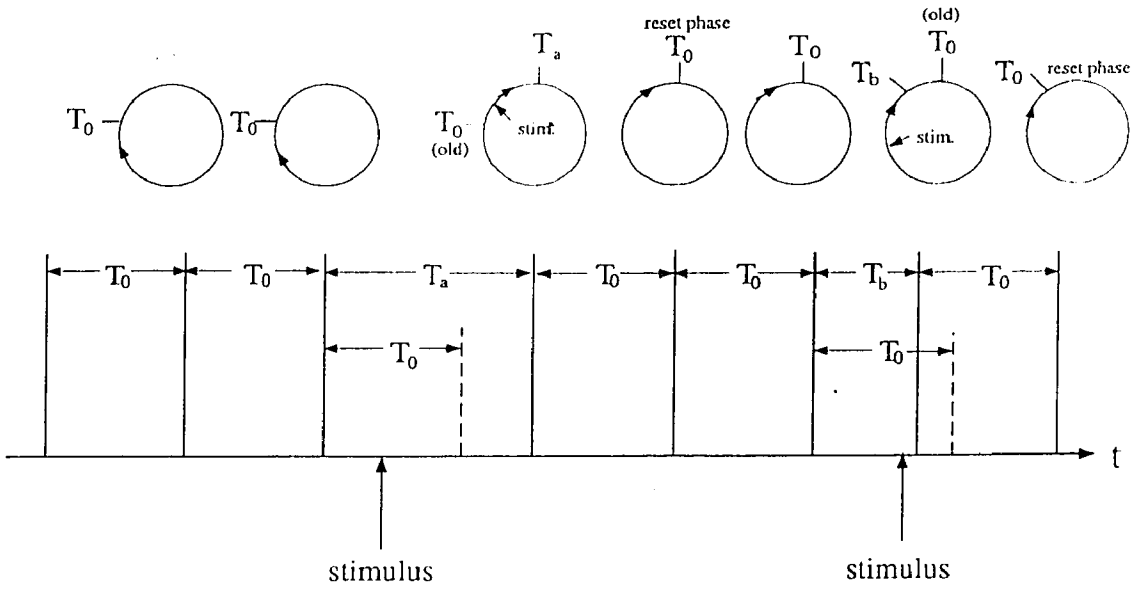

Figure 6.2.1 An idealized phase resetting paradigm. T_0 is the cycle without any perturbation. A stimulus delivered in the 3rd cycle delayed the next cycle ($T_a > T_0$) while a stimulus delivered in 6th cycle advanced the following cycle ($T_b < T_0$).

The circle diagrams in Figure 6.2.1 are another way to illustrate the concept of phase dependence. Each circle represents a cycle. Where there is no stimulus, the period remains at T_0. In the cycle with phase delay or phase advance, the end of the cycle occurs at a time which is greater or smaller than T_0.

6.3 Phase Response Curve

Since either phase advance or phase delay relies on the time of the stimulation, we can describe it as a function of stimulation time. Usually the phase shift is used to represent a phase delay or advance. Phase shift is defined as the normalized difference between the reset period and the period without any perturbation. A phase delay is represented by a positive phase shift while a phase advance is

represented by a negative phase shift. For example, a phase delay in Figure 6.2.1 can be expressed by the positive phase shift $(T_a-T_0)/T_0$ since T_a is greater than T_0 and a phase advance in Figure 6.2.1 can be represented by the negative phase shift $(T_b-T_0)/T_0$ since T_b is less than T_0. The phase response curve is phase shift as a function of the stimulation time.

The phase response curve is a convenient way to illustrate the phasic nature of the response of an oscillatory system to brief perturbations from its surroundings. When a nonlinear oscillator is perturbed by an external stimulus, the perturbation will change the starting point of the subsequent oscillation, inducing either an earlier oscillation cycle or later oscillation cycle. A good quantative description of this phenomenon is to express the difference between the perturbed period and the period without the perturbation (phase shift) as a function of the stimulus time, which is the phase response curve. Thus the phase response curve is a probe for the control mechanism of the oscillation. When two linear oscillators are coupled but operate at different frequencies, the output of the combined oscillatory system contains only terms corresponding to the modes of the oscillation of the individual oscillators. In this case, the phase response curve may not contribute much to this study since the period of the individual oscillator is not perturbed into any new value. However, when oscillators are nonlinear, the coupling can cause the two oscillators to lock onto a common frequency if the frequency difference of the two coupled oscillators is small or one is a submultiple of the other. This suggests that the individual periodic cycle has been perturbed

into a new value and the phase response curve can be used to measure those changes. Specially, for a nonlinear oscillator with spontaneous frequency f_0 perturbed by a periodic external stimulus, as the difference between the natural frequency f_0 (or harmonics) and the stimulus frequency f_s is decreased a point is reached where the system output consists of only a single dominant component at the stimulus frequency f_s. This phenomenon is called frequency entrainment [46]. The phase response curve can be used to show the entrainment. We will demonstrate it later on in our study.

The phase response curve has been used to describe the timing of circadian rhythms and cardiac pacemaker activity in response to external stimuli. In the circadian study, a phase response curve is a plot of phase shifts as a function of circadian phase of a stimulus. The phase shift is the difference between the reset rhythmic period and its natural period, the stimuli include light, temperature, drugs and chemicals. In this way, circadian resetting can be measured. The cardiac cycle resetting has been discussed in chapter 5. As we know, heart rate changes in response to the effect of the vagal nerves on the pacemaker. In our study, the cardiac pacemaker is treated as an oscillatory system. Respiration is considered as vagal input to the system and heart rate is taken as output of the system. Based on the system we have defined and the concepts illustrated in Figure 6.2.1, we began to derive the phase response curve for our experimental data.

Coupling interval --- a time region to evaluate phase dependence on respiration:

Respiration continuously modulates the vagal input to the cardiac oscillatory system so that we can not observe the individual vagal stimuli to each cardiac cycle. It is therefore impossible to use the idealized phase resetting method illustrated in Figure 6.2.1 without some simplification and quantization of the respiratory stimuli. The effect of the respiratory stimulus on cardiac resetting depends upon the phase of the heartbeat without any perturbation and the phase of the respiration cycle [28]. We divide the respiration signal into blocks (or phases) and define the most effective time region of the respiratory stimuli in each cardiac cycle. We locate the interval of the respiration block where the heartbeat occurs and call this the coupling interval because it is the most clearly marked interval where cardiac and respiratory cycles show their coupling. In each respiration cycle, we maintain that ten equidistant coupling intervals have good resolution to capture the changes in the phase of the heartbeat and show the coupling between cardiac cycle and respiration since the number of beats in a respiration cycle (ratio of heart rate and respiration frequency) is normally no more than 10. The points dividing the coupling intervals are called coupling interval points and are normalized by the respiration period as shown in Figure 6.3.1. The stimulus in our study is the respiration depth at the coupling interval point.

T_0 --- a reference: To study phase changes of the cardiac cycle due to the vagal perturbation, we must find a reference period T_0 without respiration influence so that phase shift, the difference between the period perturbed by respiration and T_0,

can be measured. We hypothesize that if we could stop or remove respiration modulated vagal effects on the heart, we could measure the interbeat interval without respiration influence. Ideally we could obtain T_0 by examining the interbeat interval. However, since our experiment studies intact awake humans with a focus on a noninvasive phase resetting study and the respiration influence can not be removed, T_0 must be estimated by mathematical means and signal analysis.

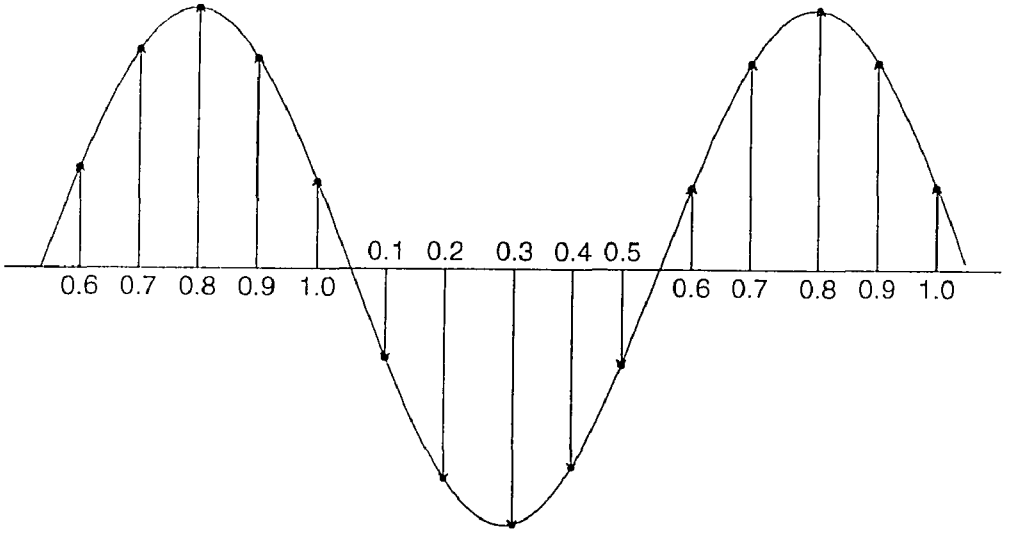

Figure 6.3.1 Coupling intervals marked by coupling interval points. One respiration cycle is shown in the graph.

To estimate T_0, we made the following assumptions: As described previously, the paced-breathing protocol with the instructed breathing can keep the inspiration and expiration well-balanced in a respiration cycle. Since inspiration and expiration can have equivalent vagal regulation on the heart but in the opposite direction, their contributions to the amount of prolongations and abbreviations of the interbeat intervals should be the same. Thus the average of the interbeat

intervals in a respiration cycle represents the reference period T_0 in our study. In fact, T_0 is an approximate value since the propagation of inspiration and expiration signals through the vagus might be slightly different and the control mechanism of inspiration and expiration to the lung might be slightly different. We have found a very low frequency trend in the interbeat interval signal that causes T_0 to be slightly different in different respiration cycles. The cause of this very low frequency trend is unknown. We have named each T_0 as the local T_0 and used the local T_0 as the reference to compute the phase shift, which we are going to derive next.

Phase (T) of the heartbeat in response to respiration --- estimate of a phase given the stimulus at a coupling interval: The human heart is under constant influence of respiration. The interbeat interval reflects both the instantaneous and previous vagal actions on the heart. The evidence provided by Jalife and Glass [4,8] indicates that a single stimulus can change the cardiac period (phase) at the time of the stimulus and the following cardiac periods. The phase of any heartbeat in our paced breathing experiment is due to the integrated effect of the respiration within its coupling interval since the respiratory stimuli within the coupling interval have major impact on the phase resetting of the cardiac oscillatory system. Figure 6.3.2 shows an example to illustrate how the phase of the heartbeat corresponding to a respiration stimulus is estimated. Panel A displays the heartbeats. Panel B is the IBI signal generated as described in chapter 1, which corresponds to the heartbeats in

Panel A. Panel C shows a coupling interval in a respiration cycle with respect to

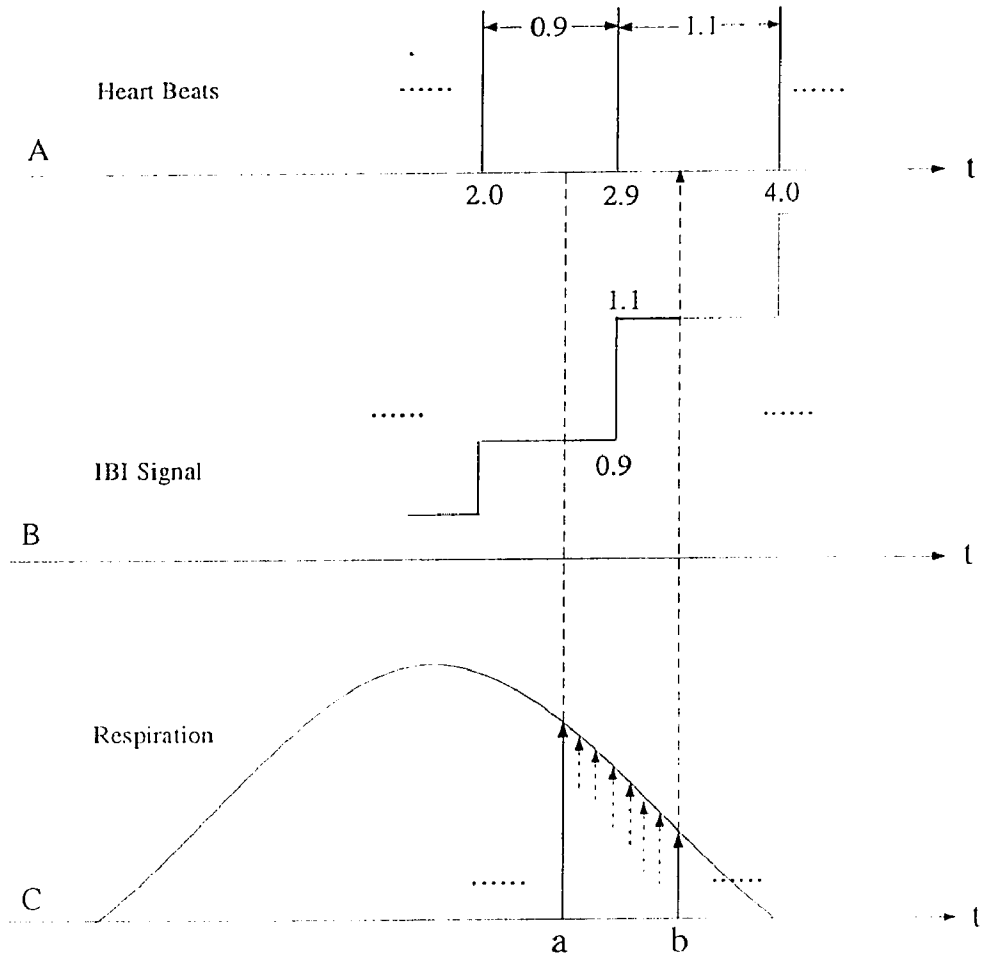

Figure 6.3.2 An example to estimate phase of the heartbeat. A. Heart beats is represented by vertical bars. B. The IBI signal corresponding to the heart beats shown in A. C. A portion of the respiration cycle, in which a and b represent the coupling interval points.

the heartbeats in Panel A. To estimate the phase of the heartbeat given the stimulus at coupling interval point b, we first find the interbeat interval at coupling interval point b from the IBI signal (1.1). Because we are assuming that the interbeat interval of 1.1 is mostly due to the additive effects of all stimuli in the coupling

interval between a and b, we notice that this coupling interval also covers a previous IBI with a value of 0.9, which means that a portion of the stimuli act on the left side of the heartbeat and another portion of the stimuli acts on the right side of the heartbeat. In a coupling interval, action on the left side of the heartbeat means that stimulation is in the late period of a cardiac cycle while action on the right side of the heartbeat means that stimulation is in the early period of a cardiac cycle; they have opposite effects. Therefore averaging the segment of the IBI signal corresponding to the interval between a and b reflects the effect of the stimulation after the cancellation of the opposite effects. The averaging has been done by finding the mean value of the IBI segment in this interval. This averaged value is the estimated phase of the heartbeat, which is a value between 0.9 and 1.1, for example, 1.05.

Phase response curve --- characterizing the phase dependence: Once the phase of the heartbeat is estimated at each coupling interval point, the amount of cardiac cycle resetting can be represented by a phase shift that is the normalized difference between phase (T) and T_0, i.e., $(T-T_0)/T_0$. Therefore characteristics of the phase dependence of the heartbeat on the respiratory stimulation can be revealed by finding phase shifts at different coupling intervals, which is called the phase response curve. The stimulus is represented by the amplitude of respiration at a coupling interval point.

Cardiac cycle resetting in response to respiration generates heart rate

variability and is measured by phase shifts of the heartbeat with respect to respiration stimuli. Study of the heart rate variability is now focused on the examination of this cardiac resetting behavior. Respiration induces the cardiac cycle resetting through the vagal input to the cardiac oscillatory system. The dynamic control process of respiration on the phase of the heartbeat is illustrated in Figure 6.3.3a during sitting and Figure 6.3.3b during standing for a normal subject. In Figure 6.3.3a or Figure 6.3.3b the upper curve shows a running phase response curve estimated by using our method while the lower curve shows the corresponding respiration stimuli at the coupling interval points. A positive value in the running PRC represents a phase delay because the period of the cardiac cycle is prolonged after a stimulus. A negative value in the running PRC represents a phase advance because the period of the cardiac cycle is shortened after a stimulus. Each phase delay and phase advance corresponds to a certain respiration stimulus at a coupling interval point. In this way phase dependence of the heartbeat on the respiration stimulation is clarified. For a running PRC under the slow pacing (8 breathes/min) condition, it is observed that the phase advances to a maximum when the respiration stimulus reaches a maximum, while the phase delays to a maximum when respiration reaches a minimum. This characteristic of the phase resetting is a frequency entrainment phenomenon. Considering the running PRC under slow, intermediate and fast pacing conditions, it is seen that there is a noticeable decrease of the magnitude of the PRC with an increase of the pacing rate (8 $\rightarrow$ 12 $\rightarrow$ 18 BPM). Therefore fast vagal modulation by paced-breathing produces less cardiac

resetting. This study suggests that phase changes of the heartbeat in response to respiratory stimulation is frequency-dependent.

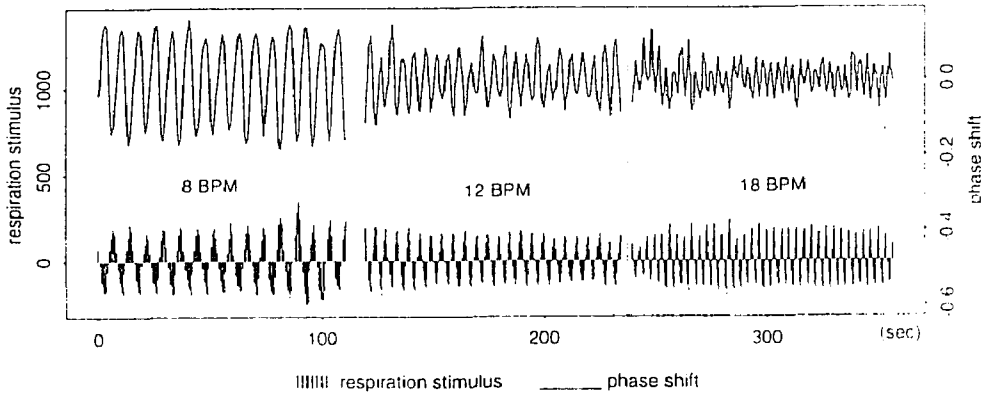

(a)

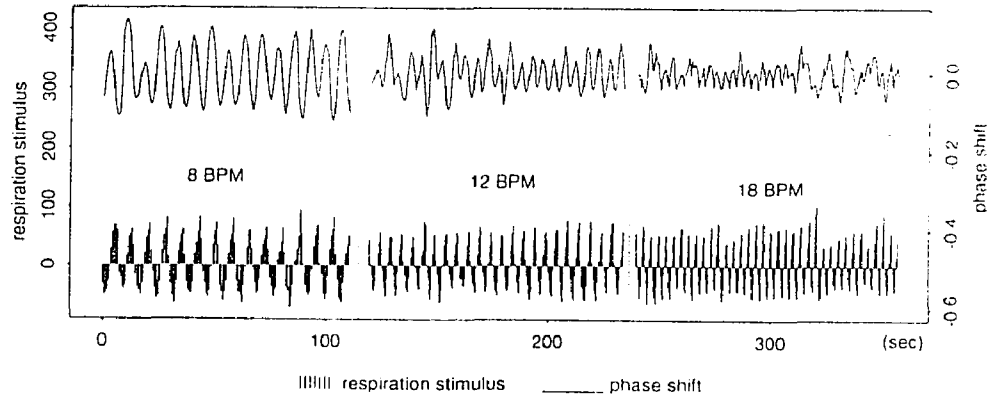

(b)

Figure 6.3.3 The running PRC and respiration stimuli. (a) sitting; (b) standing.

Also, it is observed that the entrainment phenomenon in the sitting state occurs strongly during the slow pacing condition, and occurs weakly during the fast pacing condition. In the standing state where the entrainment phenomenon

decreases with increase of the pacing rate, however, the entrainment was lost at 18 BPM. The degree of the entrainment may be studied by examining the envelope of the PRC, i.e, during the entrainment, the larger the variation of the envelope of the PRC, the lower the degree of the entrainment. The study of the entrainment degree has provided us with a useful way to evaluate the strength of the vagal control of the heart in healthy subjects and subjects in disease. The investigation of the amplitude relationship between phase shifts and respiration stimuli may lead us to better understand how respiration regulates the vagal activity on the heart.

The phase response curves for different pacing rates and in different states have been estimated and illustrated graphically in the above. Analysis of these PRCs plays a very important role for understanding of vagal control mechanisms of respiration on the heart. So far, few analytic techniques have been presented to analyze the PRC and most are focused on the estimation of different PRCs in different situations. Thus investigation of the analytical techniques for the PRC is a part of our research.

6.4 Reexamination of the PRC

Traditionally, most activities are examined on the basis of a one-dimensional straight time line. An example is shown in Figure 6.4.1, which is the usual way to describe a sinusoidal wave with a period of 12 hours. This activity usually needs at least a few cycles (for example, 5 periods) displayed on a straight time line in order to show its periodic characteristics. However, in many respects time does run

in a circle, just as day and night do on a rotating planet. Instead of a straight time line, this sinusoidal activity can also be studied on the basis of a time circle with a period of 12 hours as illustrated in Figure 6.4.2a. The resulting wave is displayed in Figure 6.4.2b. The analysis shows that this oscillatory activity repeats every 12 hours when the time circle of a 12-hour period is adopted. In this way information about this activity is compressed in a 12-hour period. Showing this activity for more than 12 hours will provide no more information.

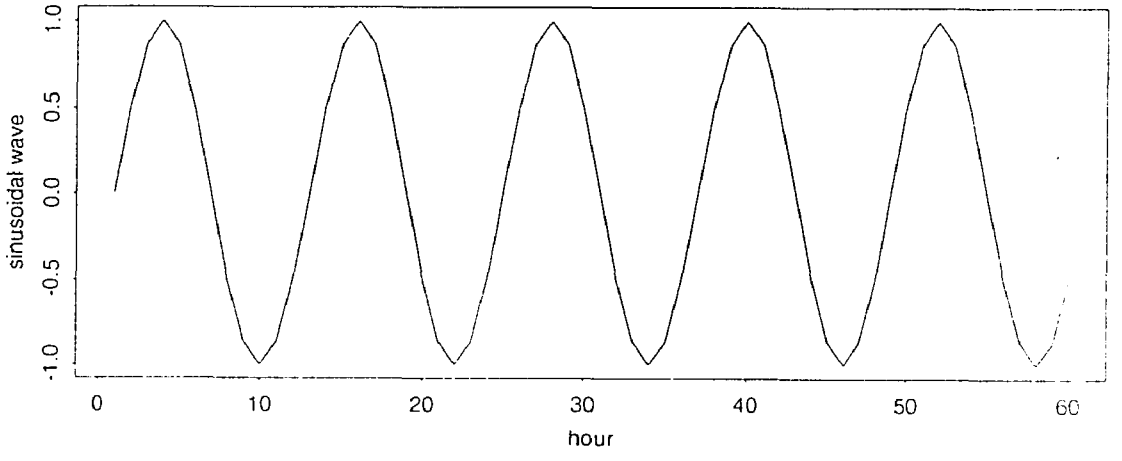

Figure 6.4.1 A sinusoidal wave with a period of 12 hours.

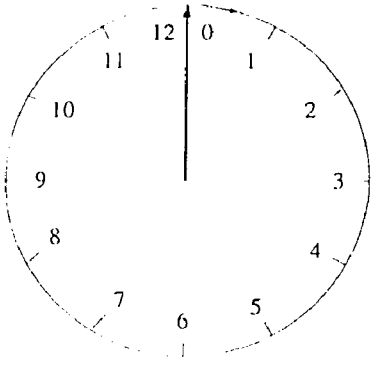

Figure 6.4.2a Time circle with a 12-hour period.

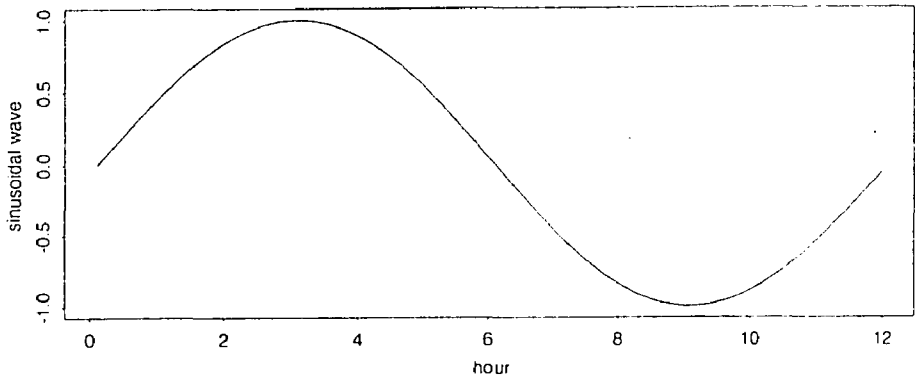

Figure 6.4.2b The compressed sinusoidal wave with a period of 12 hours, which provides the same information as Figure 6.4.1.

However, if an oscillatory activity is different in different periods, the analysis based on the time circle will not only compress the same information (for example, enhance the same repetitive pattern in a signal) in different periods into one period but will also highlight the difference between periods. This idea inspired us to reexamine the running PRC in a time circle since the running PRC exhibits oscillatory properties.

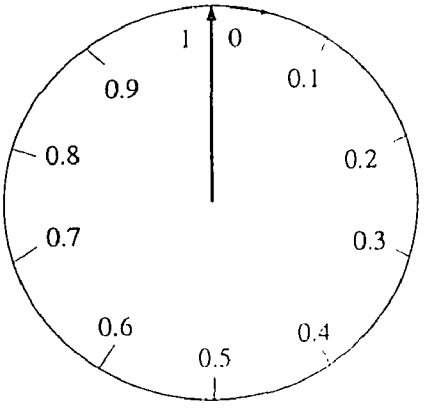

Figure 6.4.3 A time circle with a period of 10 marked by coupling interval points.

In our study the period of the time circle is defined as a respiration cycle

marked by 10 coupling interval points as shown in Figure 6.4.3. Based on this time circle, we have reexamined the running phase response curve in Figure 6.3.3a and Figure 6.3.3b, and the results are shown in Figure 6.4.3a and Figure 6.4.3b.

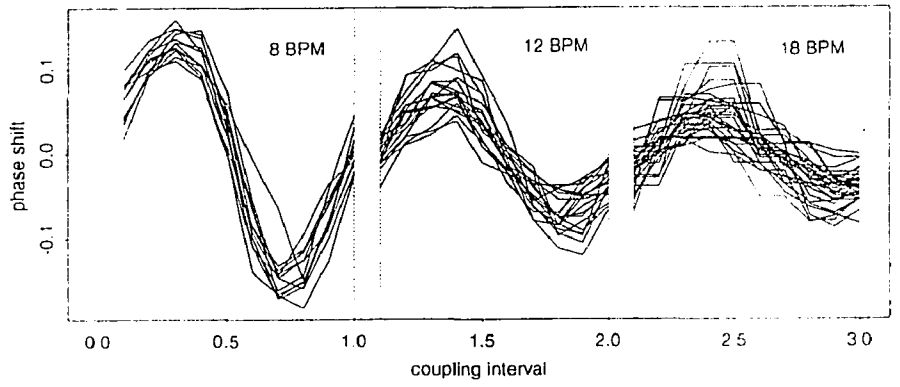

(a)

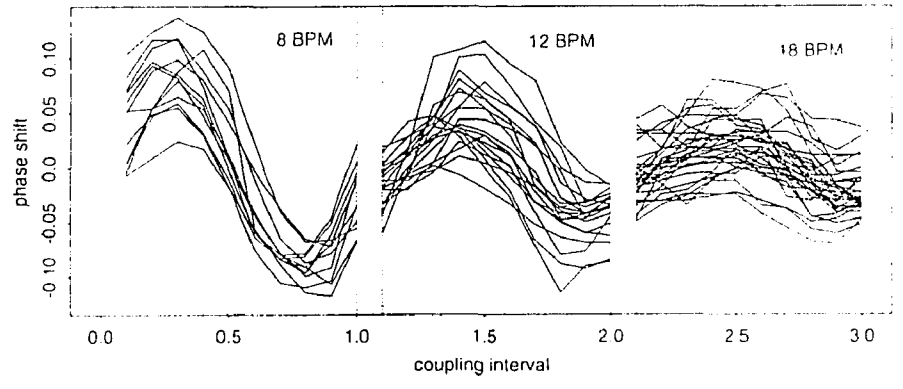

(b)

Figure 6.4.3 PRCs projected into one respiration cycle. (a) sitting; (b) standing.

Further, because of the fluctuation of the heart rate, some coupling intervals in a respiration cycle may not capture a heartbeat. It is therefore helpful to project the PRCs corresponding to different respiration cycles in a cycle in order to resolve

this problem.

This analysis provides us with condensed information about both the common phase resetting behavior shown by the overlapped dark lines and the variation away from the common pattern in different respiration cycles. The illustration offers a way to retrieve a repetitive pattern and to analyze the variation of the PRC in different respiration cycles. The repetitive pattern demonstrates an important characteristic of the phase change of the heartbeat in response to respiration stimulation on the heart. The variation away from the common pattern indicates a decrease of entrainment since respiration stimuli are quite similar in each respiration cycle. We have found that the magnitude of the PRC decreased with increased pacing rate while variation of the PRC increased with increased pacing rate. This feature is an indication of a decrease of entrainment with an increase of the pacing rate.

To retrieve the underlying common pattern in Figure 6.4.3a and Figure 6.4.3b, we have calculated the mean value of the PRC at each coupling interval point. The results are displayed in Figure 6.4.4a and Figure 6.4.4b. The characteristic of the mean PRC is that phase delay occurs mostly during the first half of the coupling interval period, and advance in the second half as illustrated in Figure 6.4.4. The first half of the coupling intervals is the period of late expiration and early inspiration while the second half is the period of late inspiration and early expiration. This illustration gives us a clear picture of how the respiration works as a vagal regulator. As we know, heart rate variability is due to

cardiac cycle resetting. Phase shifts represent the heart rate variability related to respiration stimuli. The mean PRC represents the averaged heart rate variability given stimuli at coupling interval points. In this way phase dependence of the heart rate variability has been demonstrated.

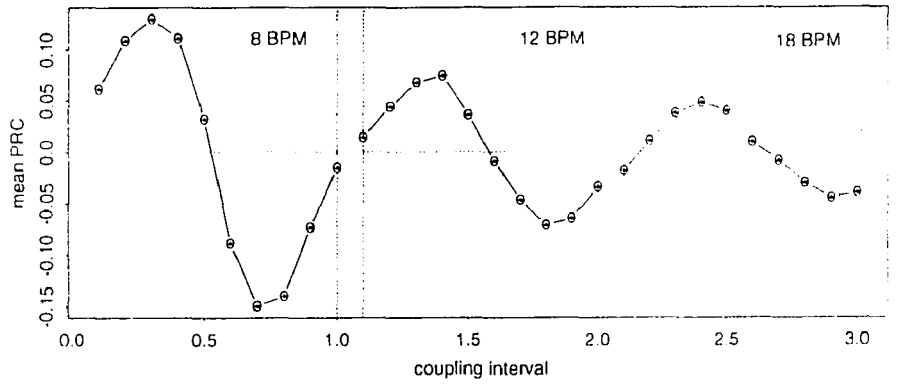

(a)

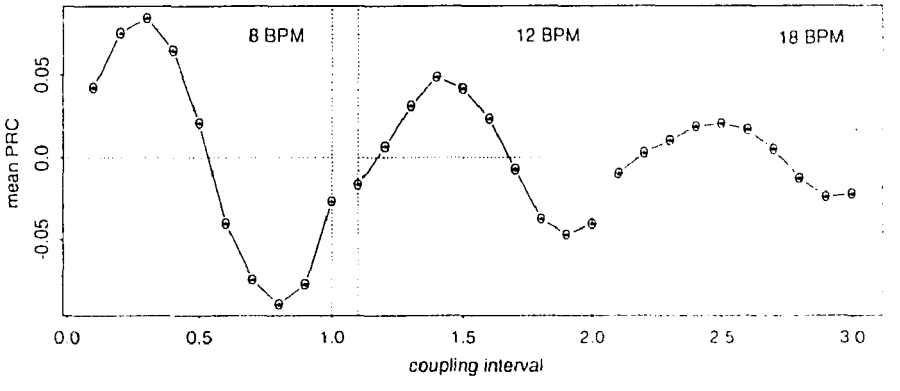

(b)

Figure 6.4.4 The mean PRC at different pacing rates. (a) sitting; (b) standing.

The maximal heart rate variability (MHRV) of the system was measured by finding the difference between maximal delay and maximal advance in the mean PRC. We have calculated the average MHRV for the normal group during both sitting and standing states and the results are shown in table 6.4.1. In the table 6.4.1 it is found that the MHRV decreases about 53% for the sitting state and about 60% for the standing state during the 12 cycles/min breathing rate, and decreases about 79% for the sitting state and 85% for the standing state during the 18 cycles/min breathing rate with respect to the 8 cycles/min breathing rate. The decrease of the MHRV with increase of the pacing rate reflects the reduced vagal control to the heart.

Table 6.4.1 The MHRV at different pacing rates during sitting and standing

	Sitting State	Standing State
8BPM	0.256 (X)	0.191 (Y)
12 BPM	0.120 (47% X)	0.077 (40% Y)
18 BPM	0.054 (21% X)	0.028 (15% Y)

The results presented above have provided much information about effects of vagal actions on the heart through phase resetting and the corresponding respiration stimulus. Because respiration resets the cardiac cycle through the vagus,

investigation of cardiac resetting in response to respiration may provide us some information which leads to an understanding of mechanisms underlying the parasympathetic nervous system and finally the ability to decipher it.

6.5 Comparison between Controls and CFS Subjects

Heart rate variability is due to cardiac cycle resetting in response to stimulation on the heart [1]. The amount of the cardiac resetting is typically not constant, depending on stimulus intensity and phase of the stimulus with respect to a cardiac cycle. Study of cardiac cycle resetting is involved in finding a phase resetting pattern of the cardiac oscillator given a stimulus at different phases of a cardiac cycle. Generally a phase response curve (PRC) is constructed to demonstrate the phase resetting behavior.

Recent experiments by surgical assessment of cardiac resetting have demonstrated that phase resetting studies have provided important clues to understand the mechanism of the vagal-heart system [8,10]. However most investigations are limited to searching for phase resetting patterns under different stimulation conditions. The characteristics of the phase resetting are viewed by examining the consequent phase response curve. We believe that phase resetting study can be further explored and phase resetting methods can be used to investigate certain diseases. Therefore an attempt has been made to characterize the abnormal phase resetting behavior due to chronic fatigue syndrome (CFS) and to compare subjects in disease with normal subjects.

Based on the method we have introduced above, we have constructed the running PRCs for CFS subjects. Typical examples in the normal group and in the CFS group during 8 BPM sitting are illustrated in Figure 6.5.1a for the normal group and Figure 6.5.1b for the CFS group.

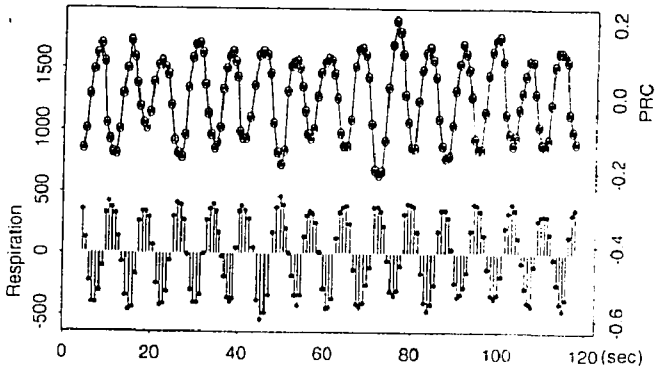

(a)

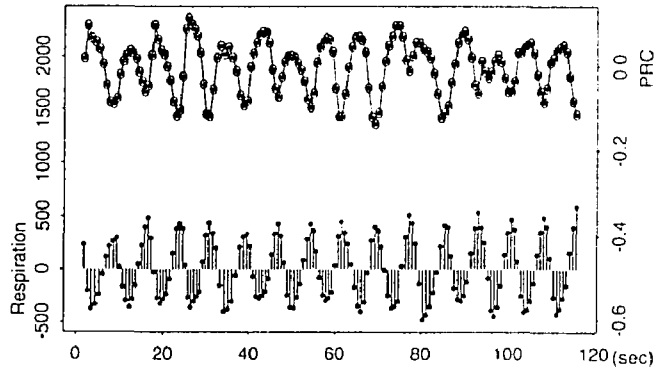

(b)

Figure 6.5.1 The running PRC with respiration stimuli at 8 BPM. (a) normal; (b) CFS.

In each figure, the upper curve is the running phase response curve and the

lower curve shows the respiration stimuli represented by respiration depths. In this way phase shifts (points on the curve) accompanied by their corresponding respiration stimuli (bars) are displayed and the characteristics of the running PRC can be examined. In general, there is a big difference in the running PRC between the normal group and the CFS group. In Figure 6.5.1a phase shifts are strongly entrained by the respiration stimuli. This entrainment phenomenon is easily observed by examining the peak-peak relationship between the running PRC and respiration stimuli, that is, positive peaks of the running PRC is tracing in coincident with the negative peak of respiration and negative peaks of the running PRC in coincident with positive peaks of respiration. However, this relationship is not maintained very well in Figure 6.5.1b. We notice that at around 100 sec, phases were not delayed as expected before starting to advance (negative phase shifts), and at around 80 sec the large stimuli did not induce big phase advances. This phenomenon is an indication of weaker entrainment than the normal subject. Our analysis of the normal and the CFS groups indicates that, although the respiration stimuli in both normal and CFS groups are clearly similar, the amount of phase resetting represented by phase shifts and degree of the entrainment in the CFS group are smaller. This difference may be due to the dynamic control process. In other words, the reduced neural coupling between respiration and the cardiac oscillator through the vagus in the CFS group might explain the subtle difference. We have also projected the PRCs of Figure 6.5.1a and Figure 6.5.1b in different respiration cycles into one cycle using time circle concept as described in section

6.4. The results are shown in Figure 6.5.2a for the normal subject and Figure 6.5.2b for the CFS subject. It is observed that the projected PRCs exhibit the bigger variation in the CFS subject than the normal subject. We will quantify this variation in the later chapters.

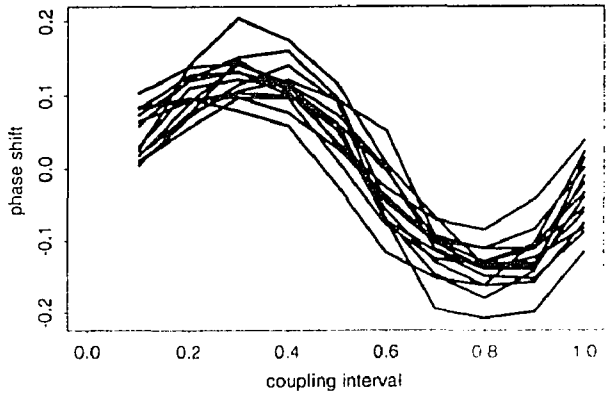

(a)

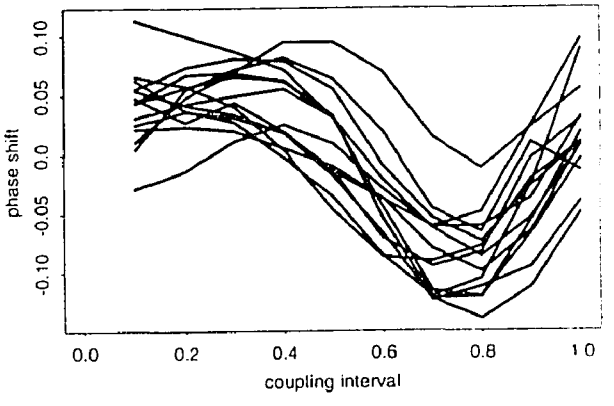

(b)

Figure 6.5.2 PRCs projected into one respiration cycle. (a) normal; (b) CFS.

We first obtained a repetitive pattern by averaging the PRCs of different

respiration cycles at each coupling interval point, which is displayed in Figure 6.5.3a for the normal subject and Figure 6.5.3b for the CFS subject. The resulting PRC is called the mean PRC in our study.

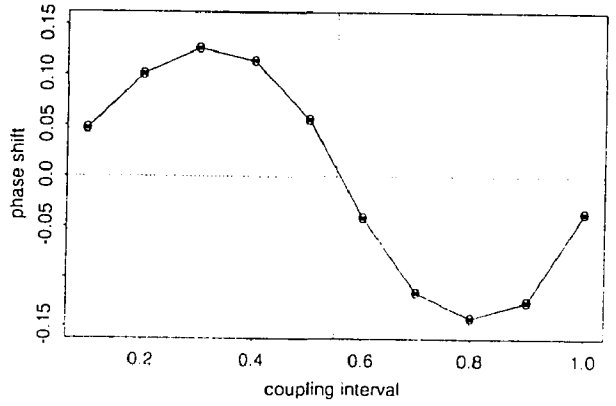

(a)

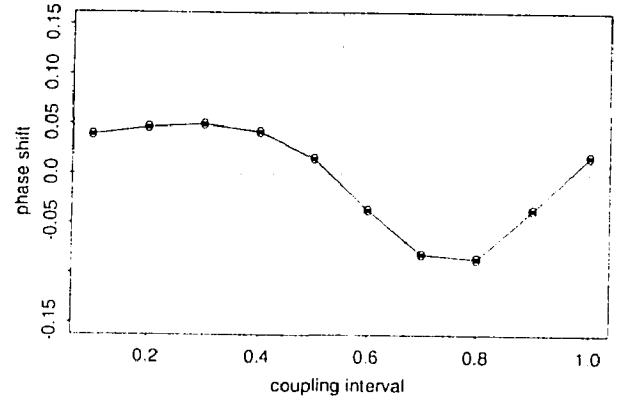

(b)

Figure 6.5.3 The mean PRC. (a) normal; (b) CFS.

Since the range of the mean PRC represents the degree of the phase change (or maximal heart rate variability) in the cardiac oscillatory system, we have

measured these values for both normal and CFS groups in order to compare the CFS group with the normal group statistically.

Table 6.5.1 Comparison between the Normal and CFS groups in MHRV

($p<0.05$)	Normal Sitting	CFS Sitting	Normal Standing	CFS Standing
8 BPM	0.256 (X)	0.133 (52%X)	0.191 Y	0.053 (28%Y)
12 BPM	0.120 (X_1)	0.072 (60%X_1)	0.077 Y_1	0.028 (36%Y_1)
18 BPM	0.054 (X_2)	0.041 (76%X_2)	0.028 Y_2	0.014 (50%Y_2)

Table 6.5.1 shows the average MHRV for two groups during the sitting state and the standing state. We have found that the MHRV for the CFS group is 48% lower during 8 BPM sitting, 40% lower during 12 BPM sitting, 24% lower during 18 BPM sitting, 72% lower during 8 BPM standing, 64% lower during 12 BPM standing and 50% lower during 18 BPM standing. This result indicated that the degree of the phasic change of the cardiac oscillatory system in response to the respiration stimulus in the CFS group was reduced with respect to the normal

group.

We then evaluated the variations of the running PRCs at different pacing rates during both sitting and standing conditions when the PRCs corresponding to different respiration cycles are projected into one cycle. The variation is measured by standard deviation. We found that standard deviations are different in different coupling interval points (the data are in Appendix IV). These absolute standard deviations could not differentiate the CFS group from the normal group because standard deviations of the normal group in some coupling intervals are smaller than the CFS group while in other coupling intervals standard deviations of the normal group are larger than the CFS group. The reason is that normal PRCs have larger range (the difference between the maximal and minimal values) of the mean PRC than the abnormal PRCs and the consequent values of the standard deviation in the normal group may be larger. Therefore we have computed relative standard deviation (RSD), which is the absolute standard deviation divided by the range of the mean PRC, and used this relative value as a measure of the variation of the projected PRCs. The results are demonstrated in Figure 6.5.4. Figure 6.5.4 shows the relative standard deviations in different coupling intervals for both normal and CFS groups, which are computed by averaging the RSDs of all the subjects. It is noticed that the RSDs in the CFS group are larger than the normal group for all the pacing rates either in the sitting state or in the standing state. In this way the variations for the normal group and the CFS group are distinguishable. Figure 6.5.4 also shows that the RSDs for two groups elevate with an increase of the pacing

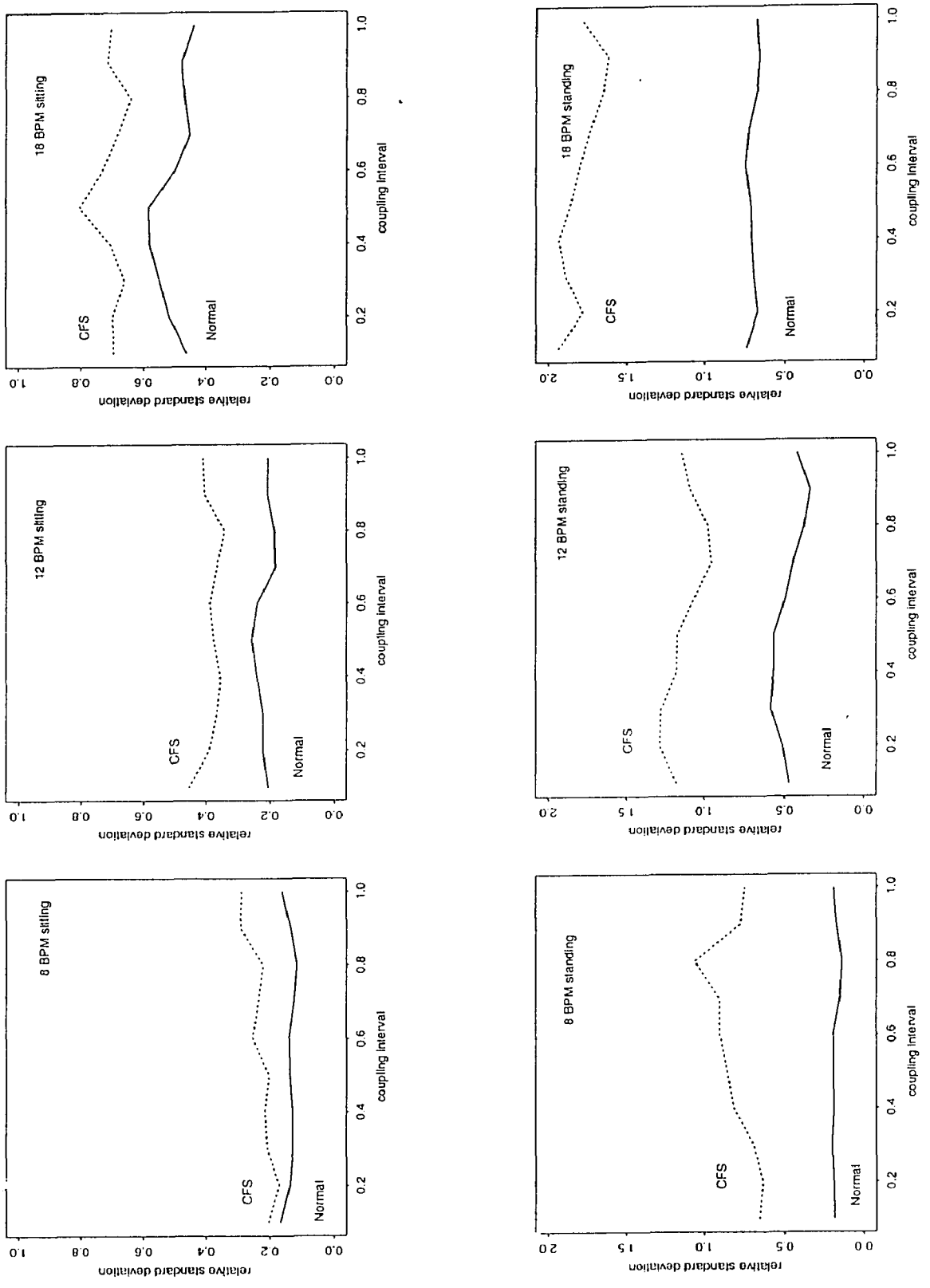

Figure 6.5.4 Relative standard deviation in normal and CFS group

rate, which reflects inversely both the degree of the entrainment between phase shifts and respiration stimuli and the stability of the vagal-heart system.

6.6. Discussion

In this chapter, we have described an investigation into the phase dependence on heart rate variability (HRV) in response to respiration as a vagal input. This investigation offers considerable promise as a noninvasive scheme for phase-resetting experiments in humans. The estimated phase response curve has succeeded in demonstrating the dynamic phase resetting behavior of cardiac cycles given the respiratory stimulus. An important characteristic is that the phase response curve can demonstrate entrainment. We have found that the degree of entrainment decreases with an increase of the pacing rate. Also the amount of phase resetting decreases when the pacing rate increases.

Although respiration influences the cardiac pacemaker through the vagus in an indirect way, and integrated effects of the continuous respiration control on the cardiac pacemaker is complicated, our study has proved that it is possible to use some noninvasive experimental and mathematical techniques to extract useful information on how the cardiac oscillator reacts to perturbation from the vagus.

Further, we have discussed characteristics of the phase resetting behavior in the normal group and the CFS group by means of the running PRC in the time domain, the projected PRCs based on a time circle and the common PRC pattern. We have also illustrated the difference between normal and abnormal phase

resetting in response to a respiration stimulus quantitatively and qualitatively.

Analysis of the running PRC has indicated that the degree of phase resetting and entrainment depends on the pacing rate, posture (sitting or standing), and function of the vagal-heart system. It has been found that the slower the pacing, the higher the degree of phase resetting and entrainment. The effect of the standing state was to reduce the amount of phase resetting and the degree of entrainment compared over the sitting state. The difference between the normal and the abnormal phase resetting behavior may be due to the difference in degree of functioning of the vagal-heart system in the normal group and the CFS group. The CFS group exhibited a lower phase setting, larger variation and weaker entrainment compared to the normal group.

CHAPTER 7

TOPOLOGICAL STUDY

7.1 Introduction

The study described in chapter 6 has indicated that the running phase response curve displays its oscillatory features during a respiration related vagal stimulation on the heart [1]. Many studies have demonstrated that most oscillatory processes exhibit qualitatively similar properties [4,12]. These properties can be analyzed effectively by using topological techniques. Study of the topological properties of the running PRC may provide us with insights into the dynamics of the vagal-heart system. In our present study we present a topological technique to study the phase resetting characteristics. We also attempt to characterize the abnormal phase resetting behavior due to CFS and to compare these subjects with normal subjects.

The dynamic control process of respiration on the cardiac cycle resetting has been illustrated by the running PRC, in which phase shifts are under control of the respiration stimuli. Although this dynamic control process has been characterized in various ways such as entrainment analysis, time cycle analysis and common pattern analysis, it still presents a challenge to understand in depth and to interpret the mechanism of the vagal-heart system. We will now present a technique to construct the phase plane of the running PRC. The phase plane can help us not only to reveal topological properties of the running PRC, but also to transform a running PRC into a topologically recognizable shape. We can then compare the

derived phase plane with the shapes seen in dynamic systems for which the underlying control process is known.

7.2 Phase Plane

Theoretically, the phase plane of a signal is defined as its first derivative dx/dt (usually called velocity) vs x [46]. In our study, the running PRC has values only at coupling interval points. To construct a phase plane, we first interpolated ten points in each coupling interval using cubic splines so that we have the reasonable number of points to do numerical differentiation. The reason we chose the cubic spline method is that the interpolated running PRC will then have continuous first and second derivatives, which is essential in order to construct a phase plane of the numerical data with smooth trajectories. The constructed phase planes of the running PRCs for a normal subject and a CFS subject during the 8 BPM sitting condition are illustrated in Figure 7.2.1a and Figure 7.2.1b. Figure 7.2.1a is a typical example of a normal phase plane. Each point on the trajectory represents a phase shift and its velocity (called phase velocity in our study). The phase velocity represents how rapidly the phase shift changes and in what direction it is going to change. A positive phase velocity indicates an increase of phase shift in the following heartbeat while a negative phase velocity indicates a decrease of phase shift in the following heartbeat. Therefore the phase plane provides us with a dynamic map showing current phase shift, on-going change and direction of the change.

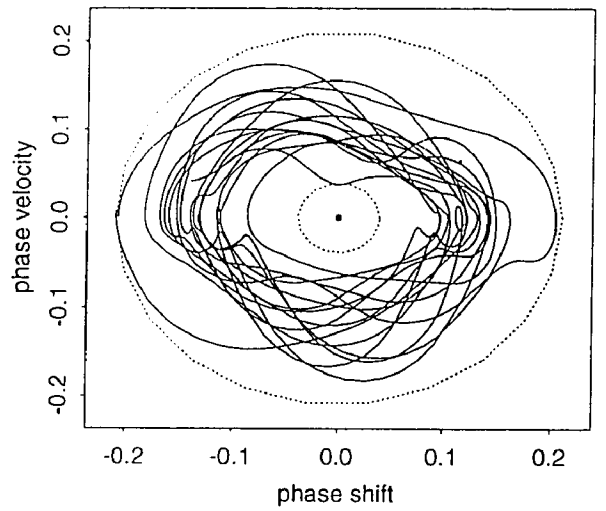

(a)

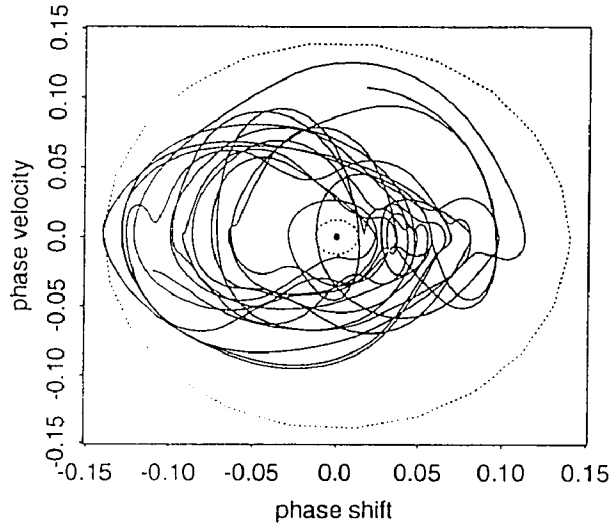

(b)

Figure 7.2.1 Phase planes during 8 BPM sitting. Dotted circles are the inner and outer layers. (a) normal; (b) CFS.

Study of the phase plane reveals topological properties and provides qualitative analysis of the dynamic behavior of the running PRC. In our study, one

orbit is defined as a closed trajectory. If all the orbits fall into one orbit, this orbit is called a limit cycle. In Figure 7.2.1a, we can imagine that initially, the orbit may be on the limit cycle, and it moves off the limit cycle and forms a new orbit due to the stimulation, which we call a shifted cycle. Because the shifted cycle moved differently orbit by orbit, a unique phase plane has been formed. It has been observed that each shifted cycle has similar patterns but different positions. Also each shifted cycle corresponds to one respiration cycle, which indicates a single frequency mode of the phase plane and implies entrainment by respiration. The shifted cycle moved around a bounded region and formed an inner boundary and an outer boundary in the phase plane. The center of the phase plane is a point with zero phase shift and zero phase velocity (singular point), in which phase resetting is zero and heart rate variability is zero. The distance between the center and the inner boundary can be a measure of the degree of the phase resetting. The distance between the inner boundary and outer boundary can be a measure of the degree of dispersion. In addition, we found that the normal phase plane is odd-symmetrical with respect to the zero line. Figure 7.2.1b is a representative phase plane for CFS subjects. Clearly there is a noticeable difference between the normal group and the CFS group. We noticed that some shifted cycles exhibited different patterns. The inner boundary is closer to the singular point since the dispersion of the phase plane is very large. Some orbits are near to the singular point. This suggests an unstable dynamic control by respiration on the cardiac cycle resetting.

The phase plane for a normal subject during the 12 BPM sitting condition

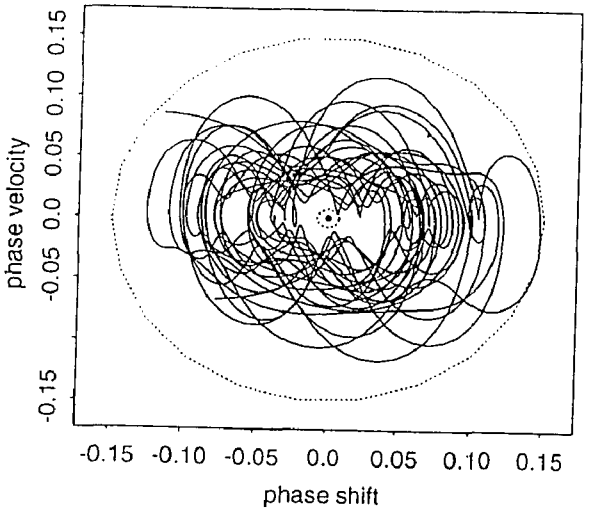

(a)

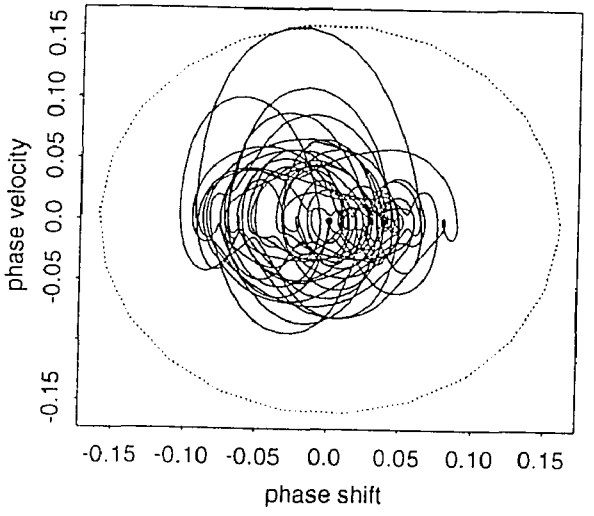

(b)

Figure 7.2.2 Phase planes during 12 BPM sitting. The dotted circles represents the inner and outer layers.

is displayed in Figure 7.2.2a. We have found that the pattern of the trajectories was changed. Compared with the phase plane during 8 BPM sitting, the inward bending of the trajectory was increased. The inner boundary is still clear but smaller.

Although some orbits exhibited different patterns, most orbits follow a similar pattern but at different positions. Figure 7.2.2b is a representative phase plane for the CFS group during 12 BPM sitting. We can see that the shape of the phase plane consisted of many different orbits. Although some common pattern in the orbits was recognizable, the characteristics of the phase plane becomes difficult to be analyzed. The inner boundary of the phase plane could hardly be identified.

The phase planes during 18 BPM sitting are shown in Figure 7.2.3a for a normal subject and Figure 7.2.3b for a CFS subject. We have observed that the phase planes became very complicated. It is very hard to characterize these phase planes and is impossible to distinguish the normal phase plane from the abnormal phase plane. We also examined the phase planes during the standing condition with different pacing rates. We found that posture did not affect the basic topological properties of the phase planes.

In this section, we have discussed characteristics of the phase resetting behavior in the normal group and the CFS group by means of the phase plane. We have also qualitatively illustrated the difference between normal and abnormal phase resetting in response to respiration stimuli. Topological analysis of the running PRC has indicated that the phase plane can reveal the topological properties of the phase resetting behavior and illustrate some mechanisms of the vagal-heart system. We also have demonstrated qualitatively the applicability of the phase plane to distinguish an ordered mechanism from a disordered mechanism. During slow pacing at 8 BPM, phase planes of normal subjects and CFS subjects

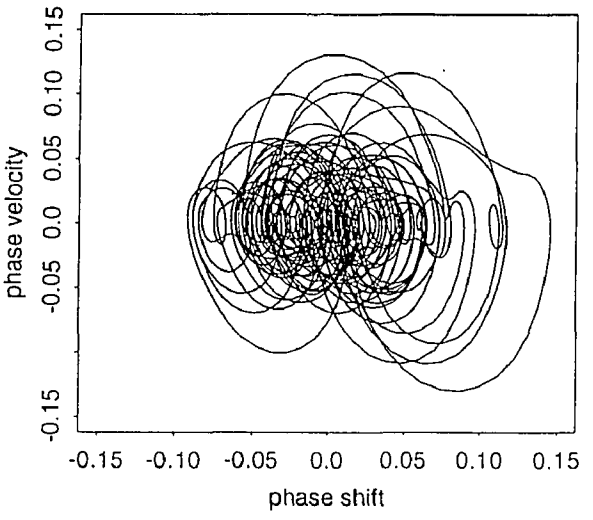

(a)

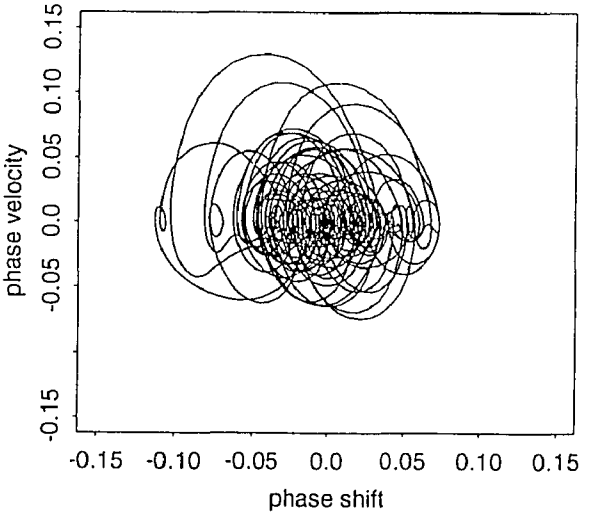

(b)

Figure 7.2.3 Phase planes during 18 BPM sitting. (a) normal; (b) CFS.

are well distinguishable. With an increase of the pacing rate, the distinction between normal and abnormal phase planes decreased and the characteristics of the

phase plane became difficult to be recognized. This suggested that topological techniques are suitable for the slow pacing data. Since we had recognizable phase planes in normal and CFS groups, we started to search for a mathematical model to simulate the dynamic activity in the phase plane and attempt to understand the control mechanism of the cardiac oscillator. The proposed model in our study was the Van Der Pol oscillator, which will be discussed in chapter 9. Therefore, the phase plane can provide us with a recognizable topological shape that we can use to develop a mathematical model that simulates the mechanism of the vagal-heart system.

7.3 Poincare Map

A Poincare map is a geometric analytic approach that was developed by Poincare in the early 1900s. A Poincare map of a signal x(t) is constructed by plotting a signal with a certain delay x(t+a) against the signal x(t) itself [36]. It projects a signal into a 2-dimensional map, in which time is excluded and only the amplitude relationship between adjacent signal points is shown. The Poincare map is used mostly in a qualitative analysis of a system, stressing the global behavior of system dynamics. In our study, the Poincare map is constructed by plotting each phase-shift against the previous one. It can provide information about the relationship of a phase-shift to the next phase-shift. We also constructed a Poincare map to characterize normal and abnormal groups qualitatively.

To illustrate and better understand some features of the Poincare map, we

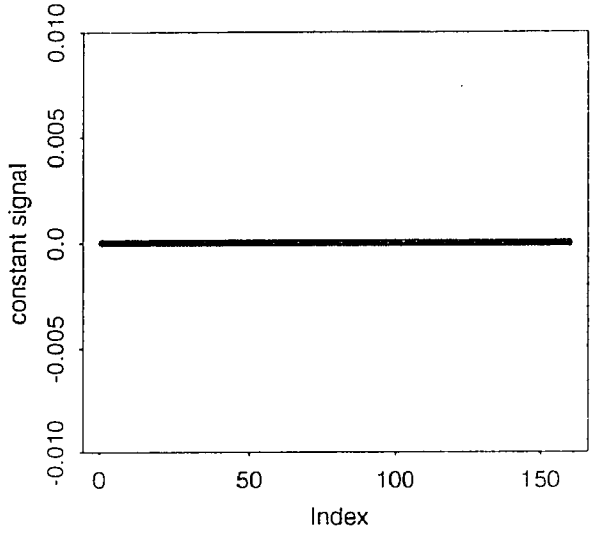

Figure 7.3.1 (a) A constant signal.

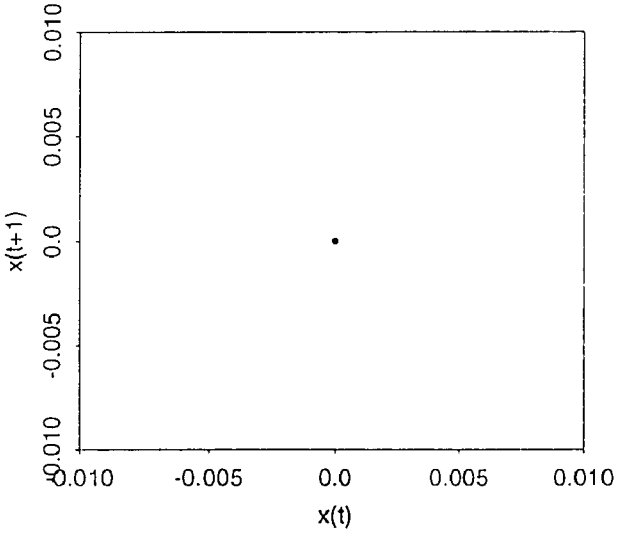

Figure 7.3.1 (b) The Poincare map of a constant signal.

started with simple signals. Figure 7.3.1a displays a signal without any variation, called a constant signal. The Poincare map of the constant signal is a point located at the mean value (zero) of the constant signal as shown in Figure 7.3.1b because neighboring points of the signal have no difference and the overall signal has no variation. This point is called the mean value point.

Figure 7.3.1c is a sinusoidal signal with 160 data points. The Poincare map of the sinusoidal signal is illustrated in Figure 7.3.1d. In Figure 7.3.1d, we can see that many points surround the mean-value point represented by a small circle at (0,0) because the mean value of the sinusoidal signal is zero. These points form a cycle, called the "limit cycle". The difference between neighboring points can be measured by the distance along the vertical axis from the point on the limit cycle to the 45 degree line represented by the solid line in Figure 7.3.1d.

For the sinusoidal signal, the difference between neighboring points decreases with an increase of the absolute value of the data point, forming an elliptic shape. Therefore a Poincare map can demonstrate the trend of changes from one data point to the next neighboring point when the amplitude of the data point changes. Overall variation of the signal away from its mean value can be evaluated by noting that the smallest horizontal and vertical scale of all the data point reflects the smallest variation away from the mean value and the largest scale shows the largest variation from the mean value.

Figure 7.3.1e shows a distorted sinusoidal wave, which is simulated by the sinusoidal wave shown in Figure 7.3.1c with a small amount of white noise added (the noise range, which the difference between the maximal and minimal values, is 12.5% of the range of the signal), and its Poincare map is displayed in Figure 7.3.1f. We observed that there is a large dispersion from the limit cycle and the center of the limit cycle (called the mean value point) has been shifted because the mean value of the signal is no longer zero.

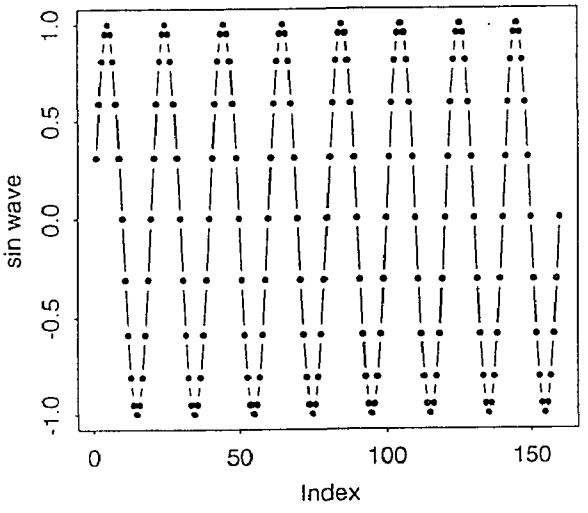

Figure 7.3.1 (c) A sinusoidal wave.

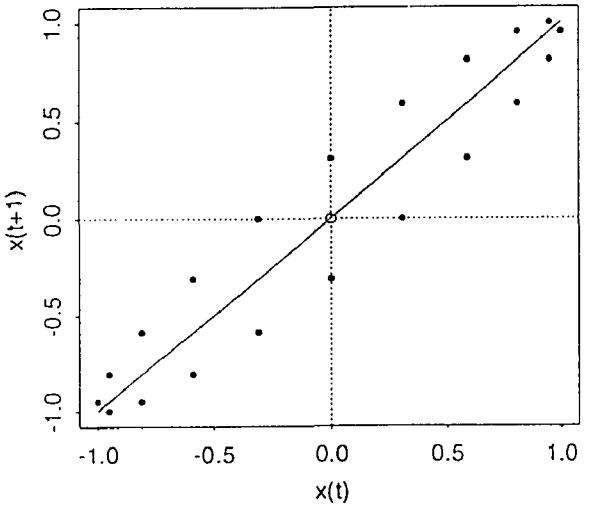

Figure 7.3.1 (d) The Poincare map of a sinusoidal wave.

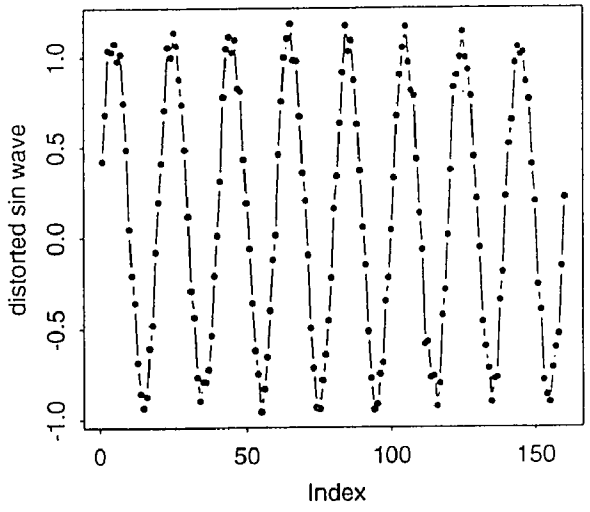

7.3.1 (e) A distorted sinusoidal wave.

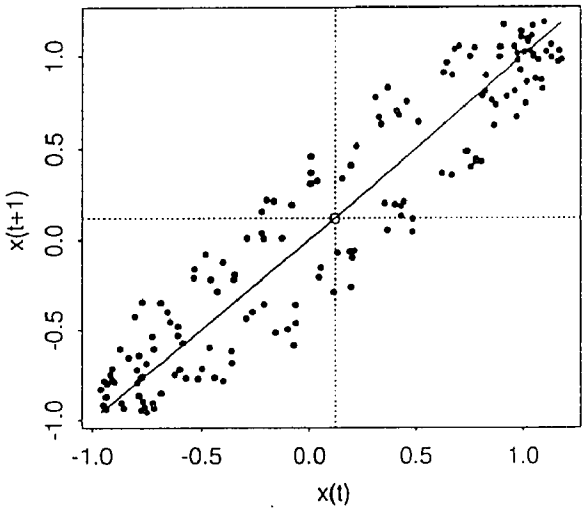

7.3.1 (f) The Poincare map of a distorted sinusoidal wave.

Therefore from a Poincare map we can visualize information about (a) the mean value point, which is the center of the limit cycle or the center of the

Poincare map, (b) variations away from the center, including smallest and largest variation, by examining the scale on the map between center and nearest point or farthest point, (c) trend of changes from a data point to the next neighboring points due to the amplitude change of the data point and (d) dispersion from the limit cycle due to the perturbation. The above study provides us with the basis for the investigation of dynamic phase-to-phase relationship.

Figure 7.3.2a shows a typical Poincare map of the PRC from the normal group at 8 BPM. It is noticed that center of the Poincare map is approximately at (0,0) coordinates, which implies that phase advances (negative phase-shift) and phase delays (positive phase-shift) are well balanced due to the respiration control. We have found that with an increase of the phase shift, the difference between neighboring phase shifts becomes smaller as in the example shown in figure 7.3.1 since the distance from most points along the vertical axis to the 45 degree line decreases. It can be visualized that the points surround the center and form a so-called "strange attractor". A strange attractor represents a perturbed limit cycle with a certain degree of dispersion [36]. The degree of dispersion from the limit cycle can be estimated by measuring the average distance between the inner layer of data points and the outer layer of data points with respect to the center. Figure 7.3.2b displays a typical Poincare map of the CFS group. Comparing to the normal Poincare map, we have found that (a) the center of the Poincare map for the CFS group was shifted by 1.2% of the range of the data since the mean value point was not at (0,0) coordinates, which means that phase advances and phase delays are not

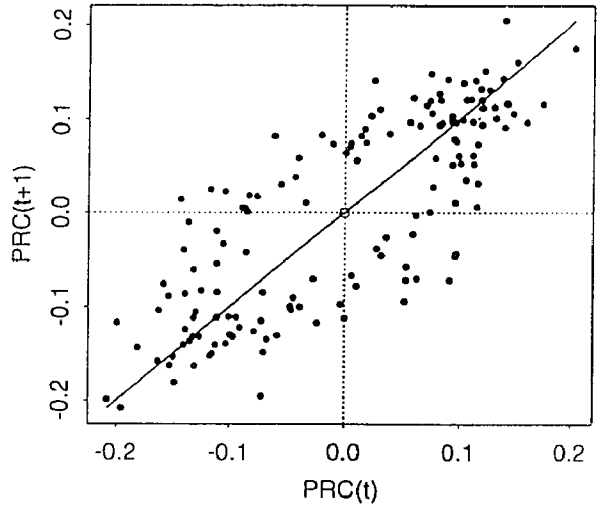

(a)

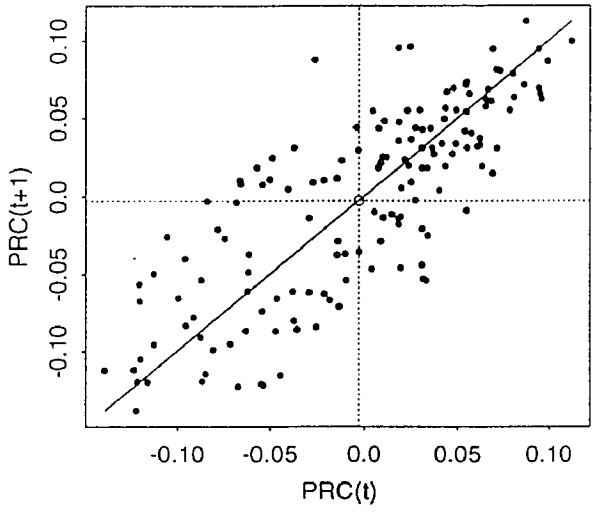

(b)

Figure 7.3.2 Poincare maps of the PRC. (a) normal; (b) CFS.

balanced and do not have equal results in response to the same respiration associated vagal stimulation, (b) variation from the mean value point was smaller, which can be observed by examining the distances between inner layer of the scatter points and the center of the map. In fact, this variation represents the degree

of phase change in response to the respiration stimulus. Therefore, the sensitivity of the cardiac oscillatory system in response to respiration associated vagal stimulation can be illustrated by the average variation of scatter points from the center of the map. The larger the variation, the larger the phase change in response to the respiration stimulus and the more sensitive the system. In addition, the dispersion between the outer layer and the inner can be a factor used to compare CFS subjects with normal subjects. However, the calculation of the variation and dispersion is complicated if we measure the average distance between inner layer and mean value point, and the average distance between the inner layer and the outer layer on the Poincare map. Since the variation and the dispersion reflect nonlinearity of the system and represent nonlinear dynamic activity, estimation of these two variables are valuable. There are a few methods to study this nonlinear dynamic activity, such as fractal dimension and Lyapunov exponents. We have also developed a method to study this activity due to the nonlinearity of the system, which will be discussed in the next chapter.

7.4 3-D Study

As we have mentioned before, topological graphs, such as phase-stimulus relationships, phase planes and Poincare maps, are limited to two variables. Therefore time has to be eliminated in order to examine two additional variables. This leads to either comparing two signals without time or looking at a single signal with time. The 3-dimensional plot can include 3 variables together and

display them in a 3-dimensional space instead of a plane, which provides time-space information about the relationship between heart rate variability and respiration.

The first step in the 3-D analysis is the data mapping from the plane to the space. This mapping can be accomplished in many ways. In our study, we have used the perspective plot to do so. After mapping, we can start to recognize each special pattern and provide some explanations.

In section 7.2, we demonstrated the relationship between the phase shift and the phase velocity (rate of change of phase shift) by the phase plane, which is shown in Figure 7.2.1a. The relationship between these two variables are displayed by sacrificing the time. It is a typical phase plane from the normal group and its structure has been described in section 7.2. Figure 7.2.1a displays the dynamic behavior of the PRC by its trajectories. To include time and display it with time evolution, we have generated a 3-D plot as shown in Figure 7.4.1a, which includes 3 variables, phase shift on x-axis, phase velocity on z-axis and time on y-axis. In this 3-D plot, the specific phase-shift with a phase velocity at each time point has been demonstrated. The trajectories at different times are displayed. It is observed that most trajectories follow the same pattern. Figure 7.4.1b is a 3-D plot of Figure 7.2.1b from the CFS group. It is observed that a major difference between the normal and the CFS 3-D phase planes is that the first few trajectories in time show a transient build-up for the CFS group but not in the normal subject. This tells us that the difference between the normal and the abnormal phase planes are mostly

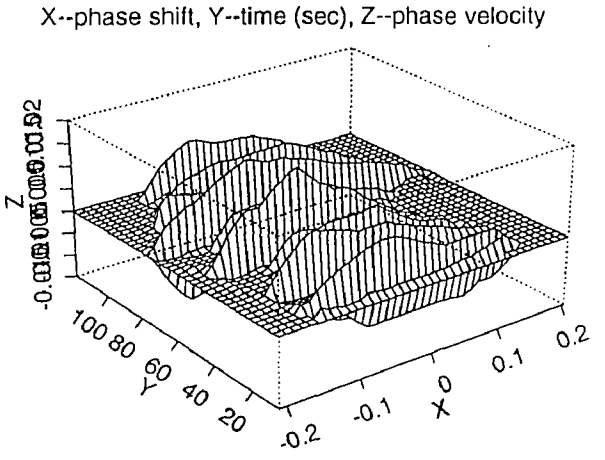

(a)

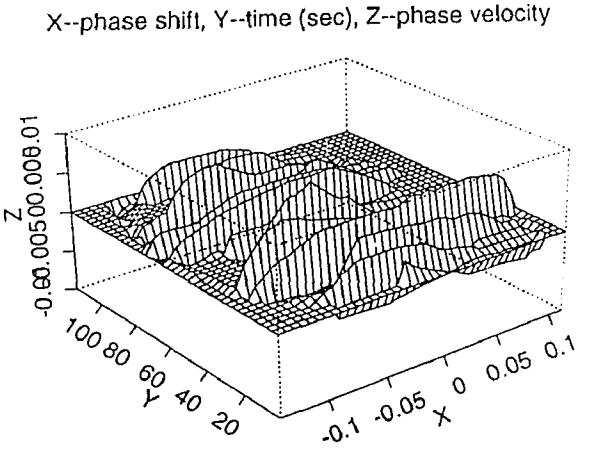

(b)

Figure 7.4.1 A 3-D view of phase planes. (a) normal; (b) CFS.

due to the first several trajectories.

Figure 7.4.2a is a 3-dimensional Poincare map for the normal subject, which

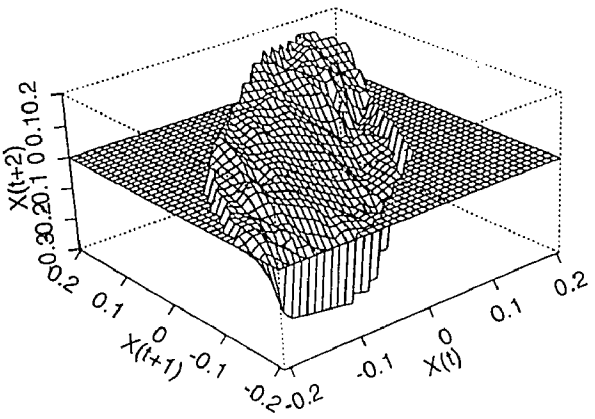

(a)

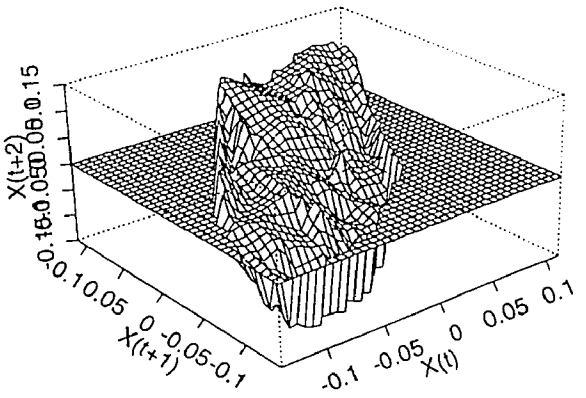

(b)

Figure 7.4.2 Phase spaces of the PRCs. (a) normal; (b) CFS.

is also called a phase space. It is constructed by adding one more variable to the Poincare map shown in Figure 7.3.2a, that is, the 3-D plot consists of the running

PRC with no delay, the PRC with one unit delay and the PRC with two unit delay. This 3-D plot can display the global dynamic behavior of the phase changes. Figure 7.4.2b is a phase space for the CFS subject, which is constructed by adding a variable of the running PRC with 2-unit delay to the Poincare map in Figure 7.3.2b. The difference in shape between the normal and CFS groups is obvious. To study either 2-D or 3-D plots, we think that symmetry of the topology is an important characteristic. It has been observed that many experimental systems possess symmetry. As we have observed before by examining the mean PRC and the phase plane, they have all displayed their symmetry or symmetry-like characteristics. Our study indicates that the preservation of symmetry may be crucial to a stable system. We have found that data from CFS patients such as the mean PRC, phase plane and phase space lost symmetry. The reason may be that the stable neural coupling between heart rate and respiration is not well maintained.

The three dimensional picture is not only capable of providing timing information of the two interesting variables, but also can integrate 3 different variables together to generate a stereo picture. In Chapter 6 we have discussed that a phase-shift depends on both stimulus and coupling interval. To visualize the relationship between these 3 variables, we have generated a 3-D plot shown in Figure 7.4.3, which displays phase-shift as function of coupling interval and respiration stimulus. In this way, we can demonstrate how a phase-shift is related to the respiration and the coupling interval. It is found that a stimulus can cause either a phase advance or a phase delay, depending on the coupling interval.

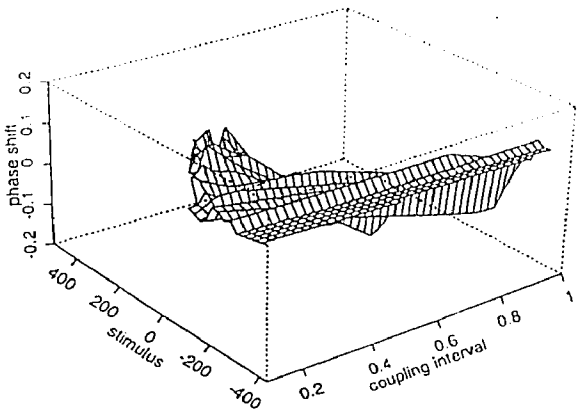

Figure 7.4.3 A 3-D view of the relationship between phase shift, stimulus and coupling interval.

We have presented several 3-D examples to expand our 2-D work. At first we included timing information along with two other variables, so the 3-D plots include time. Then we added one more delayed PRC to study the global dynamic behavior of the PRC in a phase space. Finally we viewed the phase-shift as a function of two variables, stimulus and coupling interval. The purpose is to include as much related information as we can by a 3-D construction. Based on our study, we think that the pattern recognition of a 3-D picture is a first step and an important step to understand the system. At present, our patterning study of a 3-D plot is focused on the recognization of the difference between the normal and the abnormal 3-D plots.

CHAPTER 8

NONLINEAR DYNAMICS STUDY

8.1 Introduction

In Chapter 7, we discussed the variation and dispersion phenomena on the Poincare map. This dispersion reflected nonlinearity of the cardiac oscillatory system coupling with respiration. The system nonlinearity often causes the output of the system to be a so-called "chaotic behavior" [36]. Chaotic behavior appears to be "random" dynamic activity but there is a definite law determining its dynamics. In many studies, researchers only concentrated on the linear output of the system and ignored the chaotic activity caused by nonlinear outputs. In our study, we examined the linear output of the cardiac oscillatory system in response to respiration by finding the mean PRC. The dispersion away from the limit cycle on the Poincare map represents the variation of the PRCs in different respiration cycles from the mean PRC and is due to the system nonlinearity. Complexity is a very important factor of a system and plays a crucial role in determining the nonlinear dynamic behavior of the output of a system. Recently, the study of the complexity of a system has become of great interest to scientists mainly because recent development of nonlinear dynamic theories allows scientists to quantify the degree of a system nonlinearity [23,37-39]. Many studies focused on complex mathematical formulas such as correlation dimension [37]. Few studies have dealt with the probability associated dimension (so-called information dimension),

because there is not a well-developed method to calculate the probability of a system behavior and to construct a proper probability density curve for information entropy and dimension calculation. We have investigated various dimension calculations and found that information dimension is a simple and easily-understood way to characterize complexity of a system as long as we have a good approach to construct the probability density curve.

Here we present a method to calculate the information entropy and dimension of the phase response curve (PRC) in response to respiration stimulation [23]. We have also used this method to analyze the complexity of the vagal-heart system for normal and abnormal situations.

8.2 Probability Density Curve (PDC)

The probability of an event is defined as the ratio of its favorable outcomes to the total number of outcomes provided that all outcomes are equally likely. In the applications of the theory of probability, the probability of an event gives us a certain degree of confidence that the event will occur [34]. In our study, the probability is the frequency of the phase shift located at a certain range of the running PRC. We use an example shown in Figure 8.2.1 to illustrate our procedure of probability calculation.

In Figure 8.2.1, dots are the discrete points on the running PRC. We have a total of 150 points representing each phase change of the cardiac oscillatory system due to respiration. We have categorized these points in different boxes,

where each box represents a range of phase shifts. Since different ranges of phase shift reflect different degrees of phase changes of the cardiac oscillator in response to respiration stimulation, computing the number of phase shifts favorable to each range will provide us with quantitative information of cardiac oscillatory system behavior. For example, if all the points have the same value, which means the system has the same response to each input no matter how different the inputs, no information on the system would be provided. In information theory, this is considered as the output of the system containing only redundant repeats and with zero information. If all the points are different, which means the system has a different response to each input whether the inputs are the same or different, it would provide us with the largest uncertainty of the system, and hence, maximal information.

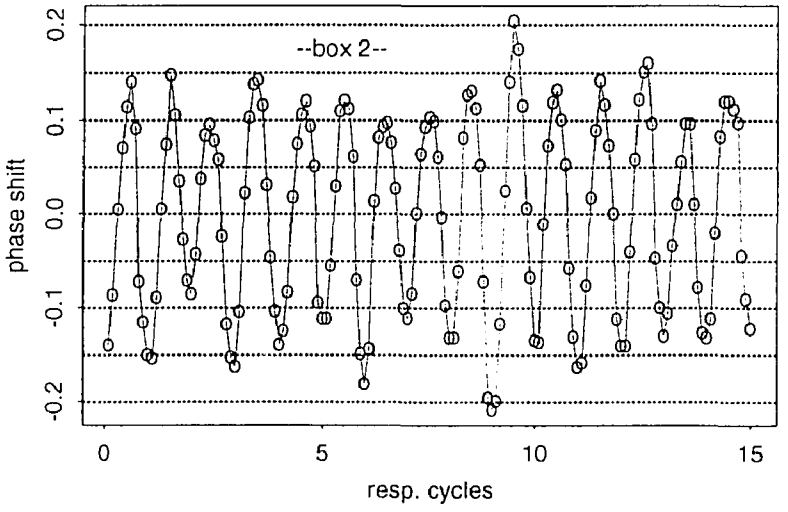

Figure 8.2.1 Phase response curve divided by boxes.

To calculate the information on the basis of information theory, we must find the probability of the different system outputs. For the output shown in Figure

8.2.1, each box will be used to categorize the different system outputs. The probability at a box equals the number of points in the box divided by the total points (150 points), which reflects the degree of the system output favorable to that range of the phase shift covered by the box. For example, the probability of box 2 equals 2/150, or 0.0133. The higher the probability of the box, the more likely the system output is in the box. The probability density curve (PDC) was constructed by finding the probability of each box at the corresponding range of phase shifts, which is shown in Figure 8.2.2.

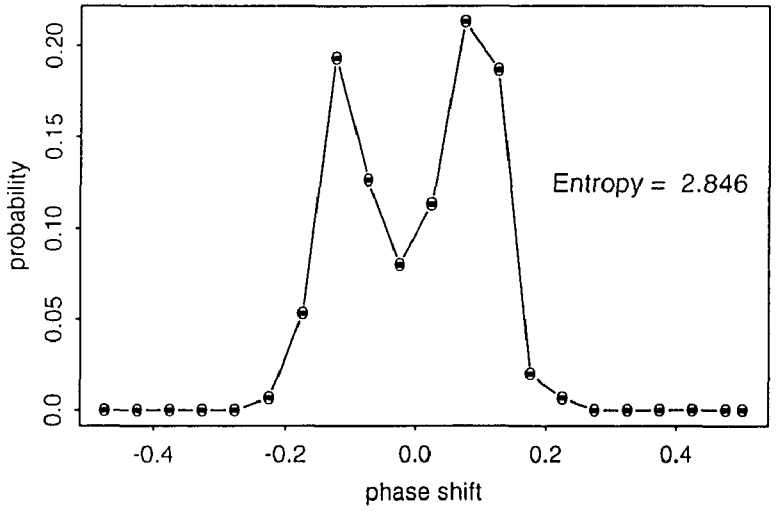

Figure 8.2.2 Probability density curve.

The probability of each box can also be interpreted as a measure of the system preference. If the probability of a box were very large like 0.999, it would be almost certain that the system would respond in the range of the box; if the probability of a box were very small like 0.001, it would be reasonably certain that the system's response would be highly unlikely in the range of the box.

In Figure 8.2.2, we can see a distribution of the system preference for different ranges of phase shifts. The peaks in the probability density curve reflect the most frequent visitation of the phase shift while those probabilities with very low values indicate the unlikeness of phase shifts in those corresponding ranges. It is noticed that large phase shifts have lower probabilities and phase shifts around 0.1 or -0.1 have maximum probabilities.

8.3 Information Entropy and Dimension

In information theory, the uncertainty of a system event is normally measured by the following formula:

$$A=P_a \log_2 P_a \qquad (8.3.1)$$

where P_a is the probability of the event and A represents the uncertainty of the event. The summation of uncertainties of all events represents the degree of uncertainty of a system. Since we have derived the probability density curve, we can measure the uncertainty of the cardiac oscillatory system during respiration stimulation. This measure is called information entropy. It is calculated by the following formula [6]:

$$H=-\sum (P_i \times \log_2 P_i) \qquad i=1,2,3,\ldots,n. \qquad (8.3.2)$$

where P_i is the probability of the ith box, n is total number of boxes, and $\sum P_i=1$.

The entropy of the PRC shown in Figure 8.2.2 is 2.846 bits. The entropy, as a measure of uncertainty of the system, would be the greatest when all boxes have equal probabilities.

We have noticed that information entropy we calculated above is a value related to the box size of 0.05 as shown in Figure 8.2.1. This suggests that information entropy depends on the box size we choose. Different entropies have been obtained using different box sizes as shown in Figure 8.3.3.

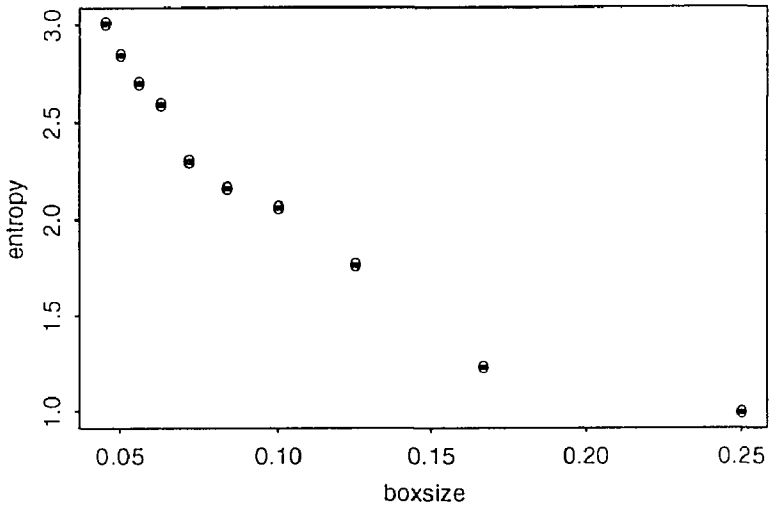

Figure 8.3.1 The relation between entropy and box size.

It is observed that entropy declines with an increase of the box size. This can be explained by the fact that specifying a large box will include more points in the box, which means that more phase shifts belong to the same category, so the degree of uncertainty will decrease. Information entropy provides us with

quantative information about the predictability of the system behavior. A system with large entropy demonstrates low predictability or high uncertainty. However, entropy of the system depends on how we choose a measure and what scale the measure is. Therefore, information dimension is introduced. Information dimension utilizes information entropies of a system in different measures and is independent of the scale of the measurement (for example, the box size in our study). It is a measure of complexity of a system [36]. Equation 8.3.3 gives the information dimension.

$$H=K\left(\frac{1}{E}\right)^{D} \qquad (8.3.3)$$

where H is information entropy, D is information dimension, E is box size, and K is a scaling factor. The above equation may be rewritten as:

$$\log(H)=D\log\left(\frac{1}{E}\right)+\log(K) \qquad (8.3.4)$$

Therefore, if we have a plot of log(entropy) vs log(1/boxsize), the slope of this plot will be the information dimension. It is clear that information dimension is independent of the box size. Figure 8.3.4 is a plot of log(entropy) vs log(1/boxsize), in which information dimension is calculated by finding the slope using a least-square-fit method. The information dimension in Figure 8.2.1 equals 0.652.

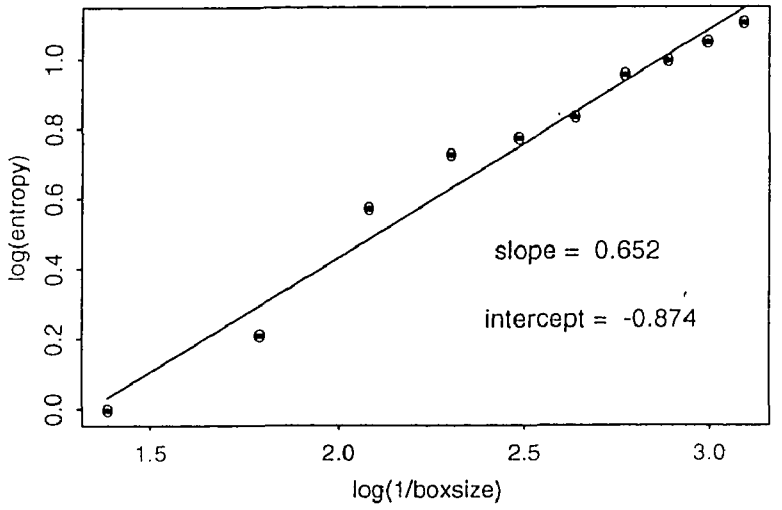

Figure 8.3.2 Calculation of the information dimension.

8.4 Comparison between Controls and CFS subjects

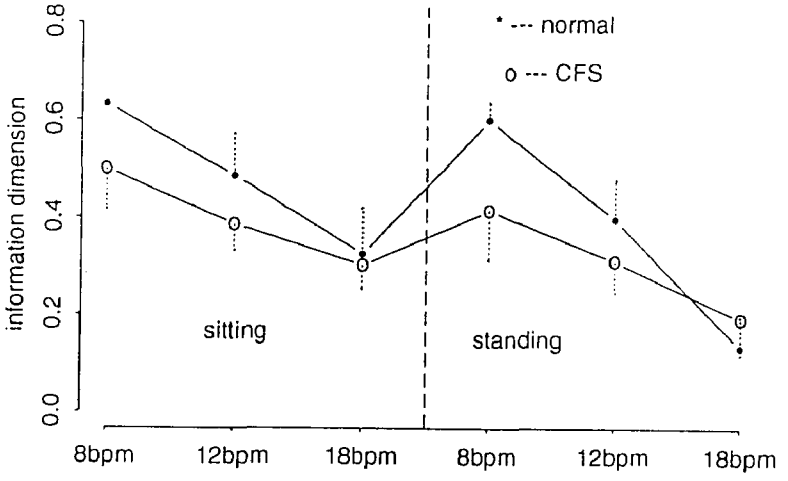

Figure 8.4.1 Information dimensions for the normal and the CFS groups.

We have used the method in section 8.2 and section 8.3 to calculate information dimensions in the normal group and the CFS group. The results are shown in Figure 8.4.1 for the control group and the CFS group.

The analysis shows that information dimensions in the CFS group are generally lower than the control group except in the case of 18 BPM standing. The largest difference of the information dimension between the two groups has been found in the slow pacing condition (8 BPM sitting and standing). The information dimension in the CFS group is 21% lower during 8 BPM sitting and 31% lower during 8 BPM standing than the control group.

Table 8.4.1 Comparison between the Normal and CFS Groups in Information Dimension

	Normal Sitting	CFS Sitting	Normal Standing	CFS Standing
8 BPM	0.632 (x)	0.499 (y)	0.60 (X)	0.414 (Y)
12 BPM	0.486 (77%x)	0.386 (77%y)	0.398 (66%X)	0.311 (75%Y)
18 BPM	0.325 (51%x)	0.302 (61%y)	0.134 (23%X)	0.192 (46%Y)

We noticed from the table 8.4.1 that information dimension decreases with an increase of the pacing rate. In the normal group, the decrease of the information

dimension was from 23% during 12 BPM sitting to 49% during 18 BPM sitting with respect to 8 BPM sitting, and from 34% during 12 BPM standing to 77% during 18 BPM standing with respect to 8 BPM standing. This suggested that information dimension decreased faster during the standing condition than the sitting condition. Similar results have been obtained from the CFS group. In the CFS group, the decrease of the information dimension was from 23% during 12 BPM sitting to 39% during 18 BPM sitting with respect to 8 BPM sitting, and from 25% during 12 BPM standing to 54% during 18 BPM standing with respect to 8 BPM standing. Comparing to the normal group, we can see that in the CFS group the rate of decrease with an increase of the pacing rate was smaller. This may suggest that system sensitivity and controllability in the CFS group may be lower than in the normal group.

8.5 Discussion

We have presented a new approach to construct the probability density curve (PDC) of a running PRC, in which the PRC reflects directly heart rate fluctuations by phase shifts during the different vagal stimuli (paced breathing in our study). We have found that the width of the PDC usually reflects the range of heart rate variations and the peaks of the PDC corresponds to most favorable states of the phase shifts. A narrow PDC with high peaks implies less heart rate variability and has been found in the CFS group, while the wide and flat PDC implies high heart rate variability and has been found in the normal group. Based on the PDC, we

have calculated information entropy. Information entropy reflects the system preference to certain state of the phase shifts and represents the amount of information needed to specify the state of phase shifts or the state of the heart rate variability to an accuracy of the boxsize. Our study has indicated that large information entropy has usually been obtained in the normal group with a large heart rate variability, which suggested there was a lesser chance to produce identical heart rates in response to different stimulations (less predictability of the system). The entropy obtained from the CFS group was generally small. A similar result was obtained from the calculation of information dimension, which has been derived from information entropies of the different box sizes. Information dimension is an index of the complexity of a system that generated the data. A low dimension means that less states are needed to describe the system while a large dimension means more states are required to describe the system. We have found that the system complexity depends on the stimulation frequency and decreases with an increase of the pacing rate. A lower dimension occurred in the CFS group except during the condition of 18 BPM standing.

The calculation of information entropy and dimension provides an attractive and useful tool to examine aspects of heart rate variability. Future investigation of the reasons which caused the CFS group to have low information dimension may be valuable.

CHAPTER 9

MODELING AND SIMULATION

9.1 Introduction

System modeling becomes necessary when whole or part of the internal structure of the system is not clear. System modeling serves either to develop or to search for well-defined mathematical equations that can simulate the system behavior. There are several advantages to system modeling, including (a) better comprehension of a system, (b) further simplification of a complicated system because many real and complex systems can be simplified into a mathematical model with the basic characteristics of the system so that we are not bothered by too much complexities, (c) quantitative analysis of a system using known parameters in a mathematical model, (d) abstraction or generalization of real system behavior for the predication of some system behaviors under a condition that is theoretically possible but physically hard to implement, (e) utilization of well-developed theories. Usually system modeling is involved in determination of proper mathematical equations, and finding the optimal parameters of the model.

To model a system, we first need to know the characteristics of the system. Since we are studying the phase resetting behavior of the cardiac oscillatory system in response to respiration, we need to take into account characteristics of both the running PRC and respiration stimuli. Respiration is a periodic signal that consists of well-balanced, alternating and smooth expiration and inspiration movement. In

chapter 7, we characterized the running PRC in the topological domain. This characterization provided us with topologically recognizable shapes, that is, phase planes. We started modeling from a second order system since a second order system is simple and can generate easily analyzable phase planes. After a review of the second order system, we have chosen the Van Der Pol model for a first investigation. We will also discuss other models as a complementary investigation.

9.2 Second-order Systems

A second-order system can be described by a second-order differential equation. Study of second-order systems is important because many practically important but dynamically complicated systems can be reasonably simplified or approximated by second-order systems and can be analyzed accordingly. Since the second-order system is simple, many significant results and conclusions can be derived. Finally, several important theorems concerning phase trajectories have been formulated. In particular the phase plane,which describes the output of a second-order system and its rate, is well-known.

Because of the development of modern computers, a second-order differential equation can be solved easily by state space methods [47,49]. The use of the state-space approach offers a great deal of convenience conceptually, notationally and analytically. The conceptual advantage of the state-space approach is from its unique representation of a second-order system, that is, the state-space method describes the condition of a system in the time domain by the notation of

the so-called system state. The system state (for example, the position of an object, the velocity of an object, etc.), which is usually defined based on the interests of the analysts, can be visualized as a point in a Euclidean space and the behavior of the system as time progresses is then given by a trajectory traced out by the point on a 2-dimensional plane. The notational and analytical convenience arises through the form of the state-space equation of a system and the form of its solution, which is a compact matrix, has only first-order differentiation in the equation and can be solved easily by numerical methods developed for computers [49]. An example is now presented to illustrate the state-space approach:

$$a\frac{dx^2}{dt^2}+b\frac{dx}{dt}+cx=0 \qquad (9.2.1)$$

Equation (9.2.1) is a standard second-order differential equation, where a, b and c are constant for a linear time-invariant system. For a second-order system, there are two system states that can be defined, depending on the interest of the study. Usually one state, called x_1, is defined as x and another state, called x_2, is defined as its derivative with respect to time (dx/dt). Equation 9.2.1 can then be transformed into equations:

$$\frac{dx_2}{dt}=-\frac{c}{a}x_1-\frac{b}{a}x_2 \qquad (9.2.3)$$

$$\frac{dx_1}{dt}=x_2 \qquad (9.2.2)$$

$$\begin{bmatrix} \frac{dx_1}{dt} \\ \frac{dx_2}{dt} \end{bmatrix} = \begin{bmatrix} 0 & 1 \\ -\frac{c}{a} & -\frac{b}{a} \end{bmatrix} \begin{bmatrix} x_1 \\ x_2 \end{bmatrix} \qquad (9.2.4)$$

Equation (9.2.4) is a state space representation of the second-order system, which can be solved easily by computers using numerical methods. The numerical solution normally transforms dx into Δx and dt into Δt, and multiplies both sides of the equations by Δt. Then it begins recursion from initial conditions with proper step size Δt and ends at the specified time. The computer can perform this recursion and solve the equations rapidly.

The second-order differential equation can also be easily solved by means of frequency-domain methods, such as the Laplace transform and Fourier transform. However, when a system to be studied contains time-varying or nonlinear elements, utilization of the frequency-domain transform method becomes restricted; the state-space method can nevertheless produce a state-space equation that can be easily solved numerically by a computer. In this work the state-space representation is especially useful. A Van der Pol equation is a typical example, which we will discuss in detail in the next section.

As we have discussed before, there are two states in a second-order system. The relationship between these two states can be easily demonstrated by the trajectory of a state plane or phase plane that is constructed by one state against the another state in the Euclidean coordinate space. In a phase plane, a state is called an equilibrium state if starting from that state, the system will not move from it in

the absence of forcing functions. For a linear second-order system, the state-space equation is given as follows:

$$\frac{dx}{dt} = Ax \qquad (9.2.5)$$

where x is a state vector consisting of two states (x_1, x_2) and A is a 2x2 matrix. The equilibrium states of the system are given by those states satisfying Ax=0. From this, we see that x=0 is the only solution as long as the determinant of the matrix A is nonzero. In other words, the origin of the phase plane of the system is the only equilibrium for a linear time-invariant system provided that the determinant of A is nonzero. Thus the study of the behavior of the linear time-invariant second-order system phase trajectories can be focused on the behavior of phase trajectories in the vicinity of the origin of the phase plane because the characteristics of the equilibrium for a linear time-invariant second order system determine trajectory behaviors around the origin.

Further, the behavior of a system as well as the trajectories of the system phase plane, are determined by the poles of the system. For a second-order system, there are only two poles that determine the system behavior. Figure 9.2.1 shows how the two poles (λ_1 and λ_2) in a second-order system play a role on the formation of its phase plane. The arrow in Figure 9.2.1 indicates the direction of the state changes as time progresses.

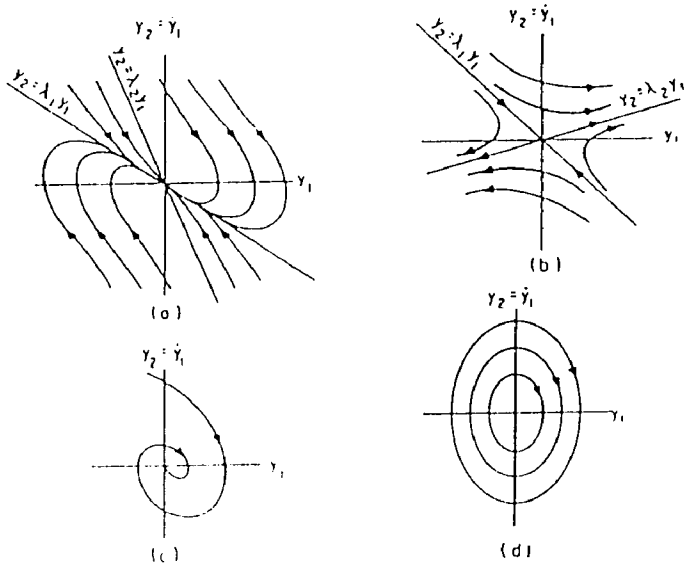

Figure 9.2.1 The state-plane portraits in the normal coordinates. (a) for $\lambda_1<0$, $\lambda_2<0$; (b) for $\lambda_1<0$, $\lambda_2>0$; (c) λ_1 and λ_2 are complex with negative real parts; (d) λ_1 and λ_2 are purely imaginary.

For the system with two negative poles, its trajectories fall into a node at (0,0) as shown in Figure 9.2.1(a), which is called stable equilibrium point. For the system with one negative pole and one positive pole, which is displayed in Figure 9.2.1(b), the trajectories approaching to the node (0,0) will eventually be deflected away from it. This node is called saddle point. Figure 9.2.1(c) shows the trajectory for the system with complex poles that have negative real parts. The trajectory is a spiral that will converge toward the node (0,0). For the system with poles that are purely imaginary, its trajectories are circles centered about the node (0,0) as shown in Figure 9.2.1(d).

The linear second-order system we have discussed has the characteristics of a single equilibrium point, and the properties of the entire phase plane are reflected by the behavior of the trajectories in the vicinity of the origin of the phase plane.

The study of characteristics of a linear time-invariant system is helpful to analyze the nonlinear system. However, a linear system is a special case of a nonlinear system when the nonlinearity of the system is zero. In Figure 9.2.1, we can see that for a linear second-order system oscillation can take place only when the two poles are purely imaginary. A slight change of the system parameters (for example, one pole is changed from an imaginary value to a complex value) will end the oscillation of the system. Also the amplitude of the oscillation depends on the initial condition, the starting point of the two states. In nonlinear systems, amplitude of the oscillation is independent of the initial condition. The corresponding trajectory of the system phase plane is a limit cycle, which we will definite in the next, instead of a circle in linear systems. A further property of limit cycle type oscillation is that the oscillation is usually much less sensitive to system parameters. In particular, there usually exist finite ranges of parameter values over which the oscillation can be sustained.

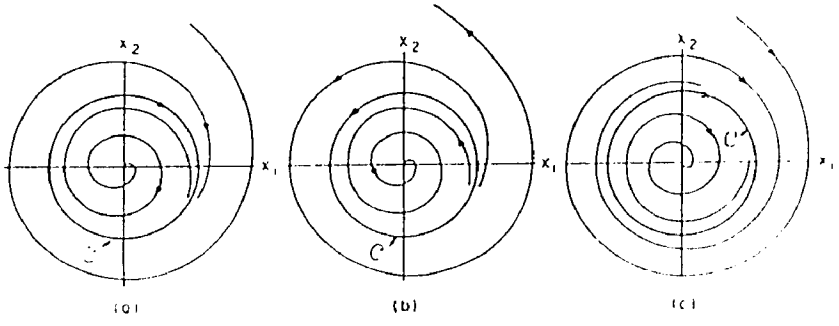

Figure 9.2.2 (a) A stable limit cycle; (b) An unstable limit cycle.; (c) A semi-stable limit cycle.

A limit cycle is defined as a closed curve in a phase plane with one of the

following features [47]. Feature I: All system trajectories in the vicinity of a closed curve ultimately tend toward the closed curve as time approaches infinity as shown in Figure 9.2.2 (a), this closed curve is a stable limit cycle; Feature II: All system trajectories in the vicinity of a closed curve, starting from any points close to the closed curve, tend away from the closed curve as time approaches to infinity as shown in Figure 9.2.2 (b). This closed curve is an unstable limit cycle; Feature III: All system trajectories in the vicinity of a closed curve fall into two exclusive classes, one class of trajectories tend toward the closed curve while another class of trajectories tend away from the closed curve as time approaches to infinity as shown in Figure 9.2.2 (c). This closed curve is a semi-stable limit cycle.

In addition to limit cycles, a nonlinear system can have multiple modes of behavior.The multiple modes occur in cases when a second-order system has a multiple of isolated equilibrium states or has different behaviors in the different regions of a phase plane surrounding the same equilibrium state.

9.3 Van Der Pol Model

A Van der Pol oscillator is a typical nonlinear second-order system, which is described by a second-order differential equation [46]. The reason that the Van der Pol model can be adapted for our phase resetting study is due to the following of its special features. The output of the Van der Pol model is an oscillatory signal with an endogenous period and is capable of describing cardiac oscillatory activity around its natural period. The nonlinearity of the Van der Pol model can be

adjusted to reflect the nonlinear dynamic activity existing in the running PRC (the nonlinear dynamic activity has been illustrated by the dispersion of the phase plane of the running PRC in the topological study in chapter 7 and in the information dimension analysis in chapter 8). Further, two coupled Van der Pol oscillators allow us to adjust their frequency ratio so that the frequency dependence of the phase plane of the running PRC can be investigated. In our study, we will use the Van der Pol model to explain and better understand some characteristics of the PRC.

9.3.1 A Van Der Pol Model

The differential equation of the Van der Pol oscillator is as follows:

$$k^2\frac{d^2x}{dt^2}+\mu\ k(x^2-1)\frac{dx}{dt}+\omega^2 x=0 \qquad (9.3.1.1)$$

where ω is the endogenous frequency of the Van der Pol oscillator and μ is a parameter that determines the nonlinearity of the oscillator. The value of ω can be easily derived by assuming μ to be zero so that the consequent oscillator becomes a pure sinusoidal wave generator. The frequency of the sinusoidal wave is ϖ. μ=0 is a special case, in which the oscillator becomes a linear oscillator. The linear oscillator produces a pure sinusoidal wave with a fixed frequency. The nonlinear oscillator is able to generate multiple frequency components or harmonic components in its output signal in addition to the dominant sinusoidal wave. The

larger the value of μ, the higher the degree of the nonlinearity.

Since modern numerical methods developed for computers can only be used to solve first order differential equations, we need to transform equation (9.3.1.1) into state equations in order that numerical solution can be obtained using a computer. The state equations are as follows:

$$\frac{dx_1}{dt} = x_2 \qquad (9.3.1.2)$$

$$\frac{dx_2}{dt} = -\frac{\omega^2}{k^2} x_1 - \frac{\mu}{k}(x_1^2 - 1) x_2 \qquad (9.3.1.3)$$

The above equations are derived by assuming x as a state variable x_1 and derivative of x as another state variable x_2. We have developed a software package interacting with Splus for the Van der Pol model (the software description is given in Appendix V).

Figure 9.3.1.1 shows an output of the Van der Pol model described in equations (9.3.1.2) and (9.3.1.3), and the corresponding phase plane. The parameters are k=3.82, μ = 0.2, ω = 1.92. Figure 9.3.1.1 (a) is a oscillation wave. Figure 9.3.1.1 (b) is the corresponding phase plane constructed by x_2 via x_1, which shows that the trajectory moves from a small circle toward the limit cycle (condensed lines).

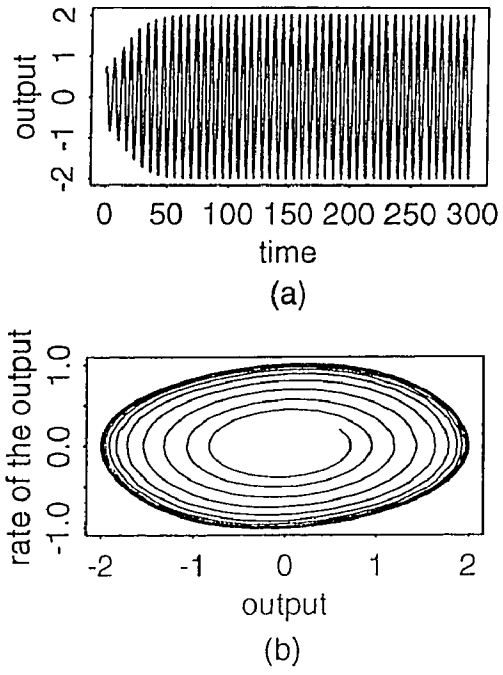

Figure 9.3.1.1 (a) Output of the Van der Pol model. (b) Phase plane for the Van der Pol model, k=3.82, μ=0.2, ω=1.92.

9.3.2 Phase Response to an Impulse

Since the Van der Pol model is a nonlinear oscillator and its trajectories, starting at an initial state, will always approach a limit cycle, it is a self-sustained oscillator and its oscillation has the period of the limit cycle. During the oscillation on the limit cycle, a perturbation to the Van der Pol oscillator causes the trajectory to move away from the limit cycle, which leads the current oscillation cycle or period to be changed into a new value (called the perturbed period) instead of the period of the limit cycle. In the time domain, change of the current oscillation period means that the following oscillation cycle will be advanced if the perturbed period is shortened or will be delayed if the perturbed period is prolonged. This phenomenon is called "shift of the phase of the oscillation", in which phase is the

perturbed period. A small perturbation or stimulation to the Van der Pol model induces the trajectory away from the limit cycle and produces a phase shift of its oscillation. After the stimulation, the trajectory will approach the limit cycle in a few cycles (normally 2 or 3 cycles), depending on the size of the stimulation and how far the trajectory moves away from the limit cycle in response to the stimulation. A large perturbation may cause the trajectory to approach the equilibrium point at the origin of the phase plane, and without any force the trajectory is not able to go back into the limit cycle so that the oscillation stops. The equilibrium point that terminates the oscillation is also called a singular point. Figure 9.3.2.1 shows the above situations. Figure 9.3.2.1(a) is a phase plane after the Van der Pol oscillator received a positive stimulus, which caused the trajectory to move away from the limit cycle in an inward direction and approached the limit cycle in three cycles after the stimulus was removed. Figure 9.3.2.1(b) is a phase plane after the Van der Pol oscillator was stimulated by a negative impulse, which induced the trajectory away from the limit cycle in the outward direction and approached the limit cycle in two cycles. When the positive stimulus was increased, it took more cycles for the perturbed trajectory to return to the limit cycle as shown in Figure 9.3.2.1(c). When a large stimulus was delivered, the Van der Pol oscillator was terminated and the perturbed trajectory ended in the singular point as shown in Figure 9.3.2.1(d).

We have used the impulse stimulus to perturb the Van der Pol oscillator and studied its phase response behavior. Figure 9.3.2.2 (in Appendix IV) shows the

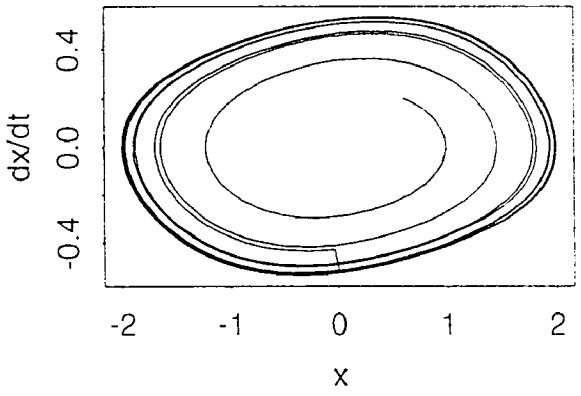

(a) A positive stimulus.

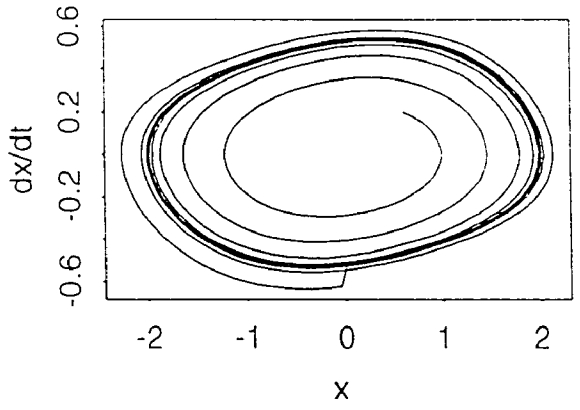

(b) A negative stimulus.

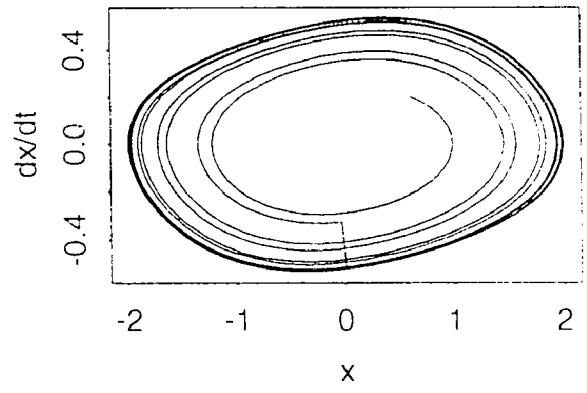

(c) An increased positive stimulus.

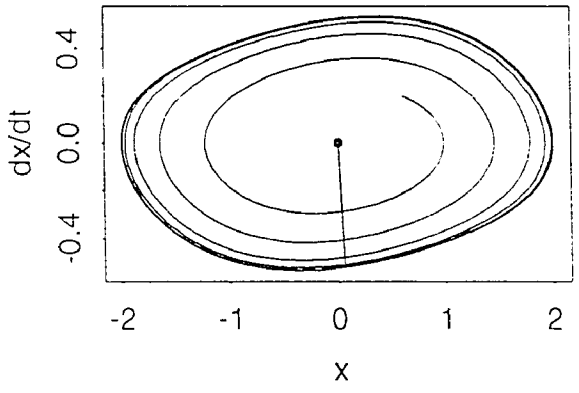

(d) A large stimulus.

Figure 9.3.2.1 A Van der Pol model in response to different impluse stimulus

detailed perturbation process, in which an impulse stimulus represented by a solid vertical line was delivered at different times in a oscillation cycle and the consequent period of the oscillation cycle was measured. The phase response curve was constructed by the difference between the period of the perturbed oscillation cycle and the period of the limit cycle, normalized by the period of the limit cycle.

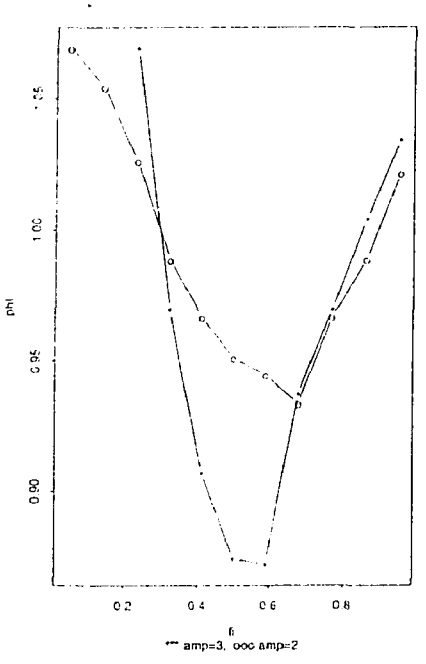

Figure 9.3.2.3 Phase response curves at different stimulus amplitudes (amp=2 and amp=3).

Two phase response curves are presented in Figure 9.3.2.3 to show the phase resetting behavior of the Van der Pol oscillator in response to an impulse and also to illustrate that the amplitude of the phase shift depends on the time when a stimulus is delivered and the amplitude of the stimulus. The x axis represents the phase of the stimulus and is the percentage of the oscillation period at which a stimulus is given. The y axis represents the perturbed period, in which values above

1.00 mean the oscillation period is prolonged (phase delay) while values below 1.00 mean the oscillation period is shorted (phase advance). It is found that changes of the oscillation periods (phase shifts) are different at different phases of the stimulus. Thus the phase shift depends on the time of the stimulus. It is also found that a larger stimulus causes a larger phase shift. Thus the phase shift depends on the amplitude of the stimulus.

9.3.3 Two Coupled Van Der Pol Oscillators

A Van der Pol oscillator perturbed by a single stimulus generates phase resetting and its phase resetting behavior can be used to illustrate the phase dependence of a self-sustained oscillator. It is quite useful to simulate the phase resetting behavior of the cardiac oscillator in response to a single stimulus. However, the cardiac oscillator in response to the respiration stimulation is a continuous perturbation process because the heart is under a constant influence of respiration-associated vagal activity. Therefore a continuously-perturbed Van der Pol model may be needed to simulate the phase resetting behavior of the cardiac oscillator in response to respiration stimulation. There are two possible models we have considered for the continuous perturbation. One model is a Van der Pol oscillator perturbed by a linear oscillator and perturbation is a one-way control process. The linear oscillator is not affected by the Van der Pol oscillator. Another possible model is two coupled Van der Pol oscillators where the two oscillators interact with each other. We have chosen two coupled Van der Pol oscillators as a reasonable model for our

study because the heart is under the influence of respiration on one hand and respiration is also affected by the heart on the other hand. Heart and respiration interact with each other. The cardiac oscillator is considered as one Van der Pol oscillator and the respiration as another oscillator. The phase resetting behavior of the cardiac oscillator due to the respiration is determined by the coupling factors. The model of the two coupled Van der Pol oscillator is as follows:

$$k_x^2\frac{d^2x}{dt^2}+\mu_x k_x(x^2-1)\frac{dx}{dt}+\omega_x^2 x+g_{xy}y+f_{xy}\frac{dy}{dt}=0 \qquad (9.3.3.1)$$

$$k_y^2\frac{d^2y}{dt^2}+\mu_y k_y(y^2-1)\frac{dy}{dt}+\omega_y^2 y+g_{yx}x+f_{yx}\frac{dx}{dt}=0 \qquad (9.3.3.2)$$

where f_{xy} and f_{yx} are the direct coupling coefficients between the x and y oscillators while g_{xy} and g_{yx} are velocity coupling coefficients between the x and y oscillators. This model provides us with many flexible ways to study the interaction between the heart and respiration. The following is noted:

(a) Choosing $\mu_x = 0$, we can study characteristics of a Van der Pol oscillator coupled with a linear oscillator;

(b) Choosing $g_{xy} = g_{yx} = 0$, we can evaluate aspects of two coupled oscillators coupled by their amplitudes;

(c) Choosing $f_{xy} = f_{yx} = 0$, we can examine how the slope of the oscillation wave from one oscillator affects another oscillator;

(d) Choosing different ratio ω_x/ω_y, we can estimate what role the change of the frequency ratio between two coupled oscillators may play on

the system features;

(e) Choosing all parameters as nonzero value, we can inspect the combined effects of two coupled oscillators on the system behaviors.

Figure 9.3.3.1 (in Appendix IV) shows phase planes for different nonlinearities during velocity coupling. We can see that a big increase of the nonlinearity μ of the two coupled oscillators, will change the basic shape of the trajectories and increase the amount of trajectory bending. It is observed that with larger nonlinearity, the system oscillation tends to be attracted to the limit cycle.

To see how the way of the coupling affects the phase plane, we have compared the phase planes during direct coupling ($f_{xy}=f_{yx}=0$) with the phase plane during the velocity coupling ($g_{xy}=g_{yx}=0$). The results are shown in Figure 9.3.3.2 (in Appendix IV). We have found that at the same condition the oscillator is more sensitive to velocity coupling than direct coupling since velocity coupling increases the complexity of the system state plane (phase plane). We have also investigated how the coupling coefficients play the role on the phase plane. The results are shown in Figure 9.3.3.3 (in Appendix IV). It is observed that the stronger the coupling between two oscillators, the more complicated the system states.

The coupling factors include the method of coupling (direct and/or velocity coupling), coupling coefficients, and the coupling frequency (frequency ratio between two oscillators). The system state planes related to different frequency ratios are illustrated in Figure 9.3.3.4. It is noticed that an increase of the frequency

ratio between two oscillators induces an increase of the trajectory bending number and degree. Therefore the structure of the phase plane becomes more complicated when the coupling frequency ratio is increased. Also the difference between phase planes with integer frequency ratio and phase plane with fractional frequency ratio has also been observed in Figure 9.3.3.4. The phase plane with fractional frequency ratio has more overlapped trajectories while the phase plane with integer frequency ratio has more trajectories following the same pattern but in different positions.

From the above simulation, we conclude that the increase in the complexity of the phase plane of the running PRC with an increase of the pacing rate may be due to the increase of the nonlinearity and the frequency ratio in the cardiac oscillator in the interaction with respiration cycles since the nonlinearity and the frequency ratio contributes to the complexity of the phase plane.

9.4 Generalized Additive Model

The generalized additive model (GAM) uses an adaptive approach to fit the real data and models the terms nonparametrically using a scatterplot smoother. The output of the GAM can estimate the coefficients, evaluate and examine the fits. In particular, the estimated residual and partial residual plots can be used to illustrate discrepant observations and to identify nonlinearities.

The general form of the additive model is as follows [48]:

$$n(x) = f_1(x_1) + f_2(x_2) + \ldots\ldots + f_p(x_p) \qquad (9.4.1)$$

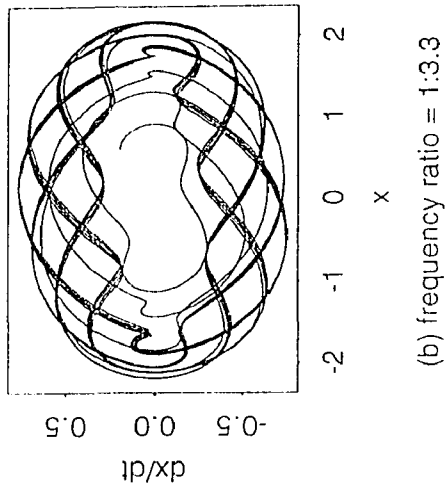

(b) frequency ratio = 1:3.3

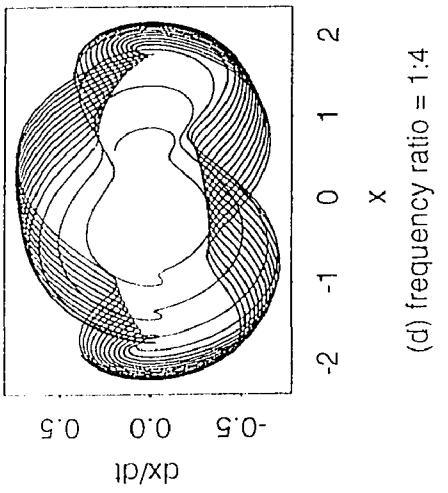

(d) frequency ratio = 1:4

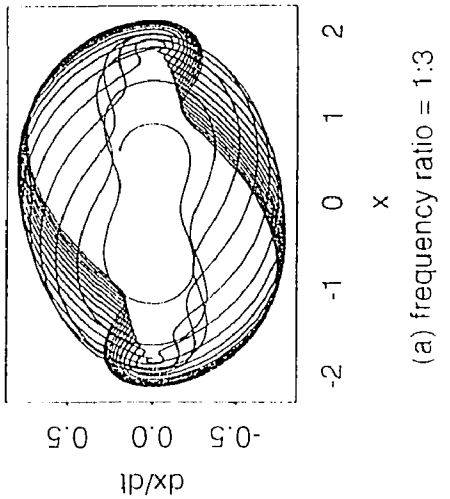

(a) frequency ratio = 1:3

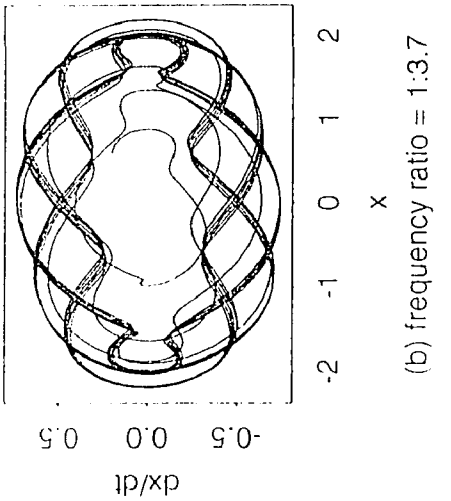

(b) frequency ratio = 1:3.7

Figure 9.3.3.4 Phase planes during different coupling frequency ratios.

where each of the x_i are predictors and the f_i are transform functions of the predictors or terms. The $n(x)$ consists of different parametric functions, which may be polynomials, logarithms, sinusoids, step functions and other functions. These functions either add together to fit the real data or fit the real data in a piecewise fashion. The form of the mathematical expression of the GAM is simple. The additive model also has an appeal of flexibility since we have a lot of options to choose various functions to fit the real data. However sometimes it is very difficult and time-consuming to determine the correct transform functions for each variable and combine them in a correct additive way for the modeling. Therefore using the parametric transform functions for the modeling limits the popularity of the additive model.

A solution of the above problem is to use regression algorithms. Thus the parametric transform functions in equation (9.4.1) are replaced by the nonparametric regression fitting functions, which are the scatter data smoothers and will be described in the next. This overcomes the shortcomings of the parametric modeling and provides more flexibility to the users. Since nonparametric transforms deal with local data fitting instead of the parameters of the parametric transform, large computation time are usually needed. In order for the nonparametric techniques to be used easily, they must be supported by some well-developed and easily-mastered software. In our study, we have used Splus software to do the general additive modeling.

Splus is a language and an interactive programming environment for data

analysis and graphics, and is a very high level language for specifying computations. The primary facilities in Splus include (a) organizing, storing and retrieving all sorts of data; (b) providing numerical methods and computational techniques; (c) allowing users to program and produce new functions; (d) interfacing with other kinds of computer languages such as C and Fortran, and Unix and DOS commands; (e) graphics capabilities. Here we introduce some Splus functions that are used in our nonparametric modeling.

A. **gam**(formula): The function "gam" is used to generate a fit of the generalized additive model. The argument "formula" of the gam function is of the following form:

output ~ f(input A) + g(input B) + ... + h(input X)

where f, g, ... and h are smoothing transform functions. The input A, B, and X are the given data sets related to the output.

B. **poly**(x,n): The function "poly" is a smoothing transform function and is able to generate a basis of polynomial regression. The argument "x" of the function poly is a given data or a predicator. The argument "n" of the function "poly" is a parameter used to specify the degree of the polynomial transform.

C. s(x,df): The function "s" is a smoothing transform using the spline method. The argument "x" is the same as in B. The argument "df" of the function s is used to

specify the degree of freedom of the smoothing spline transform.

D. **lo**(x,span,degree): The function "lo" is a scatter-plot smoothing transform and uses the robust locally linear fit. The argument "x" is the same as in B. The argument "span" of the function "lo" is used to specify the range of a neighborhood of data points to be accounted. The argument "degree" has two options: degree = 1 means a local linear fit while degree = 2 means a local quadratic fit.

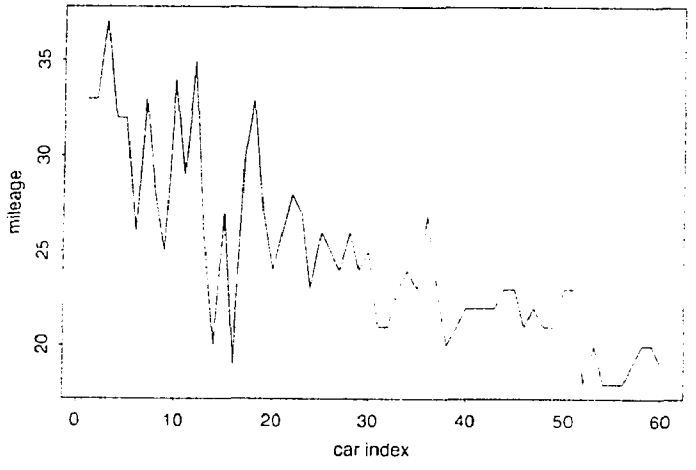

Figure 9.4.1 Car mileages for different cars.

In Appendix I we give the detailed description of the above Splus functions. In order to illustrate how the generalized additive model (GAM) works, we present an example here. The data in our example is from a car test data frame as shown in Appendix II. Figure 9.4.1 shows car mileage for different cars and the mileage

distribution will be modeled using the GAM. Since the car mileage mainly depends on the car weight and the horse power of a car, the predicator are selected as the car weight and the horse power. If the function "s" is used as the smoothing transform, the modeling can be done as follows:

gam(mileage ~ s(weight) + s(HP))

where HP represents horse powers for different cars and weight is a data set consisting of weights for different cars, which are illustrated in Appendix II. Mileage is the mileage data for different cars as shown in Figure 9.4.1. The transform "s" is a spline smoothing. The simulation result is given in the following form:

Degrees of Freedom: 60 total; 51 Residual

Residual Deviance: 306.3506

where "Degrees of Freedom: 60 total" means total number of data points simulated, and "51 Residual" means that the number of residuals derived is 51. The residual represents the difference between the real mileage data and the simulated data consisting of the addition of the contributions from the car weight data and the horse power data. The "Residual Deviance" is the summation of the square of the residuals. Figure 9.4.2 shows that the above additive model relates the car mileage shown in Figure 9.4.1 to the car weight and the horse power. Each plot illustrates the contribution of a term (transformed predictor) to the model. The solid line in Figure 9.4.2 (a) represents the simulated result and the contribution from the

weight. The solid line in Figure 9.4.2 (b) represents the simulated result and the contribution from the horse power. It can be seen that with an increase of the car weight the simulated mileage data represented by the solid line in Figure 9.4.2 (a) declines. However, change of the horse power does not significantly affect the mileage, which is illustrated by a flat solid line in Figure 9.4.2 (b). Therefore, the car weight plays a more important role on the car mileage than the horse power.

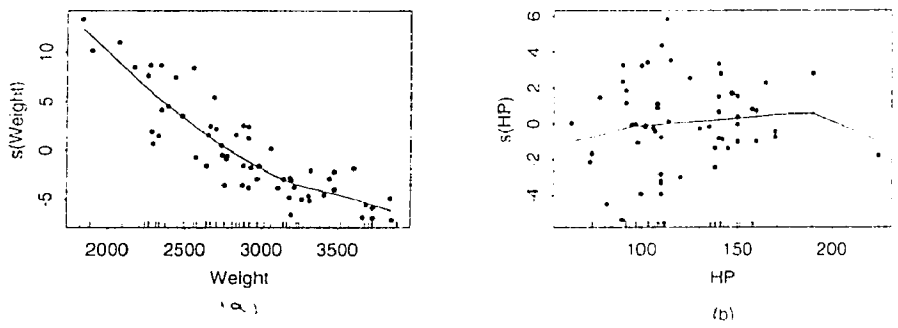

Figure 9.4.2 An additive model relates Mileage to Weight and HP.

Since the generalized additive model provides us with flexible ways to investigate the relationship between phase resetting and respiration, we have used the GAM to model the phase resetting data. We have derived the following additive models using the GAM:

(a). gam(Prc ~ s(Coup) + s(Resp.amp))

(b). gam(Prc ~ poly(Coup) + poly(Resp.amp))

(c). gam(Prc ~ lo(Coup) + lo(Resp.amp))

where Prc is the phase response curve, Coup is a predictor of the Prc, consisting of the coupling intervals and Resp.amp is another predictor of the Prc, consisting of the amplitudes of the respiration at coupling interval points. The transform "s" is a spline smoothing, the "poly" is a transform generating a basis for polynomial regression, and the transform "lo" is a robust locally weighted regression; the functions were described before in this section and are described in detail in Appendix I. The following table shows the results of the three models.

Table 9.4.1 The GAM models at different transforms

	Degree of Freedom	*Residual Numbers*	*Deviance*
poly	*150*	*147*	*0.22738*
lo	*150*	*142*	*0.17953*
s	*150*	*141*	*0.17458*

Since we have chosen the coupling interval and respiration amplitude as two major predictors related to phase resetting behavior, the modeling becomes a question of how to select smoothing transform functions in order to fit the real PRC data. The quality of the fit can be evaluated by the deviance. From Table 9.4.1, we can see that different smoothing transforms have different qualities of fit, and the model of Prc = f(Coup) + g(Resp.amp) using the spline smoothing

transform "s" is the best because the model gives the smallest deviance among these three models.

In order to reduce the deviance of the model, we need to take more factors into account, which will increase the complexity of the model. As we have discussed in chapter 6, a phase shift depends on the time of the stimulus (coupling interval) and the amplitude of the stimulus (respiration amplitude). Since the slope of impedance pneumography (respiration) may have some impact on the phase resetting behavior of the cardiac cycle, we included the slope of respiration in the model and the three models we presented before will be:

(a). gam(Prc ~ s(Coup) + s(Resp.amp) + s(Resp.slope))

(b). gam(Prc ~ poly(Coup) + poly(Resp.amp) + poly(Resp.slope))

(c). gam(Prc ~ lo(Coup) + lo(Resp.amp) + lo(Resp.slope))

where Resp.slope represents the slope of the respiration. A similar table has been created to show the improvement of the models:

Table 9.4.2 The improved models

	Degree of Freedom	*Residual Numbers*	*Deviance*
poly	*150*	*146*	*0.2265*
lo	*150*	*138*	*0.17692*
s	*150*	*137*	*0.17072*

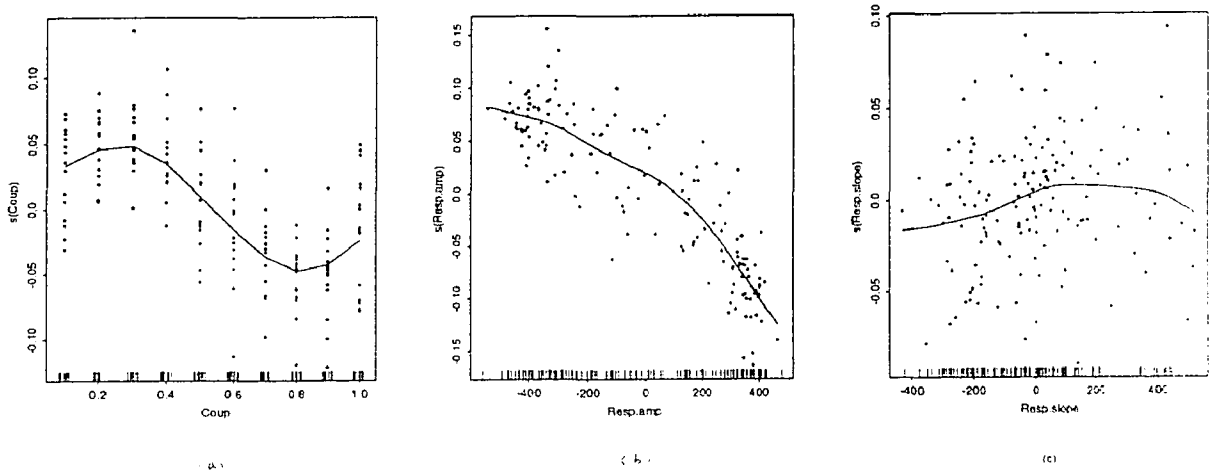

Figure 9.4.3 An additive model used to show the contributions of coupling interval, respiration stimulus and slope of respiration to the PRC.

We can see that deviances have been reduced due to the increase of number of predicator by comparing Table 9.4.2 with Table 9.4.1. Figure 9.4.3 shows the contributions of the coupling interval, respiration amplitude and the slope of respiration to the PRC, which is obtained using the spline smoothing transform since it produces minimal deviance in the models. The solid lines in Figure 9.4.3 represent the contributions from coupling interval, respiration amplitude and respiration slope. The contribution of the coupling interval to the phase response curve ("Prc" in the model) is: In the first half of the coupling interval the phase shift represented by the solid line in Figure 9.4.3 (a) is positive while in the second half of the coupling intervals the phase shift is negative. The contribution of the

respiration amplitude is: The positive amplitude of respiration induces the negative phase shift represented by the solid line in Figure 9.4.3 (b) while the negative amplitude of respiration induces a positive phase shift. Further, the larger the amplitude of respiration, the larger the phase shift. The relation between the phase shift and the amplitude of respiration is not linear as shown by the solid line in Figure 9.4.3 (b). The contribution of the slope of respiration is: The positive slope of respiration produces a positive phase shift shown by the solid line in Figure 9.4.3 (c) while the negative slope of respiration produces a negative phase shift. The relation between the phase shift and the slope of respiration is not linear. However, compared with the coupling interval and the respiration amplitude, the contribution of the slope of respiration is much smaller. Thus respiration amplitude and coupling interval play the major role on the phase resetting and the slope of respiration has a minor effect on the phase response curve, which can be visualized by the flat line in Figure 9.4.3 (c).

The generalized additive model uses statistical techniques to simulate the real data. The quality of the simulation depends on how many predicators are considered in the model and what transform is used. An increase of the number of possible predictors can improve the accuracy of the simulation, but increases the complexity of the model analysis. Selection of the transform is normally done by comparing the deviances of the model using various transforms. The smaller the deviance, the better the model. For the phase resetting study, we have considered the coupling interval, the respiration amplitude and the respiration slope as the

predictors for the PRC simulation since our present study indicates that the phase shift depends on these three variables. The transforms we have selected are three commonly used algorithms in the general additive model, spline smoothing, polynomial regression and robust locally weighted regression. Our study demonstrated that the spline smoothing was a better choice since it produced a smaller deviance.

9.5 Knight and Peskin's Models

In this section, we will introduce three models discussed by Knight and Peskin [40][41], which are used to demonstrate the relationship between firing rate of "pacemaker" and input stimulus. These three models are (a) Knight's simple integrate-and-fire model (IAF), which yields the firing rate of a "pacemaker" maintaining a perfect copy of the input stimulus, (b) Knight's forgetful integrate-and-fire model, which yields the firing rate of a "pacemaker" being a much degraded copy of the input stimulus, (c) Peskin's model, which is a modified forgetful integrate-and-fire model, in which the stimulus depends on the "pacemaker" behavior. We will limit our study to a theoretical investigation.

A. Knight's simple integrate-and-fire model [40]

$$\frac{du}{dt} = s(t). \qquad (s(t) \geq 0) \qquad (9.5.1)$$

Knight's simple IAF model is characterized by the above mathematical equation.

where u is the value of the internal variable of the "pacemaker" and $s(t)$ is a stimulus. Since $s(t)$ is greater than zero, the u will increase with time. When u achieves a criterion level C (called threshold), the "pacemaker" fires an impulse, u is reset to zero and the process starts again. Therefore the "pacemaker" follows a repetitive resetting process. The point of resetting depends on the stimulus value. In general, larger stimuli will induce a faster speed for u to reach the threshold so that a higher firing rate will be generated.

From equation (9.5.1) and the above discussion, we can see that the instantaneous firing period of a "pacemaker" is determined by the time since its last firing. The reciprocal of the instantaneous period is the instantaneous firing rate. The relationship between instantaneous rate and stimulus may be derived by integrating equation (9.5.1) once. Then

$$C=\int_{t_n}^{t_{n+1}} s(t)\,dt \qquad (9.5.2)$$

where t_n and t_{n+1} are the times of the nth and $(n+1)$th impulses, respectively. If the stimulus is constant s_0, then

$$C=(t_{n+1}-t_n)\,s_0 \qquad (9.5.3)$$

or if f_0 is assumed to be the instantaneous rate, then

$$f_0 = \frac{s_0}{C} \qquad (9.5.4)$$

Thus the firing rate is linearly proportional to the stimulus. Since C is a constant, the firing rate is a perfectly linear copy of the stimulus. This is a simplest case. However the result of (9.5.4) can also be used in the situation during which the stimulus $s(t)$ changes by only a very small fraction of its value between two impulses. The following derivation is used to illustrate what degree of error may be made by this approximation. $s(t)$ can be expanded at t_n by a Taylor series

$$s(t) = s(t_n) + s'(t_n)\,(t - t_n) + \ldots \qquad (9.5.5)$$

and is substituted into equation (9.5.2), which gives

$$C = \frac{1}{f}s + \frac{1}{2f^2}s' + \ldots \qquad (9.5.6)$$

where f is the instantaneous firing rate. Multiplying equation (9.5.6) on both sides by f/C and assuming $s \gg | s'/f |$ leads to

$$\begin{aligned} f &= \frac{1}{C}s + \frac{1}{2C\left(\frac{1}{C}s + \frac{1}{2Cf}\right)}s' + \ldots \\ &\approx \frac{1}{C}s + \frac{s'}{2s} \end{aligned} \qquad (9.5.7)$$

The major error is from the term $s'/2s$. If this term is much smaller than s/C, the linear relationship is still a reasonable approximation. If the error term is not small, the firing rate can not be considered as a linear copy of the stimulus.

In the following, we will discuss how the instantaneous firing rate follows a periodic stimulus which consists of a small fluctuation about a steady mean level. In equation (9.5.2), t_{n+1} is the time of the present impulse and t_n is the time of the last. The instantaneous period T equals to $(t_{n+1} - t_n)$. A constant stimulus s_0 corresponds to a constant firing period T_0 as illustrated in equation (9.5.4) where f_0 is the reciprocal of T_0. Let stimulus $s(t) = s_0 + s_1(t)$ and the corresponding firing period $T = T_0 + T_1$, which means that a perturbation stimulus s_1 causes a change T_1 in the period. The integration in equation (9.5.2) is approximated and linear perturbation theory is adopted to obtain the following result:

$$f_1(t) = \frac{1}{T_0^2} \int_{t-T_0}^{t} \frac{s_1(t')}{s_0} dt' \qquad (9.5.8)$$

The detailed derivation is given in Appendix III. Equation (9.5.8) tells us that change of the firing rate $f_1(t)$ is proportional to the running average of the stimulus perturbation over the last T_0 time period. If $s_1(t)$ fluctuates periodically and can be expressed mathematically by $s_1(t) = s_1(0)e^{i\omega t}$, the frequency response of $f_1(t)$ can be evaluated by integrating (9.5.8)

$$f_1(t) = \frac{1}{T_0^2} \int_{t-T_0}^{t} \frac{s_1(0)\, e^{iwt'}}{s_0} dt' \qquad (9.5.9)$$
$$= \frac{s_1(0)\, e^{iwt}}{T_0^2 s_0} \frac{1-e^{-iwT_0}}{iw}$$

Since $s_1(0)e^{iwt} = s_1(t)$ and $f_0 = 1/T_0$, equation (9.5.9) becomes

$$\frac{f_1}{s_1} = \frac{f_0}{s_0} \frac{1-e^{\frac{-iw}{f_0}}}{iw/f_0} \qquad (9.5.10)$$
$$= \frac{f_0}{s_0} B\left(\frac{w}{f_0}\right)$$

Three conclusion can be derived from the above result (equation 9.5.10). (a) The ratio of f_1/s_1 reflects how the firing rate follows the change of the stimulus. From equation (9.5.10), it is clear that this ratio is independent of time. (b) The ratio is also independent of amplitude of the s_1. (c) Since this ratio is a complex number, its magnitude shows the amplitude relationship between firing rate and stimulus while its phase shows the phase shift of the firing rate to the stimulus. The

amplitude and phase relationship between firing rate and stimulus is displayed in Figure 9.5.1. For a slow oscillation of the stimulus (with a small w comparing with firing rate f_0), the flat curve in Figure 9.5.1 suggests that firing rate following the change of the stimulus is a linear replica. When the frequency $w/2\pi$ of the stimulus rises and approaches the unperturbed firing rate f_0, the perturbation of the stimulus s_1 to the firing rate f_1 decreases and approaches a cut-off. The ratio of the firing rate f_1 and the perturbation force s_1 is frequency-dependent. If the frequency of the perturbation s_1 is an integer multiple of the unperturbed frequency f_0, the ratio will be zero. This phenomenon can be easily explained by inspecting equation (9.5.9) in which " $1-e^{-iwT0}$ " is zero if $w=2\pi nf_0$ (n is integer).

Knight's IAF model is a simple model to show the firing rate linearly follows the stimulus. This model can be used for our phase resetting study. As we have discussed in the previous chapters, the change of the cardiac cycle with respect to the reference period is entrained by respiration. This entrainment phenomenon is similar to the output of the IAF model if we assume respiration to be a stimulus signal with a baseline s_0 and with an inspiration-expiration fluctuation s_1 with respect to the baseline, the reference period in our PRC study is assumed to be T_0 $(1/f_0)$, and the change of the cardiac cycle (phase shift) is assumed to be T_1 $(1/f_1)$. Therefore, the relation between the phase shift and the amplitude of respiration after removal of the baseline can be modeled by equation (9.5.10). However, the relation between the phase shift and the amplitude of respiration is, in fact, not linear. The IAF model can only be used for situations during which a

linear relationship between the firing rate and the stimulus can be established.

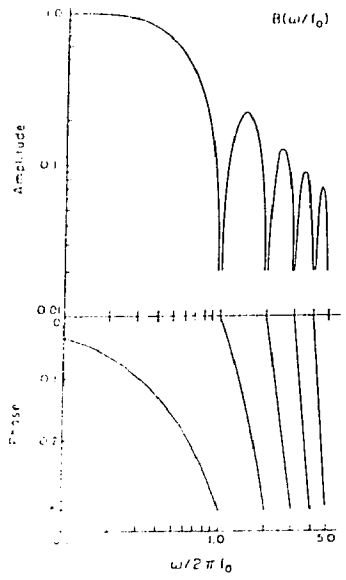

Figure 9.5.1 The function B, amplitude and phase.

B. Knight's forgetful integrate-and-fire model [40]

The Knight's forgetful IAF model is described as follows:

$$\frac{du}{dt} = -ru + s(t) \qquad (9.5.11)$$

which shows a more general relationship between the firing rate and the stimulus. The simple integrate-and-fire model is a special case of the equation (9.5.11) with $r = 0$. By imposing a firing threshold at the criterion level $u = C$ and resetting u to be zero as before, the equation (9.5.11) yields

$$C=\int_{t_n}^{t_{n+1}} e^{-r(t_{n+1}-t')}\, s(t')\, dt' \qquad (9.5.12)$$

Comparing with equation (9.5.2) of the simple integrate-and-fire model, we find that the stimulus *s(t)* is weighted by a decaying exponential. Therefore the time needed for u to reach the threshold C depends more strongly on the immediate past history than on its distant past. If the stimulus *s(t)* is a constant s_0, the integration of equation (9.5.12) will lead to

$$f_0=-\frac{r}{\ln[1-(rC/s_0)]} \qquad (9.5.13)$$

Equation (9.5.13) can be further simplified by an approximation of $ln(1-(rC)/s_0)$ using the Taylor expansion:

$$\ln(1-(rc/s_0)) \approx \frac{rc}{s_0}+\frac{1}{2!}\left(\frac{rc}{s_0}\right)^2 \qquad (9.5.14a)$$

Thus, the response of the forgetful integrate-and-fire model to the constant stimulus is the firing rate of simple IAF model offset by the half of the time constant of the

$$
\begin{aligned}
f_0 &\approx \frac{r}{\frac{rc}{s_0} + \frac{1}{2}\left(\frac{rc}{s_0}\right)^2} \\
&= \frac{s_0}{c}\left(\frac{1}{1+\frac{rc}{2s_0}}\right) \\
&\approx \frac{s_0}{c}\left(1-\frac{rc}{2s_0}\right) \\
&= \frac{s_0}{c} - \frac{r}{2}
\end{aligned}
\qquad (9.5.14b)
$$

decaying weight in equation (9.5.12).

Similarly, substitution of $s(t) = s_0 + s_1(t)$ into equation (9.5.12) where $s_1(t) = e^{iwt}$ and $T = T_0 + T_1(t)$ with $rT1 << 1$ produces the following result:

$$
\frac{f_1}{s_1} = \frac{f_0}{s_0} e^{\frac{r}{f_0}} \frac{1-e^{-\frac{(iw+r)}{f_0}}}{\frac{(iw+r)}{f_0}} \qquad (9.5.15)
$$

Corresponding to equation (9.5.10) derived from the simple IAF model, the response of the forgetful IAF model to a periodic stimulus has some new features. If $r = 0$, the response of the forgetful IAF model is the same as the simple IAF. However, if r is a nonzero parameter and comparable in size to f_0, the f_1/s_1 departs from f_0/s_0 by a factor

$$
A(r, f_0) = \frac{e^{\frac{r}{f_0}} - 1}{\frac{r}{f_0}} \qquad (w \approx 0) \qquad (9.5.16)
$$

The conclusion from the above result is that when the stimulation fluctuates at a very low frequency ($w \approx 0$),

(a) the perfect copy feature f_1/s_1 in the simple IAF model remains since $f_1/s_1 = f_0/s_0$ and $f_0/s_0 = C$. Any change of the mean value (s_0) of the stimulus will cause a proportional change of the natural firing frequency f_0, so the f_1/s_1 ratio is unchanged.

(b) the copy feature f_1/s_1 in the forgetful IAF model is lost since f_1/s_1 depends on f_0/s_0 as well as $A(r,f_0)$. The f_0/s_0 is not a constant. Any change of the mean value s_0 of the stimulus will induce a nonproportional change of the natural firing rate frequency f_0 and a corresponding nonlinear change of $A(r,f_0)$. Thus, the ratio f_1/s_1 can not be kept unchanged and the response of the frequency shift $f_1(t)$ to the periodic stimulation is nonlinear.

(c) The null points do not exist even when w/f_0 is an integer number. From the result in equation (9.5.15), we can easily derive the following result by substituting $w = 2\pi n f_0$

$$\frac{f_1}{s_1} = \frac{f_0}{s_0} \frac{-ir}{2\pi\, n f_0} \qquad (9.5.17)$$

Knight's IAF model becomes a nonlinear model by introducing a decaying factor r, which is the forgetful IAF model. The nonlinearity of the forgetful IAF model depends on the firing rate f_0 when the pacemaker receives a constant stimulation s_0 and the decaying factor r. Figure 9.5.2 is a plot of the function

$A(r,f_0)$, which shows the nonlinear relationship between f_1/s_1 and f_0/s_0. Since the phase resetting in response to the respiration stimulus is a nonlinear control process, we can use the forgetful IAF model to simulate this control process. The assumptions are the same as before. s_0 represents the baseline of the respiration, s_1 represents the inspiration-expiration oscillation, f_0 represents the reference heart rate, and f_1 represents the change of the heart rate. However, the nonlinear relation between the f_1 and s_1 depends on r as well as f_0. Change of the f_0, which means change of the reference heart rate, also affects the f_1 that represents the phase shift in our study, which is not what we want. Therefore, the forgetful IAF needs to be modified in our study.

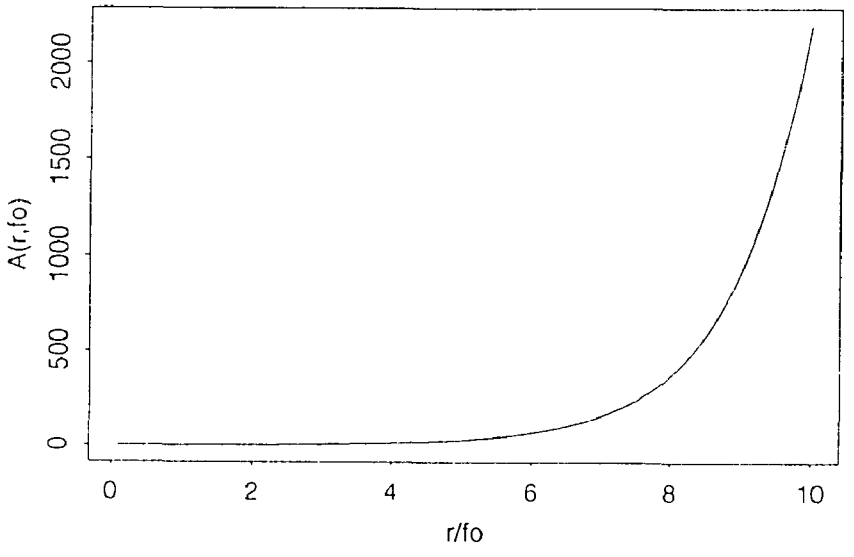

Figure 9.5.2 The function $A(r,f_0)$.

C. Peskin's model [41]

Peskin's model is a Knight's forgetful IAF model with a stimulus $s(t) = S_0 + S(t)$.

The equation is as follows:

$$\frac{du}{dt} = -ru + S_0 + S(t) \geq 0 \qquad (9.5.18)$$

Since the right side of equation (9.5.18) is greater than zero, the slope of the output u of equation (9.5.18) is positive and u is rising. When u reaches 1, the "pacemaker" fires and u is reset to zero. Then u starts rising and is reset to zero again when it reaches 1. In this way, oscillation occurs. From equation (9.5.18), we can see that the firing time of the oscillator depends on its intrinsic parameters, such as r, S_0 and its external stimulus $S(t)$ since these variables determine the rate of change of the u, and how fast the u reaches 1. Assuming $\{t_n, n = 0,1,2, \ldots\}$ is a set of firing times, the solution of equation (9.5.18) will be:

$$u(t) = \int_{t_n}^{t} e^{-r(t-t')} f(t')\, dt' \qquad (9.5.19a)$$

where f(t) = S_0 + $S(t)$. The firing time can be solved by substituting $u(t) = 1$ into equation (9.5.19a), then

$$1=\int_{t_n}^{t_{n+1}} e^{-r(t_{n+1}-t')} f(t')\,dt' \qquad (9.5.19b)$$

Assume that the external stimulus is chosen to be a periodic function with a period T, zero mean and small amplitude, which is expressed as $S(t) = \lambda g(t)$. Since $f(t) = S_0 + S(t) = S_0 + \lambda g(t)$, substitution of $f(t) = S_0 + \lambda g(t)$ into equation (9.5.19b) and utilization of Taylor expansion for approximation yields

$$\begin{aligned} 1 &= S_0 T_n + \lambda \int_{t_n}^{t_{n+1}} g(t')\,dt' - \lambda \int_{t_n}^{t_{n+1}} g(t')\,dt' \\ &= S_0 T_n + \lambda \int_{t_n}^{t_{n+1}} g(t')\,dt' - \lambda\, r \int_{t_n}^{t_{n+1}} G(t')\,dt' + \lambda\, r T_{nG}(t_n) \end{aligned} \qquad (9.5.20)$$

where

$$G(t) = \int^{t} g(t)\,dt \qquad (9.5.21)$$

Let $h(t) = g(t) + rG(t)$, then

$$1 = [S_0 + \lambda\, rG(t_n)]\, T_n + \lambda \int_{t_n}^{t_{n+1}} h(t')\,dt' \qquad (9.5.22)$$

Equation (9.5.22) is the solution of the Peskin's model to any periodic stimulus. The firing time can be obtained by performing the above recursion. It is noticed that the firing time (t_{n+1}) in the Peskin's model is a function of the previous firing time (t_n), the intrinsic parameters (λ, r and S_0), and the integral ($G(t_n)$) of the stimulus at the previous firing time. To start the above recursion, an initial time t_0 is needed. An example is choosing the period of the stimulus as $T = t_{n+1} - t_n$. Then

$$\int_{t_n}^{t_{n+1}} h(t')\,dt'=0 \qquad (9.5.23)$$

Since $G(t_n) = G(t_0)$, hence

$$\begin{aligned} 1&=[S_0+\lambda\ rG(t_0)]\,T \\ \lambda\ rG(t_0)&=\left[\frac{1}{T}-S_0\right] \end{aligned} \qquad (9.5.24)$$

The t_0 can be found from the above equation.

Peskin's model is a modification of the forgetful IAF model. The stimulus of the Peskin's model depends on the firing rate. From equation (9.5.22), we can see that the instant period T_{n+1} depends on the decaying parameter r, constant stimulus S_0, amplitude of external stimulus S_1, integration of the S_1 $(G(t))$ and preceding period T_n, which offers more flexibility to simulate the phase resetting behavior due to the respiration stimulus. However it is more complicated than both

the forgetful IAF and the simple IAF models.

We have introduced three "pacemaker" models. These three oscillators have clearly demonstrated the response of the firing rate to periodic stimulation in an approximated mathematical equation. The simple IAF model illustrates the linear relationship between the change of the firing rate and the periodic stimulus. The forgetful IAF model and the Peskin's model shows the nonlinear relationship between the shift of the firing rate and the periodic stimulus. Since our work is to study the interactive relationship between the cardiac oscillator and the respiration as the stimulus to the oscillator, these three models may provide an alternative mathematical tool for the future development.

CHAPTER 10

CONCLUSIONS

10.1 Summary of the Research

Fluctuations in heart rate have been known for a century. Study of heart rate variability, linked with human functional units such as blood pressure, thermal activity, respiration, etc., has become of great interest to physiologists and pathologists only in the past 20 years. However heart rate variability associated with the neural coupling between heart and respiration has not been completely investigated. As we have discussed before, respiration regulates the heart rate through the vagus. In this research, we examined the respiration-regulated heart rate variability (called vagal activity in our study) in the time domain using complex demodulation, studied the power of the respiration-induced heart rate variability (called vagal power in our study) in the frequency domain using spectrum analysis, and most importantly investigated the phase dependent characteristics of the heart rate variability due to the respiration-associated vagal stimulation. The results of the phase resetting study revealed the relation between cardiac phase shifts, time of respiration stimulus and amplitude of the stimulus, the topological properties of the phase response curve and the complexity of its nonlinear dynamics. Our study also included an investigation of the difference between a normal group and a group with a disease.

In the research, the experimental protocol played a critical role on the data

generation. In the vagal power study, a physical exercise protocol was adopted to drive the vagal activity of human subjects into different states by walking at different speeds on a treadmill. Changes of the vagal power were measured using the power spectrum of the heart rate variability signal. In the study of vagal activity in the time domain, a conditioning experiment was set up to generate rapid change of vagal activity so that the vagal activity underlying the heart rate variability can be complex demodulated and changes of vagal activity can be clearly evaluated. The above studies have provided us with valuable information about how the respiration-related heart rate variability changed in response to changes of the conditions of the vagal driving force. Based on the above studies, we realized that the timing and amplitude relationship between the heart rate variability and respiration were not revealed and were not able to be revealed by these two conventional time-series techniques. Therefore the phase resetting study developed in this research was meant to complement spectrum analysis and complex demodulation. The investigation of phase-dependent characteristics needs a set of fixed phases between a cardiac cycle and a stimulus, which requires well-controlled heartbeats and accurate delivery of the stimulus. Therefore most phase resetting studies are limited to surgical experiments on animals. So far the phase resetting on human hearts has not been explored. The reason may be either that the experiment is difficult or that derivation of the phasic changes of the cardiac cycle is very complicated. We found that a paced breathing protocol has advantages for this research. First, perturbation of cardiac cycles by respiration is under purely

vagal control, and pacing the heart by a fixed respiration pattern and constant frequency made the derivation of phase shifts simpler. Second, paced breathing is a noninvasive stimulation of the heart through the vagus. Third, the paced breathing provided a better respiration shape for quantization than natural breathing. But the fixed phase of the stimulus in a cardiac cycle as described by the studies on animals [4,5,7,10] and reviewed in chapter 5 is difficult to be achieved in intact awake humans using a paced breathing protocol. It is not our intention to use an invasive method. Thus we have put greater effort on mathematical manipulation and data analysis. We have made some assumptions and definitions in this research. Instead of finding the phase of the stimulus, we chose coupling intervals to locate heartbeats, and phase shifts were estimated in each coupling interval. We have found that the estimated phase response curve had some fundamentally similar characteristics, such as phase shifts related to stimulus time and amplitude, as results from animals using surgical experiments. Since the estimated phase response curves (PRCs) exist over many respiration cycles, we used a time circle method to project PRCs into one cycle so that the common pattern was enhanced and some errors due to missing beats in some cycles reduced by the mean PRC. The above methods can also be used to differentiate the normal group from the CFS group.

Analysis of the estimated phase response curve presented some challenges to us since we were trying to find a mathematical model based on the data analysis. We utilized a topological technique, the "phase plane method", to analyze the estimated phase response curve. The constructed phase planes of the real data

presented noisy topological shapes, which were hard to recognize. An effort was made to reduce the noise on the trajectories in the phase plane. It was found that the noise on the trajectories was due to insufficient number of points used to do the differentiation for the velocity derivation. Thus a smoothing algorithm, called "spline interpolation", was employed and the smoothed phase plane showed the clear pattern of the trajectories. The spline interpolation used in this research is a cubic spline and has a continuous second derivative, which is essential to construct a smoothed phase plane. We also used a Poincare map to view the topological characteristics of the PRC in a different way. The 3-D view of the data is an expansion of the 2-D work, which helps visualize the relation among three variables. Further differentiation of the normal group from the CFS group was a part of this research.

The nonlinear dynamics of the phase resetting was observed in the phase plane. Here the nonlinear dynamics are seen at the output of the nonlinear oscillator. A phase plane of the output of a linear oscillator is a circle. However, the phase plane of the output of a nonlinear oscillator shows distorted circles. In many studies, the linear behavior of the system is a focus of the research while the nonlinear dynamics is treated as noise and is ignored. In this research, we included the nonlinear dynamics because recent studies indicate that the nonlinear dynamics can be quantified by some definite laws [36]. To analyze the nonlinear dynamics, we investigated different approaches [22].Based on the basic concepts, we presented a method, called information dimension, to measure the degree of

nonlinearity and the complexity of the system.

In every part of our research discussed above, we included the study of the CFS patient since the CFS is still a mystery and is of great interest to physiologists and neurologists.

Based on the understanding of the experimental data and the analysis of the PRC, we searched for mathematical models. The modeling helps to better understand the experimental data. Since data analysis using the phase plane provided us with some recognizable topological forms and the phase plane is only meaningful to a second-order system, we started from a review of the second-order system. We found that the Van Der Pol oscillator is a reasonable second-order system for this research because the Van Der Pol model is a simple oscillator and has adjustable nonlinearity. We simulated the phase response of the Van Der Pol oscillator to an impulse and studied the relation between phase shifts and the impulse amplitude. Finally we used two coupled Van Der Pol oscillators to simulate the phase planes for different coupling situations which includes changes of coupling coefficients and ratio of coupling frequencies. In addition, we investigated a nonparametric model, the generalized additive model (GAM). The GAM, from a statistical point of view, analyzed the relationship of each possible variable, such as respiration stimulus, coupling intervals and slope of the respiration stimulus, to the phase shift. As a theoretical investigation, we viewed three possible models for the future development, which are Knight's integrate-and-fire (IAF) model, Knight's forgetful IAF model and Peskin's model.

10.2 Conclusion

Traditional time-series techniques, complex demodulation and spectrum analysis have been used to study heart rate variability associated with respiration. The respiration-related neural control, which is vagal activity, has been measured in both the time domain and the frequency domain. These techniques have become valuable tools to access the vagal nervous system. However, phase dependence of the cardiac cycle in response to vagal stimulation on the heart could not be taken into account using both spectrum analysis and complex demodulation. Thus the phase resetting study, as a complementary research, is necessary.

A noninvasive phase resetting method has been investigated in this research. The paced breathing protocol and techniques of estimation of the phase response curve have not been presented in previous phase resetting studies. Study of cardiac phase resetting in humans has been rarely seen in previous work. This research may provide an example for the noninvasive study of the cardiac phase resetting in intact awake humans.

Under our definitions and assumptions, the phase response curve was estimated and showed basic characteristics of cardiac phase resetting, such as dependence of phase on the coupling interval that is associated with phase of the respiration and on amplitude of the stimulus, entrainment and frequency dependence of phase on the pacing rate. These characteristics are fundamentally

similar to the results obtained from previous studies.

The phase plane analysis of the phase response curve was our contribution to the phase resetting study. The phase plane illustrated topological properties of the phase response curve, which provided us with much useful information for the simulation and modeling study. Also, the evidence of nonlinear output of the cardiac oscillator was displayed on the phase plane by its varying trajectories.

The information entropy and information dimension was used to measure the certainty of the phase resetting behavior and the system complexity. This study provided quantitative information about the system nonlinear dynamics. The larger the information dimension, the more variables are needed to describe the system.

The comparison between the normal group and the CFS group was a practical trial. This part of our work included the test of the practical usefulness of the phase resetting study. In this research, the above techniques were proved to be successful in the statistical differentiation of the normal group and the CFS group. It was found that the normal group had a more sensitive phase resetting response than the CFS group, given the same stimulus. The degree of the entrainment in the normal group was higher than the CFS group. The shape of the phase plane were significantly different. The normal group had the larger entropy and dimension than the CFS group.

The modeling study was done in a broad base, in which the nonlinear Van Der Pol oscillator with an impulse stimulation, two coupled Van Der Pol oscillators, generalized additive models, Knight's simple IAF model, Knight's

forgetful IAF model and Peskin's model were investigated. The modeling helped to explain and understand the real data.

10.3 Future Development of the Research

The noninvasive phase resetting study offers a totally new approach to investigate the cardiac response to respiration. Although physiologists and pathologists have made great efforts to understand the neural coupling between heart rate and respiration in the past two decades, there are still many underlying mechanisms which are unknown or unclear. The vagus, serving is controlled respiration. If the vagal nervous system can be understood completely, the vagal activity and heart rate can be regulated by the respiration. Therefore the reduced-vagal-activity associated neural diseases or heart diseases can be treated by paced breathing. An example can be found in Chinese "Qigong", which requires a person to maintain slow paced breathing and can treat "back-pain" and slow down the heart rate.

Increase of the reliability of the experimental data is another area for further exploration. The experimental data in this research was a 2-minute segment of data for every pacing rate. The longer the data length, the more reliable the data.

More pacing rates should be studied. The best pacing rate for the entrainment of the PRC to respiration stimuli should be examined.

The Knight's and Peskin's models deserve further exploration. The critical question is how to choose intrinsic parameters in the model in order that the cardiac cycle changes follow the respiration amplitude changes. The selection of models and

parameters in the model to approach the experimental data is a complex process, which we experienced in the Van Der Pol models and the GAM model. Since number of selections can be very large due to the number of combinations of many variables, modeling accuracy depends on the experiment. Therefore further investigation of the optimal and adaptive selection of parameters in the model should be made.

APPENDIX I

Splus Functions

A. gam function: Fit a Generalized Additive Model

DESCRIPTION:

Returns an object of class "gam" which is a generalized additive fit of the model.

USAGE:

gam(formula,family=gaussian,data=<<see below>>,weights=<<see below>>,subset=<<see below>>, na.action=na.fail, start=<<see below>>, control=gam.control(...), trace=F, model=F, x=F, y=T, contrasts=NULL, ...)

REQUIRED ARGUMENTS:

formula: a formula expression as for other regression models. Nonparametric smoothing terms are indicated by s for smoothing splines or lo for loess smooth terms. Additional smoothers can be added by creating the appropriate interface. Interactions with nonparametric smooth terms are not fully supported, but will not produce errors; they will simply produce the usual parametric interaction.

OPTIONAL ARGUMENTS:

family: a family object - a list of functions and expressions for defining the link

and variance functions, initialization, and iterative weights. Families upported are gaussian, binomial, poisson, Gamma, inverse.gaussian and quasi. Functions such as binomial produce a family object, but can be given without the parentheses. Family functions can take arguments, as in binomial(link=probit).

data: a data frame containing the variables occurring in the formula. If this is missing, the variables should be on the search list.

weights: vector of the observation weights for the fitting criterion. The length must be the same as the number of observations in the data. By default, an unweighted fit is produced.

subset: expression saying which subset of the rows of the data should be used in the fit. This can be a logical vector (which is replicated to have length equal to the number of observations), or a numeric vector indicating which observation numbers are to be included, or a character vector of the row names to be included. All observations are in cluded by default.

na.action: a function to filter missing data. This is applied to the model.frame after any subset argument has been used. The default (with na.fail) is to create an error if any missing values are found. A possible alternative is na.omit, which deletes observations that contain one or more missing values.

start: vector of initial values on the scale of the additive predictor.

control: a list of iteration and algorithmic constants. See gam.control for their names and default values. These can also be set as arguments to gam itself.

trace: logical flag: if TRUE, then the status during each iteration of the fitting is reported.

x: logical flag: if TRUE, then the x matrix is returned as component x.

y: logical flag: if TRUE, then the response is returned as component y.

contrasts: list of contrasts to be used for some or all of the factors appearing as variables in the model formula. The names of the list should be the names of the corresponding variables, and the elements should either be contrast-type matrices (matrices with as many rows as levels of the factor and with columns linearly independent of each other and of a column of one's), or else they should be functions that compute such contrast matrices.

...: all the optional arguments to lm can be given including weights, subset and na.action.

VALUE:

an object of class gam is returned, which inherits from both glm and lm. See gam.object for details.

DETAILS:

Components can be extracted using extractor functions predict, fitted, residuals, deviance, formula, and family. The output can be modified using update. It has all the components of a glm object, with a few more. The response variable must conform with the definition of family, for example factor or binary data if family=binomial is declared. The model is fit using the local scoring algorithm,

which iteratively fits weighted additive models by backfitting. The backfitting algorithm is a Gauss-Seidel method for fitting additive models, by iteratively smoothing partial residuals. The algorithm separates the parametric from the nonparametric part of the fit, and fits the parametric part using weighted linear least squares within the backfitting algorithm. Although nonparametric smooth terms lo and s can be mixed in a formula, it is more efficient computationally to use a single smoothing method for all the smooth terms in an additive model. In this case the entire local scoring algorithm is performed in Fortran.

REFERENCES:

Hastie, T. and Tibshirani, R. (1990). Generalized Additive Models. Chapman and Hall, London.

EXAMPLES:

```
gam(Kyphosis~s(Age,4)+Number,family=binomial)
gam(ozone^(1/3)~lo(radiation)+lo(wind,temperature),data =air)
gam(Kyphosis~poly(Age,2)+s(Start),data=kyphosis,subset=      Number>10)
```

B. glm function: Fit a Generalized Linear Model

DESCRIPTION: Produces an object of class "glm" which is a generalized linear fit of the data.

USAGE:

glm(formula,family=gaussian,data=<<see below>>,weights=<<see below>>,subset=<<see below>>,na.action=na.fail,start=<<see below>>,control,trace=F,model=F,x=F,y=T,contrasts=NULL,qr=F, ...)

REQUIRED ARGUMENTS:

formula: a formula expression as for other regression models, of the form response ~ predictors. See the documentation of lm and formula for details.

OPTIONAL ARGUMENTS:

family: a family object - a list of functions and expressions for defining the link and variance functions, initialization and iterative weights. Families supported are gaussian, binomial, poisson, Gamma, inverse. gaussian and quasi. Functions like binomial produce a family object, but can be given without the parentheses. Family functions can take arguments, as in binomial(link=probit).

data: an optional data frame in which to interpret the variables occurring in the formula.

weights: the optional weights for the fitting criterion.

subset: expression saying which subset of the rows of the data should be used in the fit. This can be a logical vector (which is replicated to have length equal to the number of observations), or a numeric vector indicating which obser vation numbers are to be included, or a character vector of the row names to be included. All observations are in cluded by default.

na.action: a function to filter missing data. This is applied to the model.frame

after any subset argument has been used. The default (with na.fail) is to create an error if any missing values are found. A possible alternative is na.omit, which deletes observations that contain one or more missing values.

start: a vector of initial values on the scale of the linear predictor.

control: a list of iteration and algorithmic constants. See glm.control for their names and default values. These can also be set as arguments to glm itself.

trace: logical flag: if TRUE, details of the iterations are printed. This can also be set in the control argument.

model: if TRUE, the model.frame is returned. If this argument is itself a model.frame, then the formula and data arguments are ignored, and model is used to define the model.

x: logical flag: if TRUE, the model.matrix is returned.

y: logical flag: if TRUE, the response variable is returned (default is TRUE).

contrasts: a list of contrasts to be used for some or all of the factors appearing as variables in the model formula. The names of the list should be the names of the corresponding variables, and the elements should either be contrast-type matrices (matrices with as many rows as levels of the factor and with columns linearly independent of each other and of a column of one's), or else they should be functions that compute such contrast matrices.

qr: logical flag: if TRUE, the QR decomposition of the model.matrix is returned.

...: control arguments may be given directly, see the control argument.

VALUE:

an object of class glm is returned, which inherits from lm. See glm.object for details.

DETAILS:

The output can be examined by print, summary, plot, and anova. Components can be extracted using predict, fitted, residuals, deviance, formula, and family. It can be modified using update. It has all the components of an lm object, with a few more. Other generic functions that have methods for glm objects are drop1, add1, step and preplot. Use glm.object for further details.

The response variable must conform with the definition of family, for example factor or binary data if family=binomial is declared.

The model is fit using Iterative Reweighted Least Squares (IRLS). The working response and iterative weights are computed using the functions contained in the family object. GLM models can also be fit using the function gam. The workhorse of glm is the function glm.fit which expects an x and y argument rather than a formula.

REFERENCES:

McCullagh, P. and Nelder, J. A. (1983). Generalized Linear Models. Chapman and Hall, London.

EXAMPLES:

glm(Count~.,data=solder,family=poisson)

glm(Kyphosis~poly(Age,2)+(Number>10)*Start, family=binomials

glm(ozone^(1/3)~bs(radiation,5)+poly(wind,temperature, degree=2),data=air)

C. poly function: Generate a Basis for Polynomial Regression.

USAGE:

poly(x, 3)

poly(x, y, 2)

poly(...)

ARGUMENTS:

...: the arguments to poly can be a comma-separated list of numeric vectors or matrices. If the final argument is atomic, positive, and integer-valued, it is taken to bethe degree of the polynomial.

VALUE:

a matrix of orthonormal polynomials is returned. For a single vector argument and a trailing degree argument (first case above), a matrix of orthonormal polynomials of given degree is returned (the constant column is excluded). The orthogonality is with respect to the data. For several arguments (vector, matrix, or both), each of the column vectors is used to generate

orthogonal polynomials of the required degree. The columns will be a subset of the tensor product of the the orthogonal polynomials of given degree of each of the individual variables. The ma trix has an attribute degree that is a vector giving the degree of each column.

When called with a single vector argument, poly returns an additional attribute coefs. This contains the normalization constants used in constructing the orthogonal polynomials. See the documentation for poly.raw for information on how these can be used to construct additional evaluations of the same polynomial basis.

EXAMPLES:

glm(Kyphosis~poly(Age,3)+Start,family=binomial)

D. s function: Specify a Smoothing Spline Fit in a GAM Formula

USAGE:

s(x, df=4, spar=0)

ARGUMENTS:

x: the univariate predictor, or expression, that evaluates to a numeric vector.

df: the target equivalent degrees of freedom, used as a smoothing parameter. The real smoothing parameter (spar below) is found such that df=tr(S)-1, where S is the implicit smoother matrix. Values for df should be greater than 1, with 1 implying a linear fit.

spar: can be used as smoothing parameter, with values larger than 0.

VALUE:

the vector x is returned, endowed with a number of attributes. The vector itself is used in the construction of the model matrix, while the attributes are needed for the backfitting algorithms all.wam or s.wam (weighted additive model). Since smoothing splines reproduces linear fits, the linear part will be efficiently computed with the other parametric linear parts of the model.

DETAILS:

Note that s itself does no smoothing; it simply sets things up for gam.

EXAMPLES:

```
# fit Start using a smoothing spline with 4 df.
y ~ Age + s(Start, 4)
# fit log(Start) using a smoothing spline with 5 df.
y ~ Age + s(log(Start), df=5)
```

E. lo function: Specify a Loess Fit in a GAM Formula.

USAGE:

lo(..., span=0.5, degree=1)

ARGUMENTS:

...: the unspecified ... can be a comma-separated list of numeric vectors, numeric matrix, or expressions that evaluate to either of these. If it is a list of vectors, they must all have the same length.

span: the number of observations in a neighborhood. This is the smoothing parameter for a loess fit.

degree: the degree of local polynomial to be fit; can be 1 or 2.

VALUE:

a numeric matrix is returned. The simplest case is when there is a single argument to lo and degree=1; a one column matrix is returned, consisting of a normalized version of the vector. If degree=2 in this case, a two-column matrix is returned, consisting of a 2d-degree orthogonal-polynomial basis. Similarly, if there are two arguments, or the single argument is a two-column matrix, either a two-column matrix is returned if degree=1, or a five-column matrix consisting of powers and products up to degree 2. Any dimensional argument is allowed, but typically one or two vectors are used in practice. The matrix is endowed with a number of attributes; the matrix itself is used in the construction of the model matrix, while the attributes are needed for the backfitting algorithms all.wam or lo.wam (weighted additive model). Local-linear curve or surface fits reproduce linear responses, while local-quadratic fits reproduce quadratic curves or surfaces. These parts of the loess fit are computed exactly together with the other parametric linear parts of the model. Note that lo itself does no smoothing; it

simply sets things up for gam.

EXAMPLES:

y ~ Age + lo(Start, span=.5)

fit Start using a loess smooth with a span of 0.5.

y ~ lo(Age) + lo(Start, Number)

y ~ lo(Age, 0.5) # the argument name for span is not needed.

APPENDIX II

Car Test Data Frame

	Price	Country	Reliability	Mileage	Type	Weight
Eagle Summit 4	8895	USA	4	33	Small	2560
Ford Escort 4	7402	USA	2	33	Small	2345
Ford Festiva 4	6319	Korea	4	37	Small	1845
Honda Civic 4	6635	Japan/USA	5	32	Small	2260
Mazda Protege 4	6599	Japan	5	32	Small	2440
Mercury Tracer 4	8672	Mexico	4	26	Small	2285
Nissan Sentra 4	7399	Japan/USA	5	33	Small	2275
Pontiac LeMans 4	7254	Korea	1	28	Small	2350
Subaru Loyale 4	9599	Japan	5	25	Small	2295
Subaru Justy 3	5866	Japan	NA	34	Small	1900
Toyota Corolla 4	8748	Japan/USA	5	29	Small	2390
Toyota Tercel 4	6488	Japan	5	35	Small	2075
Volkswagen Jetta 4	9995	Germany	3	26	Small	2330
Chevrolet Camaro V8	11545	USA	1	20	Sporty	3320
Dodge Daytona	9745	USA	1	27	Sporty	2885
Ford Mustang V8	12164	USA	1	19	Sporty	3310
Ford Probe	11470	USA	3	30	Sporty	2695
Honda Civic CRX Si 4	9410	Japan	5	33	Sporty	2170
Honda Prelude Si 4WS 4	13945	Japan	5	27	Sporty	2710
Nissan 240SX 4	13249	Japan	3	24	Sporty	2775
Plymouth Laser	10855	USA	NA	26	Sporty	2840
Subaru XT 4	13071	Japan	NA	28	Sporty	2485
Audi 80 4	18900	Germany	NA	27	Compact	2670
Buick Skylark 4	10565	USA	2	23	Compact	2640
Chevrolet Beretta 4	10320	USA	1	26	Compact	2655
Chrysler Le Baron V6	10945	USA	4	25	Compact	3065
Ford Tempo 4	9483	USA	2	24	Compact	2750

Honda Accord	4	12145	Japan/USA	5	26	Compact
2920						
Mazda 626	4	12459	Japan/USA	4	24	Compact
2780						
Mitsubishi Galant	4	10989	Japan	5	25	Compact
2745						
Mitsubishi Sigma V6		17879	Japan	4	21	Compact
3110						
Nissan Stanza	4	11650	Japan	5	21	Compact
2920						
Oldsmobile Calais	4	9995	USA	2	23	Compact
2645						
Peugeot 405	4	15930	France	NA	24	Compact
2575						
Subaru Legacy	4	11499	Japan/USA	5	23	Compact
2935						
Toyota Camry	4	11588	Japan/USA	5	27	Compact
2920						
Volvo 240	4	18450	Sweden	3	23	Compact
2985						
Acura Legend V6		24760	Japan	5	20	Medium
3265						
Buick Century	4	13150	USA	3	21	Medium
2880						
Chrysler Le Baron Coupe		12495	USA	2	22	Medium
2975						
Chrysler New Yorker V6		16342	USA	3	22	Medium
3450						
Eagle Premier V6		15350	USA	2	22	Medium
3145						
Ford Taurus V6		13195	USA	3	22	Medium
3190						
Ford Thunderbird V6		14980	USA	1	23	Medium
3610						
Hyundai Sonata	4	9999	Korea	NA	23	Medium
2885						
Mazda 929 V6		23300	Japan	5	21	Medium
3480						
Nissan Maxima V6		17899	Japan	5	22	Medium
3200						

		Disp.	HP
Eagle Summit	4	97	113
Ford Escort	4	114	90
Ford Festiva	4	81	63
Honda Civic	4	91	92
Mazda Protege	4	113	103
Mercury Tracer	4	97	82
Nissan Sentra	4	97	90
Pontiac LeMans	4	98	74
Subaru Loyale	4	109	90
Subaru Justy	3	73	73
Toyota Corolla	4	97	102
Toyota Tercel	4	89	78
Volkswagen Jetta	4	109	100
Chevrolet Camaro	V8	305	170
Dodge Daytona		153	100
Ford Mustang	V8	302	225
Ford Probe		133	110
Honda Civic CRX Si	4	97	108
Honda Prelude Si 4WS	4	125	140
Nissan 240SX	4	146	140
Plymouth Laser		107	92
Subaru XT	4	109	97
Audi 80	4	121	108
Buick Skylark	4	151	110

```
                    Chevrolet Beretta 4   133  95
                   Chrysler Le Baron V6   181 141
                           Ford Tempo 4   141  98
                         Honda Accord 4   132 125
                            Mazda 626 4   133 110
                     Mitsubishi Galant 4   122 102
                     Mitsubishi Sigma V6   181 142
                         Nissan Stanza 4   146 138
                     Oldsmobile Calais 4   151 110
                           Peugeot 405 4   116 120
                        Subaru Legacy 4    135 130
                         Toyota Camry 4    122 115
                            Volvo 240 4    141 114
                        Acura Legend V6    163 160
                        Buick Century 4    151 110
                Chrysler Le Baron Coupe    153 150
                 Chrysler New Yorker V6    202 147
                       Eagle Premier V6    180 150
                         Ford Taurus V6    182 140
                    Ford Thunderbird V6    232 140
                       Hyundai Sonata 4    143 110
                           Mazda 929 V6    180 158
                       Nissan Maxima V6    180 160

                                    Price Country Reliability Mileage   Type
Weight
   Oldsmobile Cutlass Ciera 4 13150     USA           2       21 Medium
2765
Oldsmobile Cutlass Supreme V6 14495     USA          NA       21 Medium
3220
            Toyota Cressida 6 21498   Japan           3       23 Medium
3480
            Buick Le Sabre V6 16145     USA           3       23  Large
3325
         Chevrolet Caprice V8 14525     USA           1       18  Large
3855
   Ford LTD Crown Victoria V8 17257     USA           3       20  Large
3850
      Chevrolet Lumina APV V6 13995     USA          NA       18    Van
3195
       Dodge Grand Caravan V6 15395     USA           3       18    Van
3735
             Ford Aerostar V6 12267     USA           3       18    Van
3665
                 Mazda MPV V6 14944   Japan           5       19    Van
3735
          Mitsubishi Wagon 4 14929   Japan          NA       20    Van
3415
             Nissan Axxess 4 13949   Japan          NA       20    Van
3185
                 Nissan Van 4 14799   Japan          NA       19    Van
3690

                                  Disp.  HP
   Oldsmobile Cutlass Ciera 4   151 110
Oldsmobile Cutlass Supreme V6   189 135
            Toyota Cressida 6   180 190
            Buick Le Sabre V6   231 165
         Chevrolet Caprice V8   305 170
   Ford LTD Crown Victoria V8   302 150
      Chevrolet Lumina APV V6   151 110
       Dodge Grand Caravan V6   202 150
             Ford Aerostar V6   182 145
                 Mazda MPV V6   181 150
          Mitsubishi Wagon 4    143 107
             Nissan Axxess 4    146 138
                 Nissan Van 4   146 106
```

APPENDIX III

The General Linear Perturbation Theory

The general linear perturbation theory is described as follows:

(1) Express both input and output variables as a constant plus a small departure.

(2) Substitute these variables into equations that connect them.

(3) Ignore all expressions which are small compared to those small departures.

An example used in our study in section 9.5 is given here.

$$f=\frac{1}{T} \tag{A1}$$

Now let

$$T(t)=T_0+T_1(t), \qquad f(t)=f_0+f_1(t) \tag{A2}$$

Since that

$$\frac{1}{(T_0+T_1)}=\frac{1}{T_0}-\frac{T_1}{T_0^2}+\frac{T_1^2}{T_0^3}-\cdots \tag{A3}$$

Substitute (A3) and (A2) into (A1) and ignore smaller terms, we obtain

$$f_1=-\frac{T_1}{T_0^2} \tag{A4}$$

The (A4) is the result change of f due to change of T using the linear perturbation theory.

In section 9.5, we let $s = s_0 + s_1$ and $T = T_0 + T_1$, and substitute them into

the following integral equation

$$C=\int_{t_n}^{t_{n+1}} s_1(t')\,dt' \tag{A5}$$

Then

$$\begin{aligned} C&=\int_{t_n}^{t_{n+1}} (s_0+s_1(t'))\,dt' \\ &=s_0(t_{n+1}-t_n)+\int_{t_n}^{t_{n+1}} s_1(t')\,dt' \\ &=s_0T+\int_{t_{n+1}-T}^{t_{n+1}} s_1(t')\,dt' \\ &=s_0T_0+s_0T_1+\int_{t_{n+1}-T_0-T_1}^{t_{n+1}} s_1(t')\,dt' \end{aligned} \tag{A6}$$

Since $C = s_0/f_0 = s_0T_0$, and $T_1 \ll T_0$, the above equation can be further simplified into

$$\int_{t_{n+1}-T_0}^{t_{n+1}} s_1(t') \approx -s_0T_1 \tag{A7}$$

Substitution (A4) into (A7) yields

$$f_1 = -\frac{T_1}{T_0^2} = \frac{1}{T_0^2}\int_{t-T_0}^{t} \frac{s_1(t')}{s_0}\,dt' \qquad \text{(A8)}$$

APPENDIX IV

Figures for the Simulation

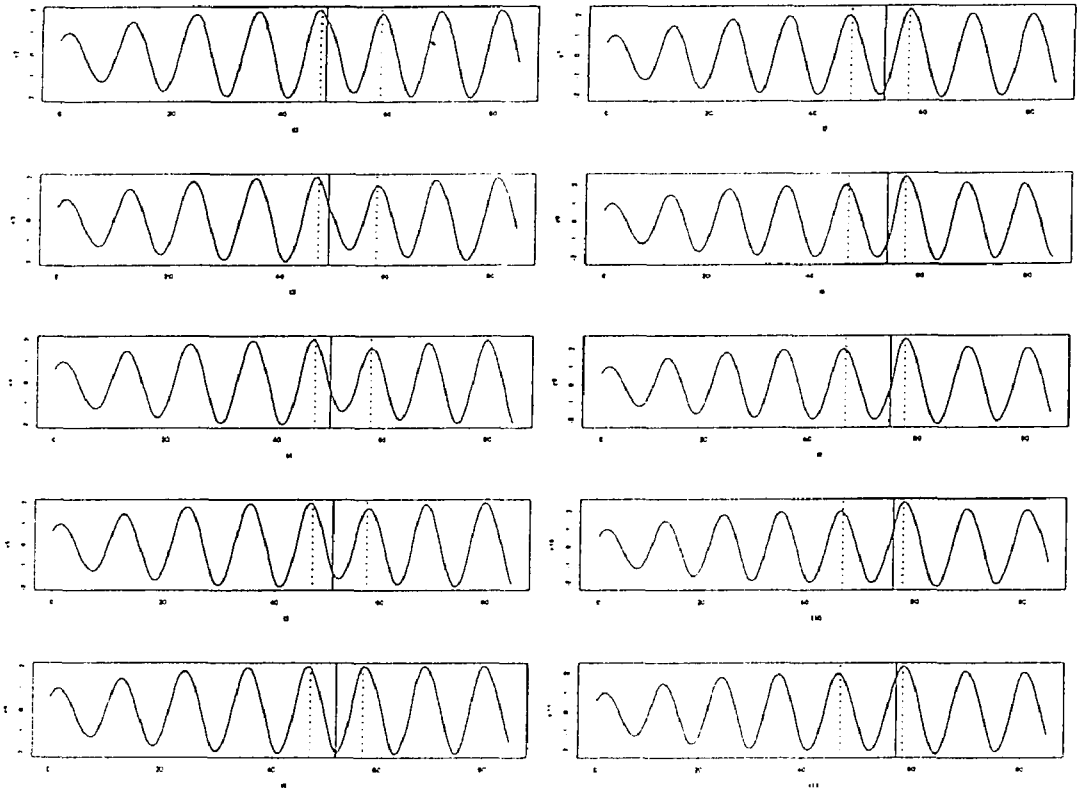

Figure 9.3.2.2 The perturbation process. The solid line represents the stimulus. The dotted lines represent the phase markers.

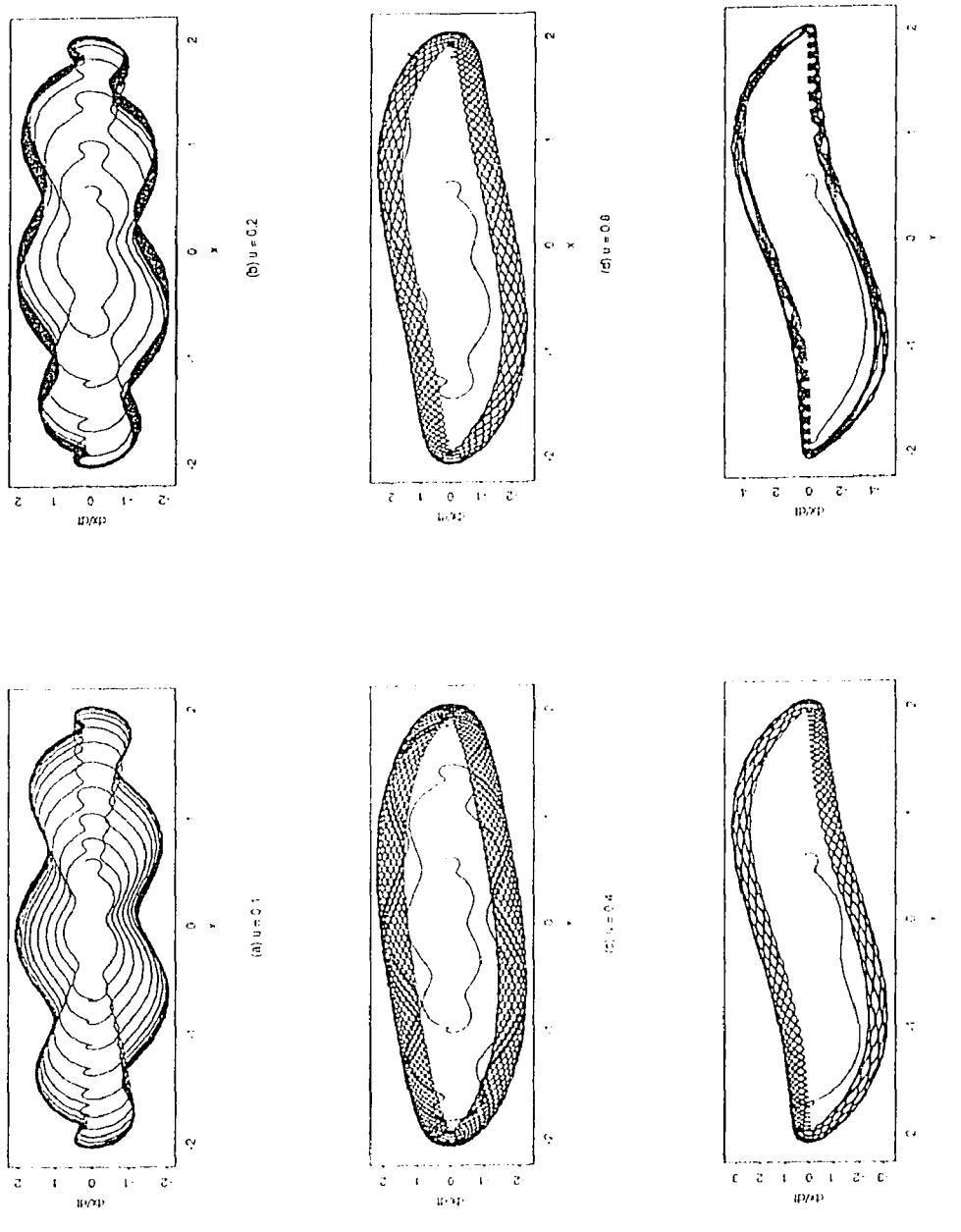

Figure 9.3.3.1 Phase planes during different nonlinearities.

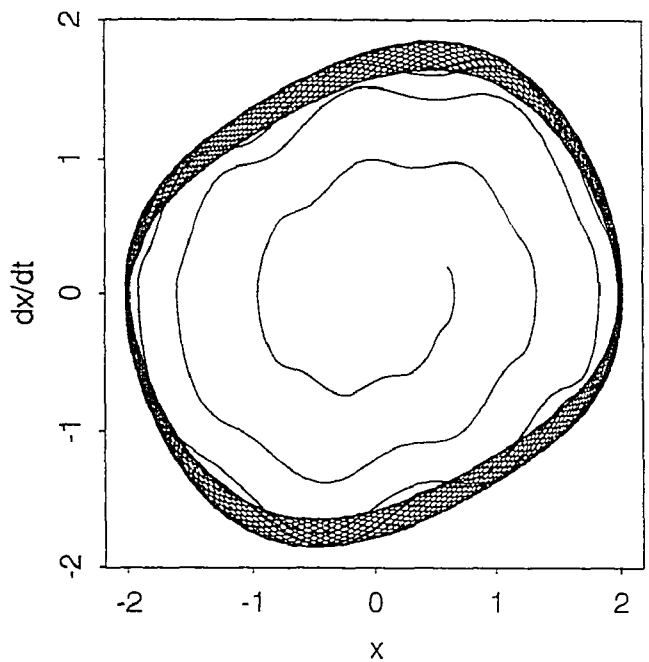

(a) Direct coupling.

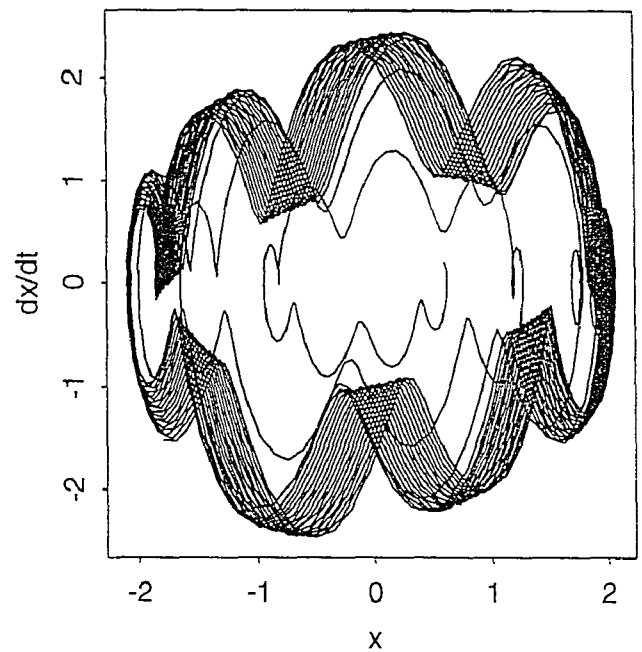

(b) Velocity coupling.

Figure 9.3.3.2 Phase planes related to the coupling ways.

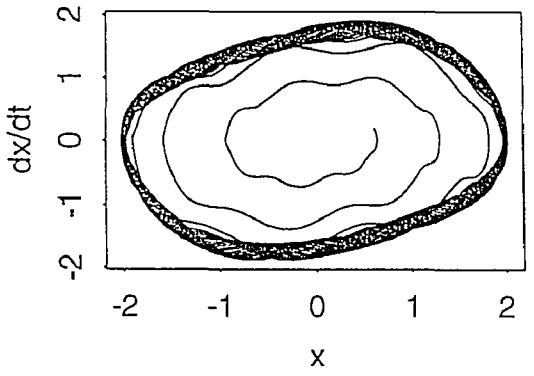

(a) Coupling coefficient = 0.1.

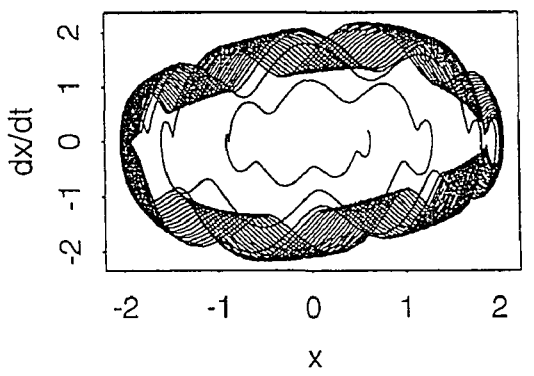

(b) Coupling coefficient = 0.3.

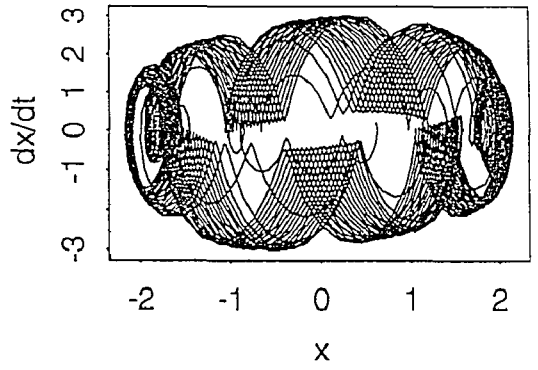

(c) Coupling coefficient = 0.9.

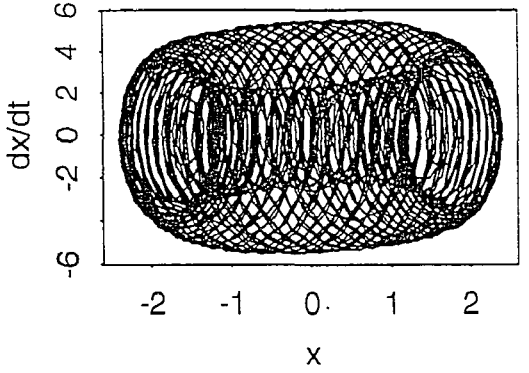

(d) Coupling coefficient = 2.7.

Figure 9.3.3.3 Phase planes related to different coupling coefficients.

APPENDIX V

Programs

Programs for the Van Der Pol oscillators

The following programs are used to simulate one Van der Pol oscillator, two coupled Van der Pol oscillators with either direct coupling or velocity coupling. The main program is written in Splus language (version 3.2), and the subroutines are written in FORTRAN 77.

main program

```
function(k = 3.819719, u = 0.2, wx = 1.92, wy = 0.923, tp = 0.2, tw = 0.1, f1
        = 0, f2 = 1.6, fs = 0.5, ftime = 700, km = 10000, dxsav = 0.1667)
{
        dyn.load("/usr3/pei/model/vdpol2plus.o")
        btime <- 0
        kmax <- round(ftime/dxsav)
        if(kmax > km) {
                kmax <- km
        }
        nvar <- 5
        yy <- c(0.6, 0.2, 0.6, 0.2)
        kx <- k
        ky <- k
        ux <- u
        uy <- u
        f1 <-  - f1
        f2 <-  - f2
        cof <- c(kx, ky, ux, uy, wx, wy, tp, f1, f2, fs, tw)
        yp <- matrix(0, kmax, nvar)
        z <- .Fortran("odeint",
                as.single(cof),
                as.single(yy),
                as.integer(nvar),
                as.single(btime),
                as.single(ftime),
                as.integer(kmax),
                as.single(dxsav),
                x = as.single(yp))
        re <- matrix(z$x, ncol = nvar, byrow = T)
        l <- length(seq(1:length(re[, 1]))[re[, 1] > 0])
        ay <- re[1:l,  ]
        result <- list(t = ay[, 1], x = ay[, 2], xdot = ay[, 3], y = ay[, 4],
```

```
            ydot = ay[, 5])
}
```

Subroutines

```
C       PROGRAM INTEG1
C       PARAMETER (KM=10000,NVAR=5)
C       DIMENSION YY(NVAR),YP(NVAR,KM)
C       DIMENSION COF(11)
C       OPEN(6,FILE='INT.DAT')
C       COF(1)=24/(2*3.1416)
C       COF(2)=24/(2*3.1416)
C       COF(3)=0.2
C       COF(4)=0.2
C       COF(5)=1.92
C       COF(6)=0.923
C       COF(7)=0.3
C       COF(8)=-0.4
C       COF(9)=-0.4
C       COF(10)=1.0
C       COF(11)=0.1
C       YY(1)=0.6
C       YY(2)=0.2
C       YY(3)=0.6
C       YY(4)=0.2
C       BTIME=0.0
C       FTIME=250.0
C       DXSAV=0.1667
C       KMAX=INT((FTIME-BTIME)/DXSAV)
C       IF(KMAX.GE.KM) KMAX=KM
C       CALL ODEINT(COF,YY,NVAR,BTIME,FTIME,KMAX,DXSAV,YP)
CC        DO 27 I=1,KMAX
CC        IF(YP(1,I).EQ.0.0) GOTO 27
CC        WRITE(6,*) YP(1,I),YP(2,I),YP(3,I),YP(4,I),YP(5,I)
CC27      CONTINUE
C       CLOSE(6)
C       END

      SUBROUTINE DERIVS(COF,X,Y,DYDX)
C**********************************************
C      Please specify your ordinaty equations
C                here
C**********************************************

C
```

```
C     Kx -- A1, Ky -- A2.
C     Ux -- UX, Uy -- UY.
C     K -- RK
C     Wx -- WX, Wy -- WY.
C     B1 -- direct coupling
C     B2 -- velocity coupling
C     x -- Y(1), dx/dt -- DYDX(1)=Y(2)
C     y -- Y(3), dy/dt -- DYDX(3)=Y(4)
C
      DIMENSION COF(11),Y(10),DYDX(10)
      Z=0.0
      ZT=0.0
      A1=COF(1)
      A2=COF(2)
      UX=COF(3)
      UY=COF(4)
      WX=COF(5)
      WY=COF(6)
      T=COF(7)
      B1=COF(8)
      B2=COF(9)
      B3=COF(10)
      W=COF(11)
      Z=X-FLOAT(INT(X/T))*T
      IF(Z.LT.W) ZT=1.0
      IF(Z.GE.W) ZT=0.0
      DYDX(1)=Y(2)
      DYDX(2)=UX*A1*(1-Y(1)*Y(1))*Y(2)-WX*WX*Y(1)-B1*Y(3)-B2*Y(4)
      DYDX(2)=DYDX(2)/(A1*A1)
      DYDX(3)=Y(4)
      DYDX(4)=UY*A2*(1-Y(3)*Y(3))*Y(4)-WY*WY*Y(3)-B1*Y(1)-B2*Y(2)
      DYDX(4)=(DYDX(4)+B3*ZT)/(A2*A2)
      RETURN
      END
C
C
      SUBROUTINE RK4(COF,Y,DYDX,N,X,H,YOUT,DERIVS)
C     C  Given values for Nvariables Y and their derivatives DYDX known
C     C  at X,use the fourth-order Runge-Kutta method to advance the
C     C  solution an interval H and return the increnmented variables
C     C  YOUT,which need not to be a distinct array from Y. The User
C     C  supplies the subroutine DERIVS(X,Y,DYDX) which returns derivates
C     C  DYDX at X.
      PARAMETER (NMAX=10)
      DIMENSION
Y(N),DYDX(N),YOUT(N),YT(NMAX),DYT(NMAX),DYM(NMAX)
```

```
      DIMENSION COF(11)
      HH=0.5*H
      H6=H/6
      XH=X+HH
      DO 11 I=1,N
         YT(I)=Y(I)+HH*DYDX(I)
11    CONTINUE
      CALL DERIVS(COF,XH,YT,DYT)
      DO 12 I=1,N
         YT(I)=Y(I)+HH*DYT(I)
12    CONTINUE
      CALL DERIVS(COF,XH,YT,DYM)
      DO 13 I=1,N
         YT(I)=Y(I)+H*DYM(I)
         DYM(I)=DYT(I)+DYM(I)
13    CONTINUE
      CALL DERIVS(COF,X+H,YT,DYT)
      DO 14 I=1,N
         YOUT(I)=Y(I)+H6*(DYDX(I)+DYT(I)+2*DYM(I))
14    CONTINUE
      RETURN
      END


      SUBROUTINE
RKQC(COF,Y,DYDX,N,X,HTRY,EPS,YSCAL,HDID,HNEXT,DERIVS)
C     C     Fifth-order Runge-Kutta step with monitoring of local
C     C     trunction error to ensure accurary and adjust step-size
C     C     Input are dependent variable vector Y of lenth N and its
C     C     derivative DYDX at the starting value of the independent
C     C     variable X. Also input are the stepsize to be attempted
C     C     HTRY,the required accuracy EPS,and the vector YSCAL against
C     C     which error is scaled. On output,Y and X are replaced by new
C     C     values,HDID is the stepsize which was really accomplished
C     C     and HNEXT is the estimated next stepsize.DERIVS is the
C     C     user-supplied subroutine that computes the right-hand
C     C     side derivatives.
      PARAMETER
(NMAX=10,PGROW=-0.2,PSHRNK=-0.25,FCOR=1./15.,ONE=1.0)
      PARAMETER (SAFETY=0.9,ERRCON=1.E-7)
      EXTERNAL DERIVS
      DIMENSION Y(N),DYDX(N),YSCAL(N),YTEMP(NMAX)
      DIMENSION YSAV(NMAX),DYSAV(NMAX)
      DIMENSION COF(11)
      XSAV=X
      DO 15 I=1,N
```

```
          YSAV(I)=Y(I)
          DYSAV(I)=DYDX(I)
15     CONTINUE
       H=HTRY
16     HH=0.5*H
       CALL RK4(COF,YSAV,DYSAV,N,XSAV,HH,YTEMP,DERIVS)
       X=XSAV+HH
       CALL DERIVS(COF,X,YTEMP,DYDX)
       CALL RK4(COF,YTEMP,DYDX,N,X,HH,Y)
       X=XSAV+H
C      IF(X.EQ.XSAV) PAUSE 'Stepsize is not significant in RKQC'
       IF(X.EQ.XSAV) RETURN
       CALL RK4(COF,YSAV,DYSAV,N,XSAV,H,YTEMP)
       ERRMAX=0
       DO 17 I=1,N
          YTEMP(I)=Y(I)-YTEMP(I)
          ERRMAX=MAX(ERRMAX,ABS(YTEMP(I)/YSCAL(I)))
17     CONTINUE
       ERRMAX=ERRMAX/EPS
       IF(ERRMAX.GT.ONE) THEN
         H=SAFETY*H*(ERRMAX**PSHRNK)
         GOTO 16
       ELSE
         HDID=H
         IF(ERRMAX.GT.ERRCON) THEN
           HNEXT=SAFETY*H*(ERRMAX**PGROW)
         ELSE
           HNEXT=4.*H
         ENDIF
       ENDIF
       DO 18 I=1,N
         Y(I)=Y(I)+YTEMP(I)*FCOR
18     CONTINUE
       RETURN
       END
       SUBROUTINE
ODEINT(COF,YSTART,NVAR,BTIME,FTIME,KMAX,DXSAV,YP)
       PARAMETER (MAXSTP=20000,TWO=2.0,ZERO=0.0,TINY=1.E-30)
       PARAMETER (NMAX=10,EPS=1.E-5,HMIN=1.E-32)
       DIMENSION YP(NVAR,KMAX)
       DIMENSION YSTART(NVAR),YSCAL(NMAX),Y(NMAX),DYDX(NMAX)
       DIMENSION YSAV(NMAX),DYSAV(NMAX)
       DIMENSION COF(11)
       NOK=0
       NBAD=0
       X1=BTIME
```

```
      X2=FTIME
      H1=DXSAV/9.0
      X=X1
      H=H1
      KOUNT=0
      NVAR1=NVAR-1
      DO 19 I=1,NVAR1
         Y(I)=YSTART(I)
19    CONTINUE
      CALL DERIVS(COF,X,Y,DYDX)
      DO 30 I=1,NVAR1
        YSAV(I)=Y(I)
        DYSAV(I)=DYDX(I)
30    CONTINUE
      XXSAV=X
      IF(KMAX.GT.0) XSAV=X-DXSAV
      DO 20 NSTP=1,MAXSTP
      IF(KMAX.GT.0) THEN
         IF(ABS(X-XSAV).GT.ABS(DXSAV)) THEN
          H=DXSAV+XSAV-XXSAV
          X=XXSAV+H
          CALL RK4(COF,YSAV,DYSAV,N,XXSAV,H,Y,DERIVS)
            IF(KOUNT.LT.KMAX-1) THEN
               KOUNT=KOUNT+1
               YP(1,KOUNT)=X
      DO 22 I=2,NVAR
                  I1=I-1
                  YP(I,KOUNT)=Y(I1)
22    CONTINUE
           XSAV=X
          ENDIF
         ENDIF
      ENDIF
         CALL DERIVS(COF,X,Y,DYDX)
      DO 21 I=1,NVAR1
           YSCAL(I)=ABS(Y(I))+ABS(H*DYDX(I))+TINY
21    CONTINUE
      DO 35 I=1,NVAR1
        YSAV(I)=Y(I)
        DYSAV(I)=DYDX(I)
35    CONTINUE
      XXSAV=X
      IF((X+H-X2)*(X+H-X1).GT.ZERO) H=X2-X
      CALL RKQC(COF,Y,DYDX,NVAR1,X,H,EPS,YSCAL,HDID,HNEXT,DERIVS)
      IF(HDID.EQ.H) THEN
        NOK=NOK+1
```

```
      ELSE
        NBAD=NBAD+1
      ENDIF
      IF((X-X2)*(X2-X1).GE.ZERO) THEN
      DO 23 I=1,NVAR1
            YSTART(I)=Y(I)
23     CONTINUE
         IF(KMAX.NE.0) THEN
           KOUNT=KOUNT+1
           YP(1,KOUNT)=X
           DO 24 I=2,NVAR
           I1=I-1
              YP(I,KOUNT)=Y(I1)
24          CONTINUE
         ENDIF
         RETURN
      ENDIF
C       IF(ABS(HNEXT).LT.HMIN) PAUSE 'Stepsize smaller than minimum'
      IF(ABS(HNEXT).LT.HMIN) RETURN
      H=HNEXT
      z=x-float(int(x/0.3))*0.3
      if(z.lt.0.1) zz=1.0
      if(z.ge.0.1) zz=0.0
      write(6,*) x,zz
20     CONTINUE
      RETURN
      END
```

REFERENCES

[1] S.Shin, W. Tapp, S. Reisman and B. Natelson, "Assessment of autonomic regulation of heart rate variability by the method of complex demodulation," *IEEE Trans. on Biomed. Eng.*, Vol. 36, No. 2, pp274-283, Feb. 1989.

[2] G. Berntson, J. Cacioppo and K. Quigley, "Respiratory sinus arrhythmia: Autonomic origins, physiological mechanisms, and psychophysiological implications," *Psychophysiology*, 30, pp183-196, 1993.

[3] Y. Nakamura, Y. Yamamoto and I. Muraoka, "Autonomic control of heart rate during physical exercise and fractal dimension of heart rate variability," *J. Appl. Physiol.* 74(2): 875-881, 1993.

[4] J. Jalife and C. Antzelevitch, "Phase resetting and annihilation of pacemaker activity in cardiac tissue," *Science*, Vol. 206, November, 1979.

[5] G. Brown and J. Eccles, "The action of a single vagal volley on the rhythm of the heart beat," *J. Physiol.*, London 82: 211-240, 1934.

[6] A. Winfree, *When time breaks down: 3 dimensional dynamics of electrochemical waves and cardiac arrhythmias*. Princeton Univ. Press, 1987.

[7] M. Guevara, A. Sherier and L. Glass, "Phase resetting of spontaneously beating embryonic ventricular heart cell aggregates," *Am. J. Physiol.*, 251, H1298-H1305, 1986.

[8] L. Glass, R. Guevara, A Sherier and R. Perez, "Bifurcation and chaos in a periodically stimulated cardiac oscillator," *Physica 7D*, pp89-101, 1983.

[9] A. Vander, J. Sherman and D. Luciano, *Human physiology: The mechanism of body function*, McGraw Hill Book company, 4th ed., pp301-421, 1985.

[10] J. Jalife, V. Slenter, J. Salata and D. Michaels, "Dynamic vagal control of pacemaker activity in the mammalian sinoatrial node," *Cir. Res.* 52, pp642-656, 1983.

[11] M. Levy and P. Martin, "Neural control of heart rate and atrioventricular conduction," *Am. Physiol. Society*, pp205-215, 1981.

[12] P. Zhang, S. Reisman and W. Tapp, "Heart rate variability study using phase response curve," *IEEE Biomed. Eng. Conf.*, Paris, pp571-572, 1992.

[13] V. Reiner and C. Antzelevitch, "Phase resetting and annihilation in a mathematical model of sinus node," *Am. J. Physiol.* 249: H1143-H1153, 1985.

[14] J. Jalife and C. Antzelevitch, "Pacemaker annihilation: diagnostic and therapeutic implications," *Am. Heart Journal*, Vol. 100, No. 1, pp128-129, July, 1980.

[15] A. Selman, A. McDonald, R. Kitney and D. Linkens, "The interaction between heart rate and respiration: Part I - Experimental studies in man," *Automedica*, Vol.4, pp131-139, 1982.

[16] R. Kitney, T. Fulton, A. McDonald and D. Linkens, "Transient interactions between blood pressure, respiration and heart rate in man," *J. Biomed. Eng.* Vol. 7, pp217-224, July, 1985.

[17] S. Akselrod, D. Gordon, J. Madwed, N. Snidman, D. Shannon and R. Cohen, "Hemodynamic regulation: investigation by spectral analysis," *Am. J. Physiol.* 249, H867-H875, 1985.

[18] M. Pagani, F. Lombardi, S. Guzzetti, O. Rimoldi and et al., "Power spectral analysis of heart rate and arterial pressure variabilities as a marker of sympatho-vagal interaction in man and conscious dog," *Cir. Research* 59:178-193, 1986.

[19] F. Wiese, F. Heydenreich, W. Gehrig and U. Runge, "Heart rate variability in diabetic patients during orthostatic load: a spectral analytic approach," *Klin Wochenschr* 68:26-32, 1990.

[20] V. Schechtman, K. Kluge and R. Harper, "Time-domain system for assessing variation in heart rate," *Med. & Biol. Eng. & Comput.* 26, pp367-373, 1988.

[21] Y. Yamamoto and R. Hughson, "Coarse-graining spectral analysis: new method for studying heart rate variability," *J. Appl. Physiol.* 71(3): 1143-1150, 1991.

[22] S. Zhang, S. Reisman, W. Tapp and P. Zhang, "Correlation dimension in heart rate variability," *19th IEEE Annual Northeast Bioeng. conf.*, pp11-12, 1993.

[23] P. Zhang, S. Reisman, W. Tapp and D. Cordero, "Information entropy and dimension calculation on heart rate variability," *19th IEEE Annual Northeast Bioeng. conf.*, pp9-10, 1993.

[24] D. Cordero, W. Tapp, P. Zhang and S. Reisman "Phase Response Curve Analysis of Heart Rate Variability with Differing Breathing Rates," *19th IEEE Annual Northeast Bioeng. conf.*, pp124-125, 1993.

[25] A. Goldberger, D. Goldwater and V. Bhargava, "Atropine unmasks bed-rest effect: Spectral analysis of cardiac interbeat intervals," *J. Appl. Physiol.* 61(5): 1843-1848, 1980.

[26] D. Cordero, W. Tapp, P. Zhang, S. Reisman and S. Cook, "Phase-response curve analysis of heart rate variability in unanesthetized humans," *The Society for Neuroscience Abstracts*, Vol. 19, 1993, in press.

[27] W. Boda, S. Sisto, P. Zhang, T. Findley, W. Tapp and B. Natelson, "Comparison of vagal power during paced breathing and treadmill exercise testing in chronic fatigue syndrome," *The Society of Neuroscience Abstracts*, Vol. 18, 495.12, 1992.

[28] L. Glass, P. Hunter and A. McCulloch, *Theory of heart: biomechanics, biophysics, and nonlinear dynamics of cardiac function.* New York: Springer-Verlag, 1991, pp294-299.

[29] W. Tapp, F. Knox and B. Natelson, "The heart rate spectrum in simulated flight: Reproductivity and effects of atropine", *Aviat.Space Environ.Med.*, 61:887-892, 1990.

[30] P. Bloomfield, *Fourier Analysis of Time Series: An Introduction.* New York: Wiley, 1976.

[31] K. Lafferty, J. Trafford, V. Roberts and L. Cotton, "Raynaud's phenomenon and thermal entrainment: an objective test," *British Medical Journal*, Vol. 286, pp90-92, Jan., 1983.

[32] Ronald N. Bracewell, "The Fourier transform," *Scientific American*, pp86-95, June, 1989.

[33] S. Akselrod, D. Gordon, F. Ubel, D. Shannon, A. Barger and R. Cohen, "Power spectrum analysis of heart rate fluctuation: A quantitative probe of beat-to-beat cardiovascular control," *Science*, Vol. 213, pp220-222, July, 1981.

[34] A. Papoulis, *Probability, Random Variables, and Stochastic Process.* McGraw-Hill, 1984.

[35] S. Guiasu, *Information Theory with Applications.* New York: McGraw-Hill, 1977.

[36] T. Parker and L. Chua, " Chaos: A tutorial for engineers", *Proceedings of*

the IEEE, Vol 75, No. 8, pp982-1008, Aug. 1987.

[37] D. Kaplan, M. Furman, S. Pincus, S. Ryan and L. Lipsitz, "Aging and the complexity of cardiovascular dynamics," *Biophys. J.*, Vol. 59, pp945-949, Apr. 1991.

[38] R. Watt, K. Ethlers, P. Scipione, E. Maslana and S. Hameroff, " Dimensional analysis of electroencephalogram during general anesthesia," *IEEE Eng. in Medicine & Biology 11 th Annual International Conf.*, pp1881-1882, 1989.

[39] J. Skinner, C. Pratt and T. Vybiral, " A reduction in the correlation dimension of heartbeat intervals precedes imminent ventricular fibrillation in human subjects," *American Heart Journal*, Vol. 125, No. 3, pp731-743, 1993.

[40] B. Knight, "Dynamics of Encoding in a Population of Neurons," *J. Gen. Physiol.* 59, pp734-766, 1972.

[41] C. Peskin, *Mathematical Aspects of Heart Physiology*. New York Univ., pp268-278, 1974.

[42] R. Barr, "The electrocardiogram and its relationship to excitation of the heart," in *Physiology and Pathophysiology of The Hea*rt, Kluwer Academic Publishers, 2nd edition, pp175-193, 1989.

[43] M. Levy and P. Martin, "Autonomic neural control of cardiac function," in *Physiology and Pathophysiology of The Heart*, Kluwer Academic Publishers, 2nd edition, pp361-379, 1989.

[44] S. Haykin, *Communication Systems*. 2nd edition, John Wiley & Sons Inc., 1983.

[45] A. Oppenheim and R. Schafer, *Digital Signal Processing*. New Jersey: Prentice-Hall, Inc., 1975.

[46] N. Minorsky, *Nonlinear Oscillations*. New Jersey: D. Van Nostrand Company, Inc., 1962.

[47] J. Hsu and A. Meyer, *Modern Control Principles and Applications*. New York: McGraw Hill Book Company, 1976.

[48] J. Chambers and T. Hastie, *Statistical models in S*. California: Wadsworth

& Brooks/Cole Advanced Brooks & Software Pacific Grove, 1990.

[49] B. Friedland, *Control System Design: An introduction to state space methods*. McGraw-Hill Book Company, 1986.